DOKUZ EYLÜL UNIVERSITY

GRADUATE SCHOOL OF NATURAL AND APPLIED SCIENCES

DESIGN, DEVELOPMENT AND PRODUCTION OF A DIGITAL RADIOGRAPHY SYSTEM

by

İdil ARİTMAN

January, 2019

İZMİR

DESIGN, DEVELOPMENT AND PRODUCTION OF A DIGITAL RADIOGRAPHY SYSTEM

A Thesis Submitted to the
Graduate School of Natural and Applied Sciences of Dokuz Eylül University
In Partial Fulfillment of the Requirements for the Degree of Doctor of Philosophy in Nanoscience and Nanoengineering Program

by

İdil ARİTMAN

January, 2019
İZMİR

Ph.D. THESIS EXAMINATION RESULT FORM

We have read the thesis entitled "**DESIGN, DEVELOPMENT AND PRODUCTION OF A DIGITAL RADIOGRAPHY SYSTEM**" completed by **İDİL ARİTMAN** under the supervision of **PROF.DR. KADRİYE ERTEKİN** and we certify that in our opinion it is fully adequate, in scope and in quality, as a thesis for the degree of Doctor of Philosophy.

Prof. Dr. Kadriye ERTEKİN
Supervisor

Prof. Dr. Birol ENGİN
Thesis Committee Member

Assoc. Prof. Dr. M. Faruk EBEOĞLUGİL
Thesis Committee Member

Assoc. Prof. Dr. Mücahit SÜTÇÜ
Examining Committee Member

Assoc. Prof. Dr. Osman ÇULHA
Examining Committee Member

Prof. Dr. Kadriye ERTEKİN
Director
Graduate School of Natural and Applied Sciences

ACKNOWLEDGMENTS

I would like to express my sincere indebtedness and gratitude to my thesis advisor Prof. Dr. Kadriye ERTEKİN for all his time and effort. Her guidance and input at every stage of my work truly helped me navigate this endeavor. I would like to thank dear co-advisor Prof. Dr. Erdal ÇELİK for his supports during my academic studies. He has always been by my side in my Ph.D. I would also like to thank Assoc. Prof. Dr. Mehmet Faruk EBEOĞLUGİL and Prof. Dr. Birol ENGİN for the useful discussions on periodical meetings of this research.

I would like to thank my friends, Serdar YILDIRIM, Metin YURDDAŞKAL, Sevcan KARDELEN, and Hilmiye Deniz ERTUĞRUL UYGUN for their encouragement and helps. I would also like to thank the administration of the Center for Fabrication and Applications of Electronic Materials (EMUM) for financial and laboratory support. Honorable Prof. Dr. Rasim İPEK, thank you for the value and effort that you gave me.

Most importantly, I am thankful to Leyla KIRKPINAR, my dear mother, the founder of all my successes and happy days in my life. I express my gratitude and love to my father, Kenan KIRKPINAR, who made all sorts of sacrifices for me for years. My sweet sister, Umay KIRKPINAR, you are my greatest chance and my beloved husband who shares the burden of life with me and always gives me love and support, my life partner. I thank Mehmet ARITMAN for being in my life. I am kissing my dear son Yetkin ARITMAN, the most precious person in my life. Their love and support always gave me strength.

İdil ARİTMAN

DESIGN, DEVELOPMENT AND PRODUCTION OF A DIGITAL RADIOGRAPHY SYSTEM

ABSTRACT

The development of scintillation materials are important because of the ever-increasing need for materials in high-energy physics and digital radiography. The present composition of the scintillators consists of organic or inorganic materials, each of which is suitable for different applications. Inorganic crystal scintillators are widely used because of their superior energy solubility and stiffness for high energy radiation. In the scope of the thesis, inorganic $Gd_2O_2SO_4$ phosphorescent nanoparticles which are doped with pure and rare earth elements (Dy^{3+}, Ce^{3+}, Eu^{3+}, Ho^{3+}, Pr^{3+}, Tb^{3+}) are optimized according to the density of the dopants. In line with this optimization, scintillator materials were produced by the sol-gel method and characterized. The characterization process was carried out separately in three different production stages, namely solution, gel, and final product. In this process, the pH and turbidity values of the solutions were determined. Slightly acidic (pH: 6.1) and fully dissolved solutions were obtained. FTIR analysis was performed to determine organic bonds to the sol-gel material, and DTA-TG thermal analyzes were performed to determine exothermic-endothermic reactions. The heat treatment temperature required to find the correct phase was determined at this stage. The final product was then obtained and characterization was completed using FTIR, XRD, XPS, SEM and PL devices, respectively. When the characterizations are evaluated in detail, it is seen that the produced $Gd_2O_2SO_4$: RE^{3+} nanoparticles are successfully produced in the desired phase structure and nanostructure. In addition, the specific emission spectra and decay times of each of the nanoparticles activated with different rare earth elements have been determined. This clearly shows that the produced scintillators can also be used in different detectors for the intended purpose in digital imaging.

Keywords: Rare earth oxysulfates, nanoparticles, scintillator, digital radiography, photoluminescence (PL)

DİJİTAL RADYOGRAFİ SİSTEMİNİN TASARIMI, GELİŞTİRİLMESİ VE ÜRETİMİ

ÖZ

Sintilatör malzemelerinin geliştirilmesi, yüksek enerji fiziği ve dijital görüntülemede artan malzeme ihtiyacından dolayı önemlidir. Sintilatörlerin bileşimi, her biri farklı uygulamalar için uygun olan organik veya inorganik malzemelerden oluşur. İnorganik kristal sintilatörler, yüksek enerji radyasyonu için üstün enerji çözünürlüğü ve sertlikleri nedeniyle yaygın olarak kullanılmaktadır. Tez kapsamında, saf ve nadir toprak elementleri (Dy^{3+}, Ce^{3+}, Eu^{3+}, Ho^{3+}, Pr^{3+}, Tb^{3+}) ile katkılandırılmış inorganik $Gd_2O_2SO_4$ fosforesans nanopartiküller katkı elementi yoğunluğuna göre optimize edilmiştir. Bu optimizasyon doğrultusunda, sintilatör malzemeler sol-jel yöntemiyle üretilmiş ve karakterizasyonları gerçekleştirilmiştir. Karakterizasyon işlemi solüsyon, jel ve nihai ürün olmak üzere üç farklı üretim aşamasında ayrı ayrı gerçekleştirilmiştir. Bu süreçte, solüsyonların pH ve bulanıklık değerleri tespit edilmiş, hafif asidik özellikte (pH: 6.1) ve tam çözünmüş solüsyonlar elde edilmiştir. Solüsyondan jel haline dönüşen malzemeye organik bağların belirlenmesi için FTIR analizi, ekzotermik-endotermik tepkimeleri belirlemek için ise DTA-TG termal analizleri yapılmıştır. Bu aşamada doğru fazı bulmak için gerekli ısıl işlem sıcaklığı belirlenmiştir. Ardından nihai ürün elde edilmiş ve sırasıyla FTIR, XRD, XPS, SEM ve PL cihazları kullanılarak karakterizasyon işlemi tamamlanmıştır. Karakterizasyonlar detaylı bir şekilde değerlendirildiğinde, üretilen $Gd_2O_2SO_4$: RE^{3+} nanopartiküllerin istenilen faz yapısı ve nano yapıda başarılı bir şekilde üretildiği görülmüştür. Ayrıca farklı nadir toprak elementleri ile aktive edilen nanopartiküllerin, her birinin kendine özgü emisyon spektrumları ve bozulma süreleri tespit edilmiştir. Bu durum, üretilen sintilatörün, dijital görüntülemede, istenen amaca yönelik olarak, farklı detektörlerde de kullanılabileceğini açık bir şekilde gösterir.

Anahtar kelimeler: Nadir toprak oksisülfatlar, nanopartiküller, sintilatör, dijital görüntüleme, fotolüminesans, nano malzemeler

CONTENTS

Page

Ph.D. THESIS EXAMINATION RESULT FORM ii
ACKNOWLEDGMENTS iii
ABSTRACT iv
ÖZ v
LIST OF FIGURES ix
LIST OF TABLES xii

CHAPTER ONE – INTRODUCTION 1

1.1 General 1
1.2 Organization of the Thesis 5

CHAPTER TWO – THEORETICAL BACKGROUND 7

2.1 Radiation and Matter 7
2.1.1 Photons 9
2.1.2 X-Ray 10
2.1.3 Interaction Between Matter and Radiation 12
2.1.4 Types of Particle Interactions 13
2.2 Types of Detectors Used in Digital Radiography Systems 14
2.2.1 Gas-Filled Detectors 14
2.2.2 Liquid Filled Detectors 14
2.2.3 Solid State Detectors 15
2.2.4 Scintillation Detectors 15
2.3 Scintillation Mechanism and Scintillator Properties 16
2.3.1 Scintillation Mechanism 16
2.3.1.1 Light yield 18
2.3.1.2 Rise and Decay Times 18
2.3.1.3 Quenching 19
2.3.1.4 Density and Atomic Weight 19
2.3.1.5 Mechanical Properties and Stability 19
2.3.1.6 Optical Properties 20

2.3.1.7 Phosphorescence or Afterglow....20
2.3.1.8 Temperature Dependence....20
2.3.1.9 Radiation Damage....21
2.3.1.10 Scintillation Efficiency....21
2.4 Scintillator Types....21
2.4.1 Organic Scintillator....22
2.4.2 Inorganic Scintillator....22
2.4.2.1 Scintillation Mechanism....22
2.4.2.1.1 Exciton Luminescence....23
2.4.2.1.2 Dopant Luminescence. Sometimes....24
2.4.2.1.3 Core Valence Band Luminescence....24
2.4.2.2 Some Common Inorganic Scintillators....24
2.5 Luminescence of Phosphors....25
2.5.1 Quantum Mechanical Description....26
2.5.2 Jablonski Diagram....30
2.5.3 Luminescence of Rare Earth Ions....32
2.5.3.1 Electronic Configuration....32
2.5.3.2 Electronic Processes Leading to Luminescence in Lanthanides....34
2.6 Imaging Devices....35
2.6.1 Conventional Imaging....36
2.6.2 Electronic Imaging....36
2.6.3 Charged Coupled Devices....37
2.6.4 Direct Conversion....37
2.6.5 Indirect Conversion....38

CHAPTER THREE – EXPERIMENTAL PROCEDURE....40

3.1 Preparation of Nanoparticles by Sol-Gel Technology....40
3.1.1 Sol-Gel Techniques....40
3.1.2 Material and Methodology....40
3.3 Characterization....45
3.3.1 Solution Characterization....45
3.3.1.1 The pH Measurement....45

3.3.1.2 Turbidity Measurement.....46
3.3.2 Material Characterization.....46
3.3.2.1 Differential Thermal Analysis-Thermogravimetry (DTA-TG).....46
3.3.2.2 Fourier Transform-Infrared Spectroscopy (FTIR).....47
3.3.2.4 X-ray Photoelectron Spectroscopy (XPS).....48
3.3.2.5 X-ray Diffraction Spectroscopy (XRD).....49
3.3.2.6 Scanning Electron Microscopy (SEM).....49
3.3.2.7 Photoluminescence (PL) and Decay Time Measurements.....50

CHAPTER FOUR – RESULTS AND DISCUSSION.....52

4.1 Solution Characteristics.....52
4.1.1 pH Results.....52
4.1.2 Turbidity Results.....53
4.2 Material Characterization.....54
4.2.1 Differential Thermal and Thermogravimetric Analysis (DTA-TGA).....54
4.2.2 FTIR Analysis.....56
4.2.3 Phase Analysis (XRD).....59
4.2.4 Elemental Analysis of Nanoparticles (XPS).....63
4.2.5 Surface Morphologies of Nanoparticles (SEM).....73
4.2.6. Luminescence Properties of Nanoparticles.....75
4.2.6.1 Photoluminescence Properties of Nanoparticles.....75
4.2.6.2 Decay Time Measurements of Nanoparticles.....85

CHAPTER FIVE - CONCLUSION.....92

5.1 Conclusion.....92

REFERENCES.....96

LIST OF FIGURES

Page

Figure 2.1 Electromagnetic spectrum 9
Figure 2.2 Sketch of a typical x-ray tube 11
Figure 2.3 Physical process of generation of characteristic x-rays and Bremsstrahlung 11
Figure 2.4 A typical x-ray tube spectrum showing Bremsstrahlung continuum and peaks corresponding to characteristic x-rays 12
Figure 2.5 Principle of production of prompt and delayed scintillation light by incident radiation 17
Figure 2.6 Time profile of light pulse 18
Figure 2.7 Schematic representation of exciton luminescence in an inorganic scintillator 23
Figure 2.8 Principle of dopant luminescence in an inorganic scintillator 24
Figure 2.9 A schematic illustration of a configurational coordinate model. The two curves are modified by repulsion near the intersection. The vertical broken lines A ↔ B 27
Figure 2.10 Discrete energy levels, each having the energy of ħω and the wave functions $\Psi 0e$ and Ψmg of harmonic oscillators indicating the two states where v_0 means the frequency at the emission peak 29
Figure 2.11 Jablonski diagram 30
Figure 2.12 Ground State Electronic Configurations of Trivalent Rare-Earth Ions 33
Figure 2.13 Energy levels of trivalent lanthanide ions including term symbols 35
Figure 2.14 Schematic of a typical CCD working in direct detection mode with front illumination 38
Figure 2.15 Sketch of an indirect CCD for x-ray imaging 39
Figure 3.1 Glovebox system for preparation of solutions 43
Figure 3.3 Steps of the heat treatment process of the $Gd_2O_2SO_4$: RE nanoparticles 44
Figure 3.5 Sample Analysis Process 47
Figure 3.7 Principle of x-ray photoelectron spectroscopy 48

Figure 3.8 A simple XPS photoelectron spectrum. Each peak corresponds to emission of photoelectrons from an atomic level. A typical spectrum contains a number of peaks corresponding to different elements in the sample 48
Figure 3.12 The Schematic representation of an SEM ("Scanning Electron Microscopy 50
Figure 3.13 The internal structure and the path the light follows of the FLSP920 system 51
Figure 4.1 The DTA-TGA curves of $Gd_2O_2SO_4$ xerogels 55
Figure 4.2 FTIR analyses of $Gd_2O_2SO_4$ solution 57
Figure 4.3 FTIR analyses of $Gd_2O_2SO_4$ sol, gel, and nanoparticles at a different temperature.....58
Figure 4.4 Pure $Gd_2O_2SO_4$ phase structure 59
Figure 4.5 The XRD pattern of Dy^{3+} doped $Gd_2O_2SO_4$ nanoparticles 60
Figure 4.6 The XRD pattern of Ce^{3+}doped $Gd_2O_2SO_4$ nanoparticles.....60
Figure 4.7 The XRD pattern of Eu^{3+} doped $Gd_2O_2SO_4$ nanoparticles.....61
Figure 4.8 The XRD pattern of Ho^{3+} doped $Gd_2O_2SO_4$ nanoparticles 61
Figure 4.9 The XRD pattern of Pr^{3+} doped $Gd_2O_2SO_4$ nanoparticles 62
Figure 4.10 The XRD pattern of Tb^{3+} doped $Gd_2O_2SO_4$ nanoparticles.....62
Figure 4.11 The XPS spectra of the $Gd_2O_2SO_4$ nanoparticles 64
Figure 4.12 The XPS spectra of Dy^{3+} doped $Gd_2O_2SO_4$ nanoparticles (scanned between 0-1400 eV).....65
Figure 4.13 The spectra of Dy^{3+} binding energy (a close inside to Dy^{3+} peak) 65
Figure 4.14 The XPS spectra of Ce^{3+} doped $Gd_2O_2SO_4$ nanoparticles (scanned between 0-1400 eV). 66
Figure 4.15 The spectra of Ce^{3+} binding energy (a close inside to Ce^{3+} peak) 66
Figure 4.16 The XPS spectra of Eu^{3+} doped $Gd_2O_2SO_4$ nanoparticles (scanned between 0-1400 eV) 68
Figure 4.17 The spectra of Eu^{3+} binding energy (a close inside to Eu^{3+} peak) 68
Figure 4.18 The XPS spectra of Ho^{3+} doped $Gd_2O_2SO_4$ nanoparticles (scanned between 0-1400 eV).....69
Figure 4.19 The spectra of Ho^{3+} binding energy (a close inside to Ho^{3+} peak) 69

Figure 4.20 The XPS spectra of Pr^{3+} doped $Gd_2O_2SO_4$ nanoparticles (scanned between 0-1400 eV) 70
Figure 4.21 The spectra of Pr^{3+} binding energy (a close inside to Pr^{3+} peak)..... 70
Figure 4.22 The XPS spectra of Tb^{3+} doped $Gd_2O_2SO_4$ nanoparticles (scanned between 0-1400 eV) 71
Figure 4.23 The spectra of Tb^{3+} binding energy (a close inside to Tb^{3+} peak)..... 71
Figure 4.24 The SEM images of $Gd_2O_2SO_4$: RE^{3+} (Ce, Dy, Eu, Ho, Pr, Tb) nanoparticles..... 75
Figure 4.25 The emission spectrum of $Gd_2O_2SO_4$ nanoparticles, depending on the Dy^{3+} concentration 77
Figure 4.26 Excitation and emission spectra of the $Gd_2O_2SO_4$: Ce^{3+} doped nanoparticles..... 78
Figure 4.27 Excitation and emission spectra of the $Gd_2O_2SO_4$: Eu^{3+} doped nanoparticles..... 79
Figure 4.28 The partial energy diagram of Eu^{3+} ions in the $Gd_2O_2SO_4$ nanoparticles showing the luminescence mechanism. 80
Figure 4.29 Excitation and emission spectra of the $Gd_2O_2SO_4$: Tb^{3+} doped nanoparticles..... 81
Figure 4.30 The partial energy diagram of Tb^{3+} ions in the $Gd_2O_2SO_4$ nanoparticles showing the luminescence mechanism. 82
Figure 4.31 Excitation and emission spectra of the $Gd_2O_2SO_4$: Pr^{3+} doped nanoparticles..... 83
Figure 4.32 Excitation and emission spectra of the $Gd_2O_2SO_4$: Ho^{3+} doped nanoparticles..... 84
Figure 4.33 The partial energy diagram of Ho^{3+} ions in the $Gd_2O_2SO_4$ nanoparticles showing the luminescence mechanism. 85
Figure 4.34 PL decay curves of the $Gd_2O_2SO_4$: Ce^{3+} nanoparticles 87
Figure 4.35 PL decay curves of the $Gd_2O_2SO_4$: Dy^{3+} nanoparticles..... 87
Figure 4.36 PL decay curves of the $Gd_2O_2SO_4$: Eu^{3+} nanoparticles 88
Figure 4.37 PL decay curves of the $Gd_2O_2SO_4$: Ho^{3+} nanoparticles..... 88
Figure 4.38 PL decay curves of the $Gd_2O_2SO_4$: Tb^{3+} nanoparticles 89
Figure 4.39 PL decay curves of the $Gd_2O_2SO_4$: Pr^{3+} nanoparticles..... 89

LIST OF TABLES

Page

Table 3.1 The chemicals used for production of the nanoparticles scintillators 42

Table 4.1 The characteristic results of the solutions.....52

Table 4.2 The XPS results (binding energy and weight %) of $Gd_2O_2SO_4$ nanophosphors.....64

Table 4.3 The XPS results (binding energy and weight %) of $Gd_2O_2SO_4:Dy^{3+}$ nanophosphors.....72

Table 4.4 Excitation and emission wavelength, and decay time measurement results of the nanophosphors with standard deviations and percentage distribution 86

CHAPTER ONE
INTRODUCTION

1.1 General

Phosphors activated with rare earth elements are strongly preferred for technological applications due to their high luminescence efficiency, color purity and variety, long emission wavelength values, adjustable decay times and densities (Ye, Xiao, Pan, Ma, & Zhang, 2010; G. Li et al., 2011; Shang et al., 2011; Gai, Li, Yang, & Lin, 2013). The luminescence properties of rare earth phosphors are largely dependent on their composition, morphology, size, and crystallinity (J.-G. Li, Li, Sun, & Ishigaki, 2008; Zhu, Li, Li, & Sun, 2009). Host materials are very important in the photoluminescence of phosphor materials. Because the effects of size and co-doping on the luminescence of rare earth doped phosphors depend on host materials (Jian et al., 2017).

Rare-earth oxysulfates ($Ln_2O_2SO_4$) have attracted increasing interest in recent years due to their significant luminescence and specific magnetic properties, as well as significant applications in large volume oxygen storage, providing eight times more oxygen storage capacity than conventional cerium-based forms (Machida, Kawamura, Ito, & Ikeue, 2005; X. Liu et al., 2012; G. Chen et al., 2014). In the literature, $Ln_2O_2SO_4$ have proven to be outstanding host materials. Until now, various rare earth elements and production methods have been used to synthesize $Ln_2O_2SO_4$ based phosphors. Emission intensities of nanoscale phosphors are stronger than mass phosphors. As the size of the phosphor materials decreases, the light efficiency increases. In addition, much work has been done in the literature where the different rare earth ions involved in the structure of rare earth phosphors have been replaced by lattice ions replacing the lattice structure of the lattice (Haynes & Brown, 1968; Nathans & Wendlandt, 1962; Porcher, Svoronos, Leskelä, & Hölsä, 1983; G. Chen et al., 2014).

S. A. Ossani et al., in 2017, used a homogenous precipitation method optimized for the synthesis of spherical and well dispersed pure $Ln_2O_2SO_4$ (Ln = Gd, Ho, Dy, and Lu) nanoparticles using lanthanide sulfates and urea synthesized as starting material. The particle size is between 500 nm and 3.5 μm. This method also allows $Ln_2O_2SO_4$ to be obtained without the use of H_2S, an extremely toxic and disturbing gas. The synthesized $Ln_2O_2SO_4$ / Ln_2O_2S can be used as a release for digital medical imaging applications and as an additive with oxygen storage or luminescent centers (Osseni, Denisenko, Fatombi, Sal'nikova, & Andreev, 2017).

M. Machida and colleagues in 2007 examined the structure of praseodymium host in a series of large-capacity oxygen storage materials using redox between $Ln_2O_2SO_4$ and Ln_2O_2S. The features of the Pr system were investigated by thermogravimetric analysis, X-ray photoelectron spectroscopy, X-ray diffraction, Rietveld analysis, Fourier transformation infrared spectroscopy and Raman spectroscopy. Unlike other $Ln_2O_2SO_4$ / Ln_2O_2S, the Pr system contained a significant amount of tetravalent cation (Pr^{4+}) on the surface. The soft redox between Pr^{3+} and Pr^{4+} will promote oxidation of the total Pr_2O_2S to $Pr_2O_2SO_4$ (Machida, Kawano, Eto, Zhang, & Ikeue, 2007).

Sung Woo Lee and his colleagues thought that in 2017 it is very important to develop a new morphology material, improve functional performance and find new applications. With this idea, monoclinic $Sm_2O_2SO_4$ nanoparticles were prepared. They have studied the basic physicochemical properties. $Sm_2O_2SO_4$ nano-plates have been found workable for visible-NIR absorption and X-ray photoelectron spectroscopy (Lee, Jeong, Ra, & Sohn, 2017).

In 2008, K. Ikeue and colleagues examined the redox properties of $Ln_2O_2SO_4$ (Ln: La and Pr) materials. They compared the effects of La and Pr elements (Ikeue, Kawano, Eto, Zhang, & Machida, 2008). In 2008, T. Kijima et al. Tried methods to increase Eu^{3+} emission in $Y_2O_2SO_4$: Eu^{3+} phosphorus. They produced the products in different concentrations and morphologies and evaluated their results. The highest Eu^{3+} emission is presumably due to the specific deformation of the sulfate groups induced by the conversion of the concentric dodecyl-sulfate layers to the flat sulfate

layers on the oxysulfate framework upon calcination (Kijima, Shinbori, Sekita, Uota, & Sakai, 2008). The same group proceeded with phosphorus $Y_2O_2SO_4$: Tb. In 2009, T. Kijima and colleagues produced and compared $Y_2O_2SO_4$: Tb^{3+} flat layered (S-type) and concentric layered (C-type) structures. Tb^{3+} doped oxysulphates exhibited luminescence bands which tend to reach or bend to a maximum saturation at different molar Tb^{3+} additions, including $^5D_4 \rightarrow {}^7F_5$ transition (Kijima, Isayama, Sekita, Uota, & Sakai, 2009).

R. V. Rodrigues and colleagues synthesized yellow emitting Dy_2O_2S and $Dy_2O_2SO_4$ phosphors in 2016. The arsenic phosphors are characterized using thermo-gravimetry (TG / DTG), X-ray powder diffraction (XRD), Fourier transforms infrared (FTIR) and Raman spectroscopy. Narrow emission bands were assigned to Dy^{3+} ion transitions within $^4F_{9/2} \rightarrow {}^6H_J$ configuration. The result is that Dy^{3+} phosphorus yellow emission color is a suitable material for Dy_2O_2S applications in LEDs (Rodrigues et al., 2016). Xiao Zhu Huang and his colleagues produced two-dimensional nano-sheets of $La_2O_2SO_4$ phosphors in 2013. Luminescence studies were performed by X-ray spectroscopy. In the study, the formation process of the nano leaves in the dissolved salts is also investigated. The luminescence properties of the obtained $La_2O_2SO_4$ nano-sheets were investigated doped with Eu^{3+} at different concentrations. Nano-sheets were found to exhibit good mono-chromaticity with high color saturation (Huang, Liu, Yang, & Tian, 2013). Wei Hua Shen and Shuichi Naito synthesized $La_2O_2SO_4$: Ce^{3+} and La_2O_2S: Ce^{3+} phosphors in 2014 and evaluated their results. The study shows that the addition of Ce^{3+} can support the oxidation and reduction process between La_2O_2S and $La_2O_2SO_4$. The Ce^{3+} doped oxygen storage system showed that sulfur leakage did not occur during redox cycling (Shen & Naito, 2014).

Xiaohe Liu and his colleagues in 2012 developed a general and easy synthetic strategy for the production of a series of highly efficient and uniform $RE_2O_2SO_4$ (RE = La, Pr, Nd, Sm, Eu, Gd, Tb, Dy, Y, Ho, and Yb) hollow spheres. It is believed that the synthetic strategy can provide a general and efficient way to synthesize and rationally design another inorganic micro/ nanospheres with hollow cores. It is expected that this rare earth oxysulfate and oxide hollow spheres will bring new

opportunities for further basic research as much as for technological applications in optical devices, nanoscale reactors, magnetic devices and oxygen storage materials, especially rare earth oxysulfates (X. Liu et al., 2012).

L. Song and colleagues synthesized $Gd_2O_2SO_4$: Tb^{3+} nanopieces in mixed gas sulfur dioxide and air at 1000 ° C in 2014 with a combined approach of electrospinning and calcination. 230 nm light-stimulated nanopieces showed excellent green luminescence with the strongest emission peak at 545 nm due to energy transfer from $^5D_4$ to $^7F_5$. In addition, the effects of the addition of alkali metal ions on the nanopieces luminescence have been investigated. Emission densities were increased by the addition of alkali metal ions, especially for $Gd_2O_2SO_4$: Tb^{3+}/ Li^+ (Song, Du, Jiang, Cao, & Xiong, 2014).

J. Lian and colleagues produced $Gd_2O_2SO_4$: Eu^{3+} phosphors by hydrothermal synthesis in 2014. They use different amounts of urea as the precipitating material. The synthesized products were characterized by XRD, SEM, FTIR, DTA-TG and photoluminescence spectra. The effect of the amount of urea on the structure and microstructure was studied. The $Gd_2O_2SO_4$ phosphor particles were found to be spherical and homogeneously dispersed, about 1-3 μm in size. PL spectra show that the strongest emission peaks for $Gd_2O_2SO_4$: Eu^{3+} spherical phosphorus are found at 620 nm under 270 nm light excitation, which corresponds to the transition of Eu^{3+} ions from $^5D_0$ to $^7F_2$ (J. Lian, Liu, Wang, & Sun, 2014). S. W. Kim et al. in 2009 synthesized $Gd_2O_2SO_4$: Eu^{3+} phosphors using the flux method. This method uses alkali metal sulfate such as Na_2SO_4 and $0.6Li_2SO_4$-$0.4Na_2SO_4$ eutectic mixture. Investigated the effect of alkaline metal sulfates on photoluminescence properties (Kim, Masui, & Imanaka, 2009).

In 2011, J. B. Lian and colleagues synthesized $Gd_2O_2SO_4$: Dy^{3+} by a homogeneous precipitation method. Photoluminescence spectroscopy reveals that the strongest and second emission peaks are at 575 nm and 485 nm under UV light excitation at 277 nm, corresponding to $^4F_{9/2} \rightarrow {}^6H_{13/2}$ and $^4F_{9/2} \rightarrow {}^6H_{15/2}$ transitions. The extinguishing concentration of Dy^{3+} ions is 1 mole % (J. B. Lian, Wang, Wang, & Li, 2011).

F. Liu et al., in 2016, produced $Gd_2O_2SO_4$: Yb^{3+}, Er^{3+} nanoparticles by hydrothermal synthesis. Up-conversion luminescence mechanisms of the produced phosphors were studied. Under 980 nm infrared light stimulation, $Gd_2O_2SO_4$: Yb^{3+}, Er^{3+} nanoparticles have the strongest red chore (664 nm), corresponding to $^4F_{9/2} \rightarrow {}^4I_{15/2}$ transitions of Er^{3+} ions. In addition, $^4S_{3/2} \rightarrow {}^4I_{15/2}$ and $^2H_{11/2} \rightarrow {}^4I_{15/2}$ are located at 546 nm and 526 nm from the Er^{3+} ion pass. $Gd_2O_2SO_4$: Yb^{3+}, Er^{3+} nanoparticles show the highest luminescence when the ratio of Er^{3+} ions reaches 2% (F. Liu et al., 2016).

In addition to all these literature studies, our own studies, the production of $Gd_2O_2SO_4$: Tb^{3+}, $Gd_2O_2SO_4$: Eu^{3+}, $Gd_2O_2SO_4$: Pr^{3+} and pure $Gd_2O_2SO_4$ phosphors, were carried out in 2017 (I Aritman et al., 2017a, 2017b, 2017c; Idil Aritman et al., 2017). The synthesis and characterization of all these phosphors have been successfully completed. The results of these studies are given in detail in the conclusions section of the thesis. In the light of all this literature, $Gd_2O_2SO_4$: x %RE^{3+} nanoparticle phosphors have not been previously studied by the sol-gel method. These phosphors are generally produced by the solid-state reaction, polymerization complex method, hydrothermal method, chemical vapor deposition, and molten salt method. In addition, in this doctoral dissertation, a detailed study was carried out in terms of both rare earth element type, production method, and contribution rates.

1.2 Organization of the Thesis

This thesis consists of five parts. In the first part, general information about the phosphorus material I have worked within the scope of the thesis and the purpose of the thesis are explained. It is mentioned in the technological applications what this product is preferred for. In addition, a good evaluation of the work done in this issue has been made in the literature and the original value of the thesis has been mentioned. In the second part, the theoretical information about the thesis is given. Detector types and features used in digital imaging are detailed. Radiation and substance are introduced. Mechanism and types of the scintillator are explained. The luminescence of phosphors is described in detail through the quantum mechanics approach and electronic configuration. Finally, it refers to imaging devices and the second part is

terminated. In the third chapter, there are experimental works carried out within the scope of the thesis. The production and characterization tools used in the test procedure are described in detail. In the fourth section, the experimental results are given. Experimental results are discussed and interpreted in the light of the literature. The outcome and future plans are summarized in Chapter Five.

CHAPTER TWO
THEORETICAL BACKGROUND

2.1 Radiation and Matter

Mass and energy are the two entities that make up the Universe. At the most basic level, these two entities sometimes represent the only reality that shows itself as mass and sometimes as energy (Davisson, 1965). Einstein's famous mass-energy relationship is complexly interrelated with $E = mc^2$. Like matter, energy has the ability to move from one point to another on the fringe through particles or waves. These energy carriers always originate from a source and continue to go far enough to lose their absorption. "Radiation" is used to describe the transport of mass and energy. When a large number of electrons interact with a large number of atoms, the dominant interaction mode will lead to the ionization of the atoms. Sometimes the radiation is characterized by wave and particle properties. The reason for this may be, according to modern physics, to associate a mass or a wavelength to each particle. This implies that a particle with mass can function as a wave and participate in the formation of interference and diffraction patterns. On the other hand, the light that can be well described by the wave character consists of photons composed of non-mass particles (Davisson, 1965; Spinks & Woods, 1976; Zlatev, Wang, & Steinhardt, 1999). Therefore, we can conclude that radiation should not be characterized based on particle and wave properties.

$$E = h\nu \tag{2.1}$$

where h = 6.626 × 10-34Js Planck constant determined by Max Planck. It is now considered a universal constant. The Planck constant has a very important place in the quantum space. The frequency (ν) of the electromagnetic radiation and its wavelength (λ) is related to the propagation velocity at c vacuum with $c = \nu\lambda$.

$$v = n\nu\lambda \tag{2.2}$$

If the radiation is traveling through another medium, the velocity should be calculated from the equation (2.2), where n is the refractive index of the medium. The refraction index of most materials is a non-linear dependence of the radiation frequency.

These experiments and the resulting theoretical models have sometimes verified that radiation acts as particles and is not continuous waves. On the other hand, there were effects such as parasitic, which could only be explained if they were thought to have continuous wave characteristics of the light. In order to contribute to this confusion, Broglie made it clear in 1920 that sometimes particles behave like waves. He proposed that one could associate a wavelength to any particle having momentum p through the relation

$$\lambda = h/p \tag{2.3}$$

for a particle moving close to the speed of light and rest mass m0, the above equation can be written as

$$\lambda = h/m0v * \sqrt{(1-v2/c2)} \tag{2.4}$$

for slow-moving particles with v <<c, the Broglie relation reduces to

$$\lambda = h/mv \tag{2.5}$$

De Broglie's theory was experimentally confirmed in Bell Laboratories where electron diffraction patterns consistent with the wave picture were observed. Based on these experiments and theoretical explanations, it is now believed that all entities in the scene have particle-like and wave-like properties. In simple terms, particles can behave in waves and waves can behave like particles. This principle, known as the wave-particle duality, plays a central role in the development of quantum physics (Eidelman & Shwartz, 2012).

2.1.1 Photons

A photoreceptor, such as an eye, is known as the first subatomic particle discovered by photons, which carry enough energy to warn a single molecule in the cell. In 1905, the German physicist Albert Einstein proposed that the nature of the bifurcation is quantized as it examines the photoelectric phenomenon. Thus, using Max Planck's idea of quanta, he revealed that energy was transferred with small energy packages called quanta. When the year 1926 came, these quanta or small energy packages were named photon by the American chemist Gilbert Lewis. That is, the photon is the smallest possible energy part of a light wave. The photons are massless, have no electric charge and are stable. In free space, the photon travels at light speed. A photon represents a quantum electromagnetic energy. The photon is regarded as a basic particle in the Standard Model of the particle physics. Photons do not correspond only to visible light. In fact, the light covers a very narrow region of the full energy spectrum (see Figure 2.1).

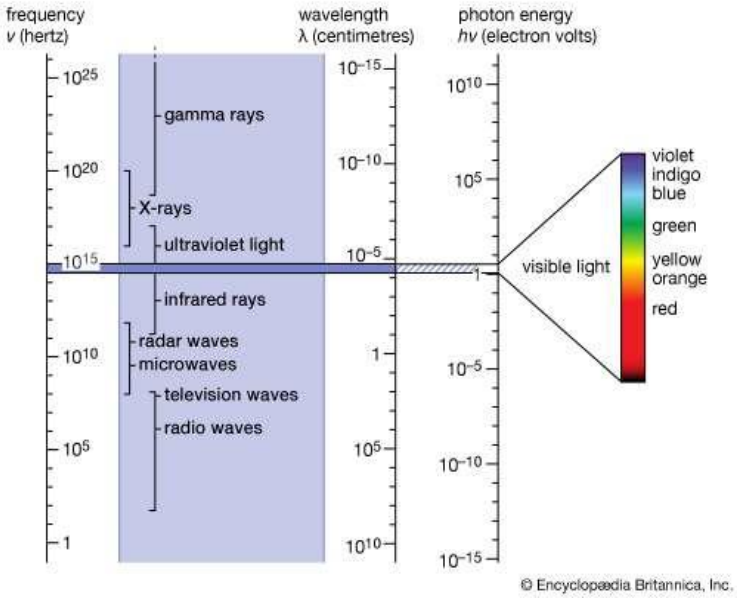

Figure 2.1 Electromagnetic spectrum (Electromagnetic spectrum n.d.)

There are many ways to produce photons that are not in visible light regions of the spectrum. For example, when a charged particle moves, electromagnetic waves propagate around it. These waves are considered the underlying electromagnetic field

stimulus, and a quantum of these excitations is called a photon. The energy carried by a photon can be absorbed in a variety of ways by other particles that interact. In addition, like other particles, a photon can be dispersed from other particles and exposed to gravitational pull. An important feature of photons is their momentum transport, even though they are not resting masses. E energy, the frequency ν, and the momentum of a photon with wavelength λ are given by,

$$p_\gamma = E/c = h\nu/c = h/\lambda \tag{2.6}$$

Photons play a crucial role not only in physics but also in engineering, medical diagnosis, and treatment. In medical diagnostics, x-rays are used to image the internal organs of the body ("Light As Electromagnetic Radiation," n.d.).

2.1.2 X-Ray

X rays are high-energy photons and can cause significant damage to the tissues, they are produced and used in controlled laboratory environments. The production of X-rays, high-speed electrons (see Figure 2.2) is a relatively simple process bombardment of a high Z targets (ie, an element with multiple protons such as tungsten or molybdenum). Two x-ray beams are produced: Bremsstrahlung and characteristic x-rays.

Bremsstrahlung refers to the radiation emitted by charged particles as they slow down in an environment (see Figure 2.3). In the case of X-rays, high-energy electrons slow down rapidly in the target material and thus emit Bremsstrahlung. There is a continuous energy spectrum of irradiated x-ray photons (see Fig. 2.4) because there are no quantized energy transitions in this process.

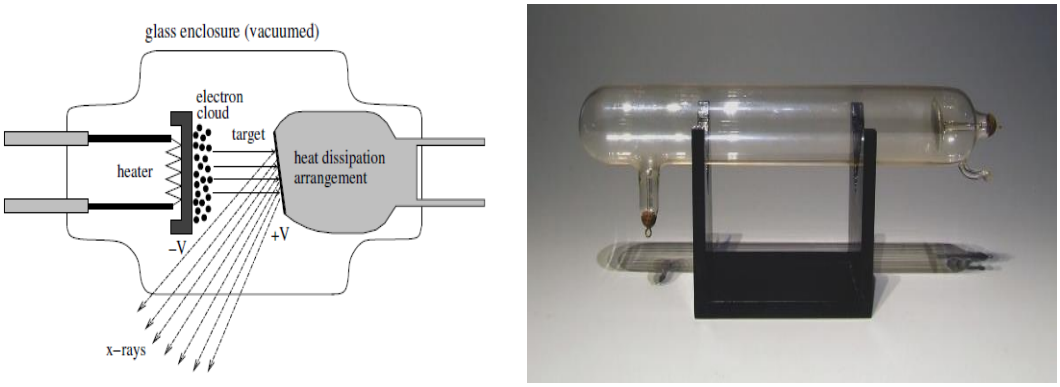

Figure 2.2 Sketch of a typical x-ray tube (X-Ray tubes, n.d.)

Bremsstrahlung is the x-rays usually used to produce images of internal objects. The electrons at the target can reach enough energy to pull them away from the atoms of the atoms leaving them to the unstable states of the target electrons. To regain atomic stability, electrons at high energy levels fill these gaps rapidly. Since the energy of these electrons is higher than the energy required to stay in the new orbit, excess energy is emitted as x-ray photons (see Figure 2.3). These photons, which have characteristic energies to the difference in atomic energy levels, are said to form characteristic x-rays (see Figure 2.4).

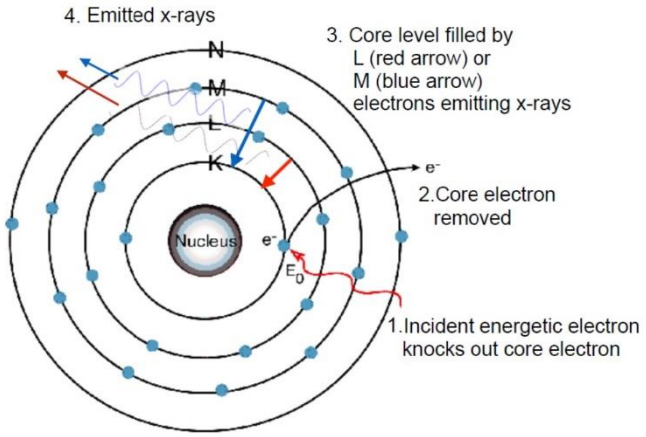

Figure 2.3 Physical process of generation of characteristic x-rays and Bremsstrahlung (Kent, n.d.)

X-ray tube spectra generally have more than one characteristic x-ray peak because a series of electronic transitions are possible after the gap created in one of the inner electronic shells. If an electron is disconnected from the innermost K-shell, the gap

can in principle be filled by any of the electrons in the outer shell. If they jump to fill an electron cavity from the L-shell, a photon with an energy of Eγ = EL-EK is emitted. Such a large number of photons appear as a distinct peak in the spectrum. Such a summit is often called the Kα peak. The Kβ peak is the result of the passages of M-shell electrons to the K-shell giving photons with Eγ = EM-EK energy (see Figure 2.3).

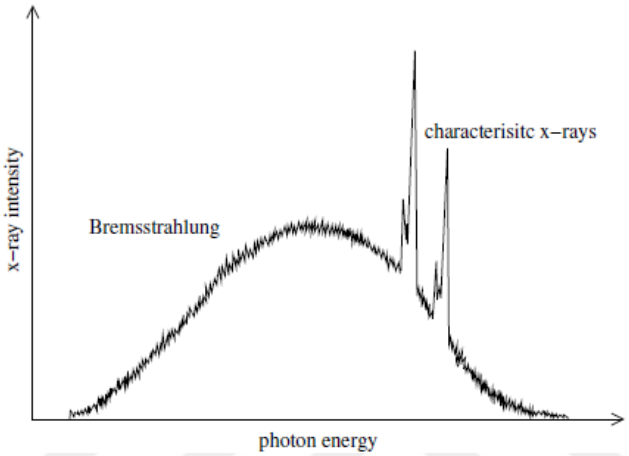

Figure 2.4 A typical x-ray tube spectrum showing Bremsstrahlung continuum and peaks corresponding to characteristic x-rays (Ahmed, 2007)

2.1.3 Interaction Between Matter and Radiation

When we want to perceive or measure radiation, we have to examine the change in the system configuration by interacting with some amount of material. According to the present understanding, it is not possible to detect radiation or measure its properties without allowing it to interact with a measuring device. In fact, this can be specified as a universal rule for any measurement. Even the five senses are no exception. For example, photons perceive cells in the retina reflected from the objects of the present. Without such interactions, we cannot see anything. The same is true for radiation detectors that use the form of radiation interaction to produce a measurable signal. This signal is then used to reverse engineer the properties of the radiation. For example, the plate stains when x-ray photons strike a photographic plate after passing through an object. The photons that do not pass through the absorbent material in the object do not reach the photo plate. The density created by the fogging of the photographic plate

creates a two-dimensional image of the object, and in this way, the photographic plate acts as a position sensitive detector. Although such a radiation detection method is still widely used, it is not very accurate or very accurate to measure the properties of radiation such as energy and flux. So-called electronic detectors provide an alternative and better means of detecting and measuring radiation. An electronic detector uses a sensing medium such as a gas to generate an electric signal as the radiation passes. It can be used to characterize the electrical signal, radiation, and properties. For this reason, a necessary step to create a detector is to understand the interaction mechanisms of the radiation in the sensing environment (Ahmed, 2007; Eidelman & Shwartz, 2012; Leroy & Rancoita, 2011).

2.1.4 Types of Particle Interactions

Many scientists have worked to establish the bases of different interaction mechanisms; these studies are understood through means such as quantum mechanics, quantum electrodynamics and quantum chromodynamics. When the radiation interacts with a sensing medium, it stores some or the entire medium in the particles. This is a form of stimulation. This excitation can form a basis for the generation of a signal that can be perceived and measured by the processing electron. Some of these excitements are:

- Ionization
- Scintillation
- Warning of lattice vibrations
- Dispersion of Cooper pairs in superconductors
- Formation of overheated droplets in superfluids
- Alert of optical conditions

The most commonly used excitation mechanisms for particle detection are ionization and scintillation (Ahmed, 2007).

2.2 Types of Detectors Used in Digital Radiography Systems

Different types of detectors are used in different electronic devices intended for the purpose. Optimum parameters must be selected in order to achieve the desired effect in electronic systems. For this purpose, detectors are classified according to the materials used.

2.2.1 Gas-Filled Detectors

Radiation through a gas may ionize the gas molecules as long as the gas has a higher ionization potential. The pairs of charge produced in this way can be moved in the opposite direction by the application of an external electric field. As a result, a related measuring device can measure an electric pulse. A gas-filled detector is a device that can rapidly and sensitively detect components in a mixture that is subjected to filled processing; can also be placed in the system in spatial and temporal dimensions. At any given moment, the concentration of the substance in the carrier gas is only at several levels. The detector should be in a position where it can detect the values far below it. In addition, since a peak detector has a time interval of 1 second or less while it passes, the detector should be able to show all the detection power over a short period. The detector is required to be able to detect linear and uniform perceptions and to maintain its long-term stability. Among the first detectors used are gas density scales, cataracts, flame detectors and x-ray detectors (Methodology, n.d.).

2.2.2 Liquid Filled Detectors

When the radiation passes through a liquid, it produces charge pairs that can be directed to the electrodes to produce a pulse. The height of the pulse is a good measure of the accumulating energy if the liquid provides a good ratio between the amount of energy deposited and the number of charge pairs generated. There are very well proportioned fluids as they emerge and can, therefore, be used as a sensing medium. Now, we would expect the probability of charge recombination in a liquid to be much

higher than a typical gas. This is true, but we must remember that higher density also allows a larger number of charge pairs to be produced (Saha, 2012).

2.2.3 Solid State Detectors

A semiconductor, the valence band is filled, and the next available energy state is the transmission band, on a higher band separated by a forbidden region. The energy gap between the two zones is one eV. Under normal conditions, there will always be a small number of electrons in the conduction band, depending on the temperature, and the material has a limited degree of conductivity. The cooling of the material reduces the background current (leakage current) by reducing the number of electrons in the conduction band and makes it easier to detect extra excitation due to gamma-ray interactions.

When you are promoted to an electron-conducting band, the gap remains. This space is effectively positively charged and is referred to as a hole. The holes are also in motion. An electron in the valence band can take its place in the void, so fill the hole. This will leave a gap. In the presence of an external electric field, it can be seen that the hole moved towards the catheter. Both electrons and holes carry a charge; both contribute to the conductivity of the material (Bode, 2009; G. Knoll, 2000).

2.2.4 Scintillation Detectors

In a scintillation detector, a part of the energy that is precipitated by the primary radiation in the detector is converted into light, which turns into an electrical signal. Conceptually, the process can be divided into two parts: the scintillation process itself (energy light), the conversion of light into electrons, and the multiplication of electrons to form a macroscopic signal.

The photons radiate through the passage of matter. When radiation atoms interact with scintillation material atoms, they transfer some of their energy to atoms. Because of this transfer, these excited atoms pass through short-lived excited states. When they

return to the ground, they are most visible in the spectrum and emit photons in ultraviolet regions. This is an alternative to the ionization mechanism for detecting and measuring radiation. The basic steps involved in radiation scintillation detection are:

- Interaction of radiation with scintillation material.
- Energy transfer to the states of the material.
- When the excited electrons are turned to the ground state, results in the emission of light photons.
- Photon collection by the photodetector.
- Signal processing by the associated electronic devices.

The working principle of a photomultiplier tube (PMT) relies on converting a scintillation photon to an electron and then multiplying them by a number of electrons. Photon electron conversion takes place in a thin metallic electrode called the photocathode. The electrons produced in the photocathode are accelerated to a metallic structure in the phototube that gives rise to a large number of electrons due to the photoelectric effect. The produced electrons are then accelerated towards another dynode to multiply the number. The process is repeated many times, allowing electrons to pass through a series of dynodes. The output pulse has a higher magnitude that can be easily measured by the associated electronics (University, 1999; Barlett & Jones, 2010; Johann Zmeskal, 2015)

2.3 Scintillation Mechanism and Scintillator Properties

In this section, the important features of the use of scintillation material in radiation detectors will be explained.

2.3.1 Scintillation Mechanism

Scintillators are also isolators with a large gap between valence and transmission bands. In this type of materials, there are also luminescent centers, which play a central role in producing the scintillation light. A luminescent center usually consists of two

energy levels, in the visible region of the electromagnetic spectrum and the energy of the photons around it (See Figure 2.5). A scintillation photon can be emitted if an electron skips this energy from the center to the lower energy level. The reason may be that there is a radiation-free transfer of energy that is distributed by heat-bearing particles called phonons. When the radiation passes through a scintillator, it transfers some of its energy to the material. If the transferred energy is higher than the band gap of the material, electrons in the valence band may skip to the conduction band. The space left by the electron in the valence band causes the formation of an effective positive charge center called the hole. Both the electron in the conduction band and the hole in the valence band are then free to move in the material. Finally, the electron in the conduction band falls to an energy level below the lower level of the conduction band.

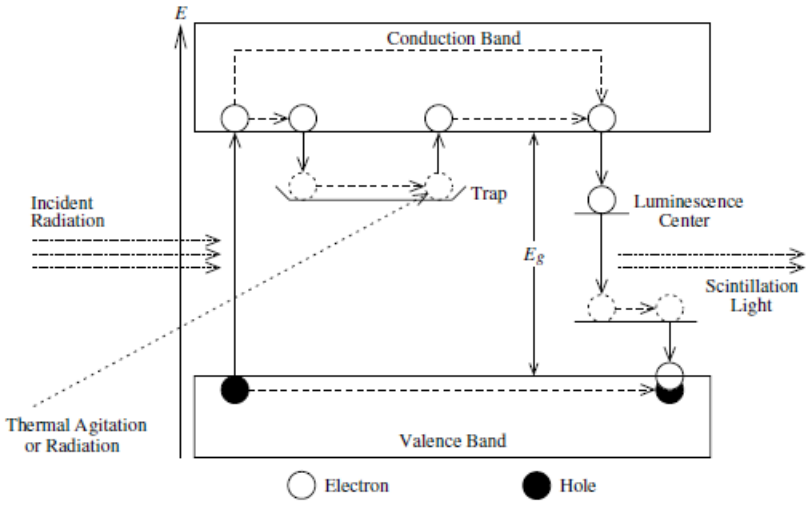

Figure 2.5 Principle of production of prompt and delayed scintillation light by incident radiation (Ahmed, 2007)

If this energy level is the luminescent center of matter, the skipped electron emits a glowing photon or loses its energy through a non-radiative emission. From here, the electron may jump to the valence band and joins with the hole. The electron positioned in the conduction band can also jump to an electron trap. These traps are generally metastable energy states and arise from impurities and defects. The electron held here can stay in this position in time intervals of extending from several nanoseconds to one hour. Following, the electron having enough energy may return to the conduction band

by thermal agitation or other means. From there it can also jump to the luminescent center and cause the scintillation light to spread. These delayed photons constitute what is termed delayed light or phosphorescence (Ahmed, 2007; G. F. Knoll, 1972; Pedrini, 2005; M. J. Weber, 2004).

2.3.1.1 Light yield

Light is one of the most important parameters for an efficient scintillation material. If the light output is not sufficient, the total signal-to-noise ratio of the next photodetector may not be acceptable. Light emission is measured as the number of photons per MeV of absorbed radiation. The main factors effective on scintillation light yield are; scintillation material, event type, particle's energy and temperature (Holl, Lorenz, & Mageras, 1988).

2.3.1.2 Rise and Decay Times

A typical scintillation is given as a variation of the light pulse over time (Figure 2.6). As stated here, the rise time of the light pulse is short in a nanosecond, and the light pulse rises rapidly.

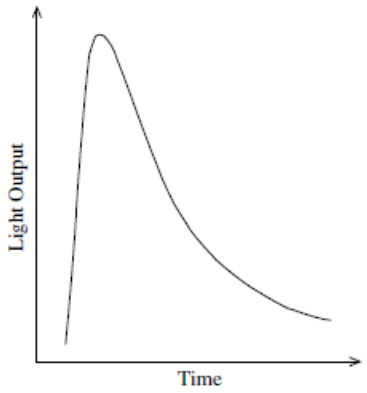

Figure 2.6 Time profile of light pulse (Ahmed, 2007)

In the meantime, the pulse decay is very slow. In fact, there is a problem with their use in detectors because slow decay in scintillators can reduce efficiency. Typical

scintillation decay times can range from several nanoseconds to several milliseconds (Ahmed, 2007; Lippitsch & Draxler, 1993).

2.3.1.3 Quenching

Fluorescent quenching is a process that reduces the fluorescence intensity of a fluorescent material. Various molecular interactions may result in quenching. These include excited state reactions, molecular rearrangements, energy transfer, ground-state complex formation, and collisional quenching. In addition, visible extinction can occur due to the optical properties of the sample. High optical densities or turbidity can cause the fluorescence intensity to decrease (Lakowicz, 1983).

2.3.1.4 Density and Atomic Weight

Scintillation detectors are used to detect any kind of radiation, including γ-rays, electrons, α-particles, and neutrons. The energy changes they have been very important in order for the expressed particles to be detected efficiently. How quickly the particles lose their energy is important. The rate of energy change in the scintillation material is directly related to the atomic weight and density of this material. For example, the detection of light particles such as photons requires that the material have a high effective atomic weight and a high density. For this reason, density and atomic weight should be considered as important factors used to assess the efficiency of the scintillator for a particular type of radiation and energy range of interest (Holl et al., 1988).

2.3.1.5 Mechanical Properties and Stability

Scintillation materials are sensitive to atmospheric changes and storage conditions greatly affect their efficiency. For example, due to the changes in humidity and temperature, the optical properties of some scintillating materials are deteriorating. Similarly, changes in the pressure can cause cracks in the structure of the scintillation material (Rodnyi, 1997).

2.3.1.6 Optical Properties

Scintillation materials have been developed to convert the very short wavelengths to the light in the visible region of the electromagnetic spectrum. The scintillators are able to convert high-energy particles into low-energy photons. The choice of scintillation material is crucial so that efficient optical results can be obtained when photons are detected by the photodetector. Because photons are attenuated after passing through the scintillation material, they cause information loss, which in turn can induce nonlinearities in the detector response. Thus, the optical properties of the utilized material play a very important role in the overall efficiency of the scintillator. The parameter of interest here is the refractive index of the material for the wavelength of the light emitted by the scintillation material (G. F. Knoll, 2000; Pedrini, 2005).

2.3.1.7 Phosphorescence or Afterglow

A scintillating material produces delayed light as well as the scintillation light. Delayed light occurs after transitions made by electrons trapped in long-lasting energy states. Obviously, it is not a desirable property for a scintillation material. Because the scintillation does not extend the decaying part of the pulse, but if the temperature rises, it can cause an important combustion. The phenomenon is called thermal luminescence, as delayed light production, an important peak, requires the provision of thermal energy to the material. Some materials are extremely good at producing such a light by scintillating it with minimal fuss. Thermo-luminescence phenomenon is used in thermo-luminescence detectors (TLDs), which are also called memory devices (Aizawa et al., 2003; Sontakke, Ferrier, & Viana, 2017; D.-D. Zhang et al., 2018; Zhen et al., 2017).

2.3.1.8 Temperature Dependence

All other parameters affecting the scintillation material depend on the temperature of the material. For this reason, the numerical values reported in the literature always

correspond to working at a certain temperature or temperature range (Nguyen, Rougieux, Mitchell, & Macdonald, 2014).

2.3.1.9 Radiation Damage

Due to the high instantaneous and integrated radiation doses, scintillators used in hostile radiation environments tend to be damaged. Monitoring of the decay of the detector response over time is a standard practice in such laboratories. Nevertheless, not all materials act in the same manner when exposed to the radiation damage. Newly developed scintillators have shown good resistance to radiation damage, and, such rigid materials against radiation are preferred over conventional materials in applications involving high radiation moieties (Baccaro et al., 2018; Martin, Koch, & Nikl, 2017).

2.3.1.10 Scintillation Efficiency

Scintillation efficiency can be used to characterize the yield of the scintillation photons. Generally, it is described as a ratio of the total energy of scintillation photons and the total energy deposited by the incident radiation, that is

$$\eta = Es / Ei,$$

where Es and Ei indicate the total energy of scintillation photons and energy deposited by incident radiation, respectively (Gektin, Belsky, & Vasil'ev, 2014; Lecoq, Gektin, & Korzhik, 2016).

2.4 Scintillator Types

Scintillation is one of the oldest types of radiation detectors because it can be measured with photographic film. In this way, images can be collected or density measurements can be performed. The measurements were also made relying on the visual observation of the brightness of the frequency of the flashes in the scintillator.

Today, light output, proportional meters, semiconductor detectors and so on can be utilized for this purpose. The voltage is converted into voltage pulses in the same way. The whole point of the scintillation detectors is that we want to produce a large light output in the visible range. There are two commonly used types of scintillators, inorganic crystals, and organic scintillators. The scintillation mechanism is different for these two types (Lecoq et al., 2016).

2.4.1 Organic Scintillator

Organic scintillators are widely used in radiation detectors. These scintillating materials can be in solid, liquid and gaseous form. One of the greatest advantages of organic scintillators is that almost any geometry can be produced and therefore can be customized to specific applications (Brooks, 1979).

2.4.2 Inorganic Scintillator

Most of the inorganic scintillators have crystal structures. The inorganic scintillator materials have higher densities, higher atomic number and higher light output than that of the organic scintillators. These atomizers, which have high atomic number and intensity, provide a high stopping power for incident radiation and is preferred in applications where desired.

2.4.2.1 Scintillation Mechanism

The excitation mechanisms and properties of luminescent centers having a scintillator are more affected in the case of a crystal having a regular structure and surrounding medium, especially if it is a solid structure. The connection between the lattice and the light center is important, as the energy can be transmitted in both directions. In particular, the location of the energy levels of the stimulation centers relative to the valence and conduction bands formed by the orbitals of the lattice atoms strongly influences the localization and delocalization conditions of excitations.

2.4.2.1.1 Exciton Luminescence. When an inorganic scintillator crystal exposed to the ionizing radiation, electron-hole pairs from within the lattice. In case of crystals exhibiting exciton luminescence the electron-hole pairs stay somewhat bound to each other forming an exciton. Depending on the energy going to the crystal, the pair can move freely or remain partially attached due to the Coulomb effects. If the energy is high, it is enough to jump into the conduction band of the electron, and then it is free. In such a case, the hole having an effective positive charge also starts to move. However, if the energy released is not so high, the electron is partially connected to the hole. This can be seen as a band jump just below the conduction band of the electron (Figure 2.7).

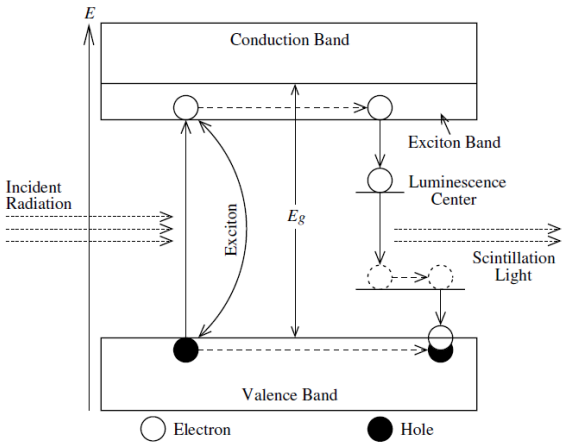

Figure 2.7 Schematic representation of exciton luminescence in an inorganic scintillator (Ahmed, 2007)

If the bond between the electron and the hole is not strong, a small amount of energy can be transferred to the electrons which can raise the electron to the conduction band. In this connected state, the electron and the hole are said to form a system called the exciton. The exciton can be trapped with a foreign matter or a defective site. If this field is a center of light, it can cause the emission of scintillation photons when the electron falls to the bottom. This process, commonly known as self-shutting of excitons, is graphically shown in (Figure 2.7). The trapping of excitons can also be accomplished by another process called charge transfer; in this case, the luminescence is called charge transfer luminescence (Pedrini, 2005; Ahmed, 2007; Gektin et al., 2014; Yoshida & Horiuchi, 2015; Hine, 2016; Lecoq et al., 2016).

2.4.2.1.2 Dopant Luminescence. Sometimes an impurity may be charged to enhance the scintillation characteristics of the materials. If an electron is trapped at the level of an additive and falls to a lower light level, the scintillation light is emitted. This process is shown in Figure 2.8.

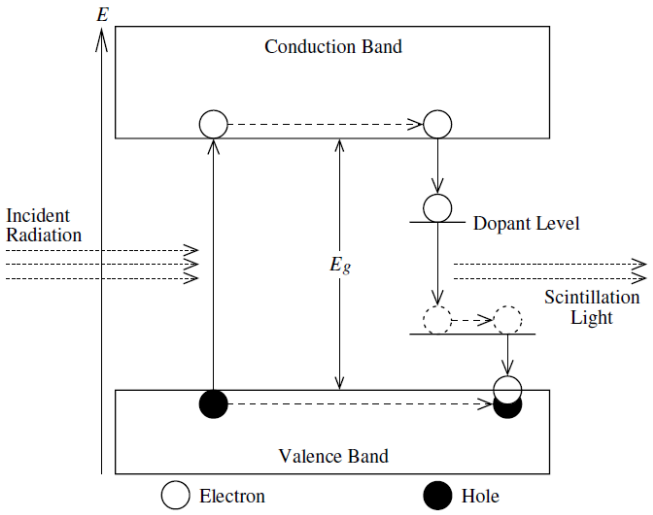

Figure 2.8 Principle of dopant luminescence in an inorganic scintillator (Ahmed, 2007)

2.4.2.1.3 Core Valence Band Luminescence. If the incident radiation provides enough energy while penetration into the lattice, it can raise the electrons from the deep core valence band to the higher energy conduction band. An electron arriving conduction band leaves a vacancy or hole behind. In order to hold the system in the stable state, one of the valence band electrons occupies this vacancy immediately which results in the emission of the scintillation light. The process is called as core valence band luminescence (Borgatti et al., 2018; Magnuson, Schmidt, Hultman, & Högberg, 2017; Meyer et al., 2014).

2.4.2.2 Some Common Inorganic Scintillators

The basic properties determining the inorganic scintillators can be listed as the emission maximum (λ_{max}), the light yield (dN / dE), the density (ρ) and the decay time (τ). Especially the two most important factors are the light emission and the emission wavelength. The choice of λ_{max} is mainly guided by the efficiency of the photon-counting detector, which depends on the wavelength. For example, in photomultiplier

tubes, the photocathode activity depends on the wavelength of the photons that form. This implies that a good match between the wavelength of the phototactic photons and the photocathode efficiency is required to achieve a high overall efficiency and a good signal-to-noise ratio. In practice, however, the choice is usually a compromise because a suitable scintillator for some other properties may not have the maximum efficiency of the photocathode λ_{max}. Especially when the detector is used in a low radiation environment, the light yield is definitely another factor.

Phosphorus groups in literature; simple oxides such as sulfates, ZnS type sulfides, CaS type sulfides, binary sulfides, various sulfides and oxysulfates, silicates, halosilicates, phosphates, halophosphates, borates, aluminates and talc, molybdates and tungstates, various oxides, halides, and oxyhalides. Gadolinium oxysulfate belongs to the orthorhombic system with a space group a = 12.996 Â, b = 8.117 Â, c = 4.184 Â. The sequential stacking of a sulfate layer (SO_4^{2-}) and a $Gd_2O_2^{2+}$ layer along the α-axis can explain the crystal structure. The Gd_2O_2S phase conversion from $Gd_2O_2SO_4$ can be calculated as removal of oxide ions surrounding sulfur due to reduction. Thus, $Gd_2O_2SO_4$ is generally used as a predecessor to Gd_2O_2S synthesis. In addition, $RE_2O_2SO_4$ doped rare earth ions are also used for high performance phosphorus when x-an ray or ultraviolet light is emitted (Lecoq, Gektin, & Korzhik, 2017; McGregor, 2017; Yanagida, 2018).

2.5 Luminescence of Phosphors

Luminescence is the emission of light from any substance and occurs from electronically excited states. Luminescence is formally divided into two categories fluorescence and phosphorescence depending on the nature of the excited state. In excited singlet states, the electron in the excited orbital is paired and is in an opposite spin with respect to the second electron in the ground-state orbital. Consequently, return to the ground state is spin-allowed and occurs rapidly by the emission of a photon. The lifetime (τ) of a fluorophore is the average time between its excitation and return to the ground state.

Phosphorescence is the emission of light from triplet excited states, where the excited electron has the same rotational orientation as the ground state electron. Passage to the ground state is prohibited and emission rates are slow with respect to the fluorescence, so the phosphorescence lifetimes are usually from milliseconds to "as long as possible".

Fluorescence is an extensively used methodology extending from biotechnology, flow cytometry, medical diagnostics, DNA sequencing, forensic science, to genetic analysis and imaging. Scientists from many disciplines use fluorescence technology. (Bai, Tsang, & Hao, 2015; Xia & Meijerink, 2017; Xie, Hirosaki, Li, & Takeda, 2010).

2.5.1 Quantum Mechanical Description

Following the path of the optical transition illustrated in Figure 2.9, presume that Hooke's law expresses the bonding force between the luminescent ion and a nearest-neighbor ion. The deviation from the equilibrium position of the ions is taken as the configurational coordinate denoted as Q. The following relations give the total energy of the ground state, Ug, and that of the excited state, Ue.

$$U_g = K_g \frac{Q^2}{2} \tag{2.7}$$

$$U_e = K_e \frac{(Q-Q_0)^2}{2} + U_0 \tag{2.8}$$

where K_g and K_e are the force constants of the chemical bond, Q_0 is the interatomic distance at the equilibrium of the ground state, and U_0 is the total energy at $Q = Q_0$.

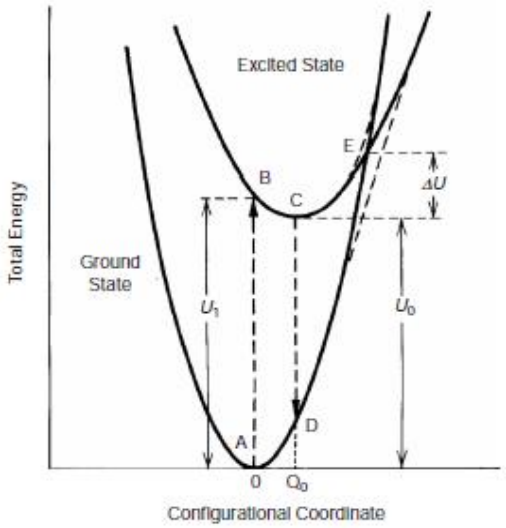

Figure 2.9 A schematic illustration of a configurational coordinate model. The two curves are modified by repulsion near the intersection. The vertical broken lines A ↔ B

In Figure 2.9 vertical broken arrows indicate optical absorption and emission processes. According to the Franck–Condon principle, an electronic transition occurs without changes in the positions of the nuclei in the molecular entity and its microenvironment. This principle is quite reasonable since an atomic nucleus is 10^3 to 10^5 times heavier than an electron. At 0 K, the optical absorption proceeds from the equilibrium position of the ground state and the probability for an excited electron to lose energy by generating lattice vibration occurs within 10^{12} to 10^{13} s^{-1}. Whereas the probability for light emission occurs around 10^9 s^{-1}. Optical absorption from A to B and relaxation from B to the equilibrium position C occurs before it emits luminescence. This is followed by the emission process C → D and the relaxation process D → A.

The energy state of a localized center taking place in luminescence can be defined by a wave function **Ψ**. It is a function of both electronic "**r**" and nuclear "**R**" coordinates, and can be considered in the electronic part and the nuclear part by the adiabatic approximation:

$$\boldsymbol{\Psi}_{nk}(\boldsymbol{r},\boldsymbol{R}) = \boldsymbol{\Psi}_{k}(\boldsymbol{r},\boldsymbol{R})_{X_{nk}}(\boldsymbol{R}) \tag{2.9}$$

herein n and k are the quantum numbers of the electron and the nucleus, respectively. The time-independent Schrödinger equation for the nuclear wave function is as follows,

$$\{-\sum_a \left(\hbar^2/_{2M_a}\right) \Delta R_a + U_k(R)\} X_{nk}(R) = E_{nk} X_{nk}(R) \tag{2.10}$$

where α indicates the nuclear number, M_α is the mass of the α^{th} nucleus, ΔR_α is the Laplacian of R_α, and E_{nk} is the total energy of the localized center. The energy component of the equation $U_k(R)$; consists of two parts: the energy of the electrostatic interaction between the nuclei the localized center and the energy of the electrons. Considering Eq., one finds that $U_k(R)$ plays the role of the potential energy of the nuclear wave function χ_{nk}. (Recall that the electron energy also depends on R.) Thus, $U_k(R)$ is an adiabatic potential and it forms the configurational coordinate curve when one takes the coordinate Q as R. When $U_k(R)$ is expanded in a Taylor series up to second order around the equilibrium position of the ground state, the potentials are expressed by Eq. 2.7. For a harmonic oscillation, the second term is the first nonvanishing term, while the first term is non-zero only when the equilibrium position is displaced from the original position. In the latter case, the first term is related to the John-Teller effect. Sometimes, the fourth term in the present, signaling anharmonic effects. In the following, consider for simplicity only a single coordinate or a two-dimensional model.

Consider a harmonic oscillator in a potential shown by Eq. 2.7. This oscillator gives discrete energy levels inside the configurational coordinate curves, as illustrated in Figure 2.10.

$$E_m = (m + 1/2)\hbar\omega \tag{2.11}$$

where ω is the proper angular frequency of the harmonic oscillator.

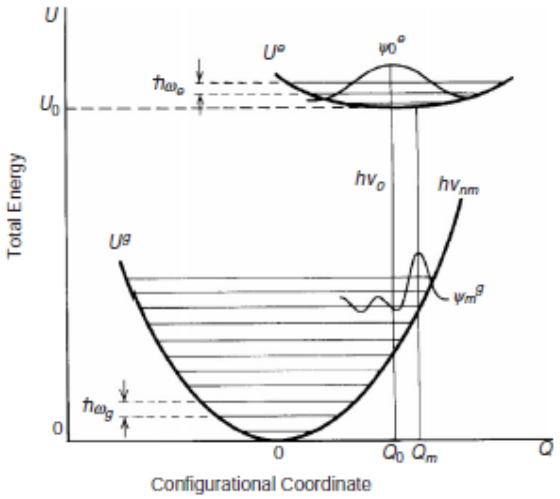

Figure 2.10 Discrete energy levels, each having the energy of ħω and the wave functions Ψ_0^e and Ψ_m^g of harmonic oscillators indicating the two states where v_0 means the frequency at the emission peak

The electric dipole transition probability, W_{nm}, between the two vibrational states n and m is given by:

$$W_{nm} = \left|\iint \Psi_e X_{en}^* er \Psi_g X_{gm} dr dQ\right|^2 = \left|\int X_{en}^* X_{gm} M_{eg}(Q) dQ\right|^2 \qquad (2.12)$$

here,

$$M_{eg}(Q) \equiv \int \Psi_e^*(r,Q) er \Psi_g(r,Q) dr \qquad (2.13)$$

When the transition is allowed, M_{eg} can be placed outside the integral, because it depends weakly on Q. This is called the Condon approximation and it makes Eq. 2.12 easier to understand as:

$$W_{nm} = \left|M_{eg}(Q)\right|^2 . \left|\int X_{en}^* X_{gm} dQ\right|^2 \qquad (2.14)$$

The wave function of a harmonic oscillator has the shape illustrated in Figure 2.10. For m (or n) = 0, it has a Gaussian shape; while for m (or n) 0, it has a maximum amplitude at both ends and oscillates m times with a smaller amplitude between the maxima. Therefore, the integral takes the largest value along a vertical direction on the

configurational coordinate model. This explains the Franck-Condon principle in terms of the shapes of wave functions. One can also state that this is the condition for which holds. The square of the overlap integral is an important quantity that determines the strength of the optical transition and is often called the Franck-Condon factor (E. M. J. Weber, Dotsenko, Glebov, & Tsekhomsky, 2003).

2.5.2 Jablonski Diagram

The Jablonski diagram shows the processes that occur during absorption and emission of light. A typical Jablonski diagram is shown in Figure 2.11. Ground, first and second electronic states are denoted by S_0, S_1, and S_2 respectively. T1 denotes the first excited triplet state. A series of vibrational levels takes place between the energy levels. Quenching, energy transfer and solvent interactions are discussed considering the Jablonski diagram in the following sections. Transitions between states are depicted as vertical lines to show the instant nature of light absorption (Birks, 2013).

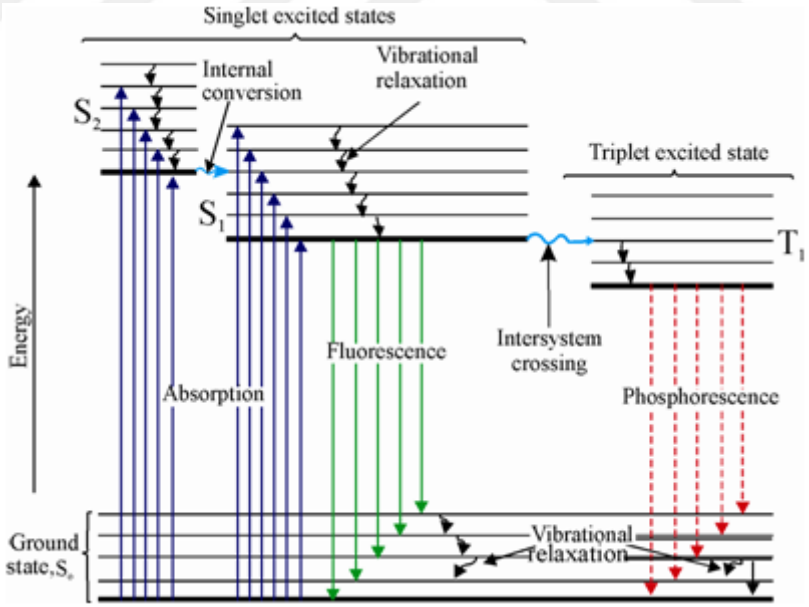

Figure 2.11 Jablonski diagram (Quora, n.d.)

The horizontal bold lines at the bottom of each electronic energy level in the diagram show the lowest vibrational energy level, and the thin lines indicate the other higher vibrational energy levels of each electronic state. Electronic energy levels can

be named as the principal basic (S0), stimulated (S1, S2…) singlets and stimulated triplets (T1). As usual, the energy of the first excited triplet state is lower than the energy of its corresponding singular state.

As can be seen in Figure 2.11, the absorption transitions can occur towards various vibrational levels of the first and second singlet excited electronic states (S1) and (S2), from the single electronic state S0. The probability of direct excitation to triple state is very low. For this reason, it is expressed as a forbidden transition. Molecules, which are stimulated by electronic states S1 and S2, lose their excessive vibration energy rapidly and are become relaxed to the ground vibrational level of this electronic situation. This non-radiative process is called vibrational relaxation. Photon absorption occurs about 10^{-14} to 10^{-15} s. Fluorescent emission is at a significantly lower rate with respect to the absorption which occurs between 10^{-5} to 10^{-10} s. And, the average speed of a triplet-to-singlet transition is less than that of a corresponding singlet-to-singlet transition. Therefore, the emission of phosphorescence takes place within 10^{-4} to 10 s or more (Skoog, Holler, & Crouch, 2017).

During the electronic stimulation process, an electron can be excited to any of the various vibrational levels. Following collisions between molecules of the excited species and the molecules of the solvent may lead to rapid energy transfer with a slight increase in the temperature of the solvent. Vibrational relaxation is much shorter than the average life of an electronically excited state. One consequence of the vibrational relaxation is that the fluorescence band for a given electronic transition appears at lower frequencies or at the longer wavelengths with respect to the absorption band the difference between the absorption and emission maximum is known as Stoke's shift (Joens, 2015; Skoog et al., 2017).

During the "internal conversion" process a molecule undergoes a low-energy electronic state without radiation. These processes are often very efficient. Internal conversion is a transition between two states with the same multiplicity (singlet-singlet or triplet-triplet). It is particularly effective when the two electronic energy levels are sufficiently close to each other in terms of the vibrational energy levels. This is shown

in Figure 2.11 for two exciting singlet status S2 and S1. The internal conversion can also occur between the S1 state and the ground electronic state S0. Another non-radiative process, which allows the molecule to return to the ground state as a result of collisions with the solvent molecules, is called “external conversion”.

“Intersystem crossing” is a process from S1 to T1, where there is a transition between the electronic states of the different multiplicity. The possibility of transition increases when the vibrational levels of the two states are in case of overlap. In such cases, the spin and orbit interaction becomes more appropriate the spin conversion occurs. Once the molecule has transitioned to a triplet state, further deactivation occurs by internal or external fluorescence or phosphorescence. The triplet molecule has a long life. Because external and internal conversions compete very effectively with phosphorescence, the molecule must be observed at a lower temperature and in high viscosity environments to maintain the triplet state (Valeur & Berberan-Santos, 2012).

2.5.3 Luminescence of Rare Earth Ions

2.5.3.1 Electronic Configuration

The rare earth elements consist of 17 elements extending from La (with an atomic number of 57) to Lu (atomic number of 71), and Sc (atomic number 21) and Y (atomic number 39). The electronic configurations of the trivalent rare earth ions are shown in Figure 2.12. Electron number of Sc^{3+} matches to Ar, Y^{3+} to Kr and La^{3+} to Xe. Lanthanides from Ce^{3+} to Lu^{3+} have electron attachments from one to fourteen over the inner shell configuration of Xe. Sc^{3+}, Y^{3+}, La^{3+}, and Lu^{3+} ions have no electronic energy level that can induce excitation and luminescence in or near the visible region due to the lack of 4f electrons. On the contrary, ions from Ce^{3+} to Yb^{3+} which have partially filled 4f orbitals have energy levels of each ion and exhibit luminescence around the visible region. Most of these ions having luminescent properties, mostly Y^{3+}, Gd^{3+}, $La^{3+,}$ and Lu^{3+}, are substituted in crystal structures to form phosphors (Wang et al., 2015).

Atomic number	Ions	Corresponding element	4*f* electrons							S Σs	L Σl	J Σ(L+S)
21	Sc^{3+}	Ar								0	0	0
39	Y^{3+}	Kr								0	0	0
57	La^{3+}									0	0	0
58	Ce^{3+}	Xe	↑							1/2	3	5/2
59	Pr^{3+}	Xe	↑	↑						1	5	4
60	Nd^{3+}	Xe	↑	↑	↑					3/2	6	9/2
61	Pm^{3+}	Xe	↑	↑	↑	↑				2	6	4
62	Sm^{3+}	Xe	↑	↑	↑	↑	↑			5/2	5	5/2
63	Eu^{3+}	Xe	↑	↑	↑	↑	↑	↑		3	3	0
64	Gd^{3+}	Xe	↑	↑	↑	↑	↑	↑	↑	7/2	0	7/2
65	Tb^{3+}	Xe	↑↓	↑	↑	↑	↑	↑	↑	3	3	6
66	Dy^{3+}	Xe	↑↓	↑↓	↑	↑	↑	↑	↑	5/2	5	15/2
67	Ho^{3+}	Xe	↑↓	↑↓	↑↓	↑	↑	↑	↑	2	6	8
68	Er^{3+}	Xe	↑↓	↑↓	↑↓	↑↓	↑	↑	↑	3/2	6	15/2
69	Tm^{3+}	Xe	↑↓	↑↓	↑↓	↑↓	↑↓	↑	↑	1	5	6
70	Yb^{3+}	Xe	↑↓	↑↓	↑↓	↑↓	↑↓	↑↓	↑	1/2	3	7/2
71	Lu^{3+}	Xe	↑↓	↑↓	↑↓	↑↓	↑↓	↑↓	↑↓	0	0	0

Figure 2.12 Ground State Electronic Configurations of Trivalent Rare-Earth Ions (E. M. J. Weber et al., 2003)

From the view of spectroscopists, the term symbol is a description of the total angular momentum quantum numbers for a multi-electron atom. Energy levels of an atom can also be described by term symbols. The subjective energy level also depends on the total angular momentum including spin. The ground state term symbol is predicted by Hund's rules.

The azimuthal quantum number describes the shape of the orbital. The azimuthal quantum number (l) of 4f orbitals is 3 and therefore 7 different f orbitals are subjective. Spin can be excepted as the rotation of a particle around an axis. Spin quantum numbers may take half-integer values. The spin of a charged particle is associated with a magnetic dipole moment. This can only be if the internal charge of the particle was distributed differently from its mass. The spin quantum number, S, is S = n/2, where n can be any positive integer. The spin-orbit interaction (or coupling) is the interaction between L and S is known as LS coupling. Atomic states are then well described by term symbols of the form;

$$^{2S+1}L_J$$

herein, S is the total spin quantum number, and, 2S + 1 is the spin multiplicity, which represents the number of possible states of J for given values of L and S. In the ground state, the electrons are located to provide a maximum combined spin angular momentum (S). The spin angular momentum S is also combined with the trajectory angular momentum L to obtain the total angular momentum J which is as follows;

If the number of 4f electrons is less than 7, the total angular momentum, J = L – S

If the number of 4f electrons is greater than 7, J = L + S

If J is the total angular momentum quantum number and L is the total orbital quantum number, from the view of spectroscopists the first 17 symbols of L can be listed as;

L = 0 1 2 3 4 5 6 7 8 9 10 11 12 13 14 15 16

S P D F G H I K L M N O Q R T U V

(E. M. J. Weber et al., 2003).

2.5.3.2 Electronic Processes Leading to Luminescence in Lanthanides

The lanthanide series consists of the elements with atomic numbers of 58 to 71, which fill their 4f sublevels respectively. The electronic energy levels of lanthanide ions make them different from each other. These electronic levels are not greatly influenced by the environmental factors because the electrons of 4f are protected from the external electric fields by the outer 5s and 5p orbitals. However, in case of transition metal ions, this is totally different. They are open for environmental effects or crystalline electric field of the 3d electrons in the outer orbits. Dieke et al. investigated the typical 4f electrons and related energy levels of trivalent lanthanide ions. Figure 2.13 shows the Dieke diagram. The diagram shows energy levels of the trivalent rare earth ions. The levels were determined experimentally by considering the optical spectra of the individual rare earth ions in $LaCl_3$ crystals (Lewis & Kasha, 1944; Valeur & Brochon, 2012). The number of corresponding 4f electrons of the rare earth ions are shown at the bottom of the table.

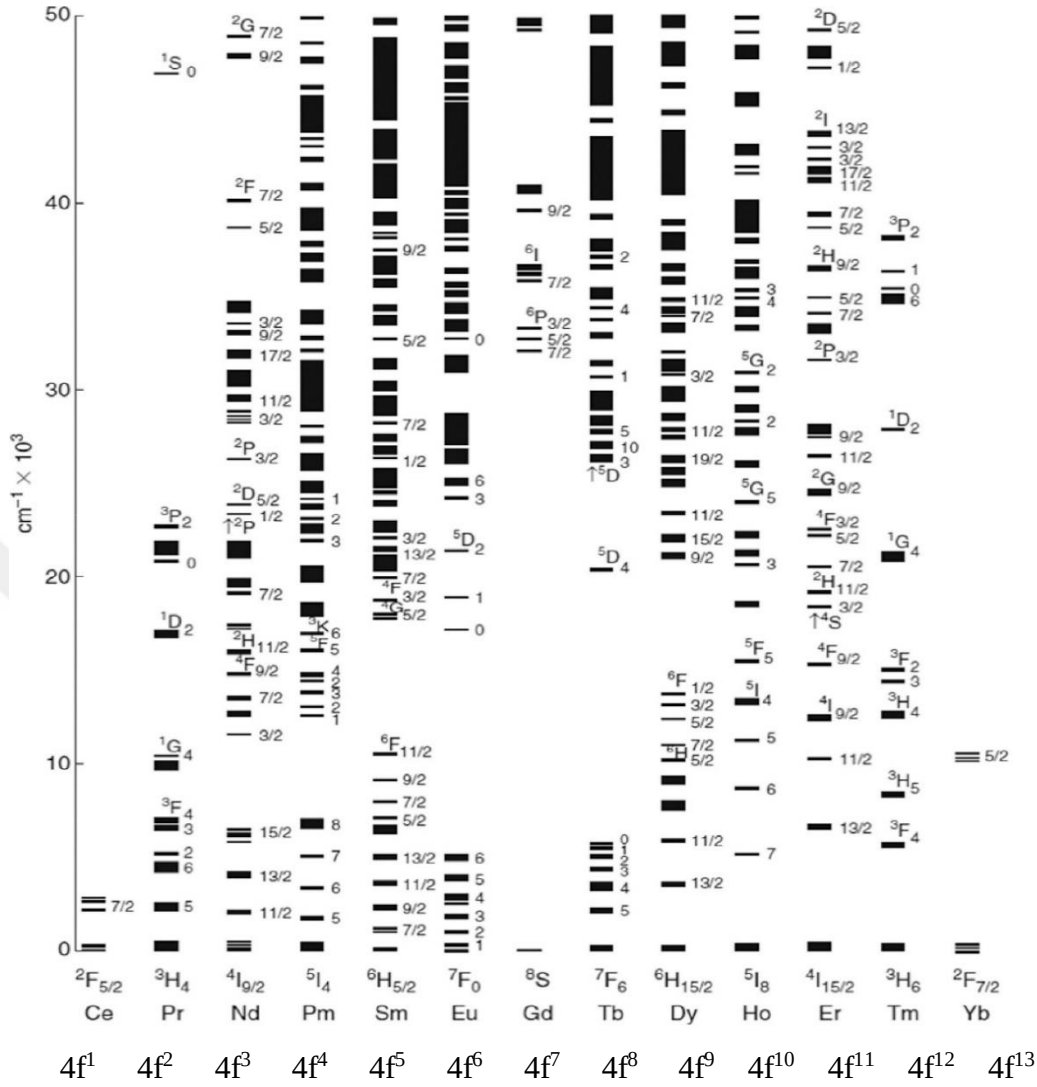

Figure 2.13 Energy levels of trivalent lanthanide ions including term symbols (E. M. J. Weber et al., 2003)

2.6 Imaging Devices

Creating an image of an object requires exposing it to a radiation field such as x-rays or light photons, and then detecting the broken and transmitted particles reflected in a two-dimensional position sensitive detector. Common examples of imaging devices are medical x-ray systems and digital photographic machines. In general, imaging devices can be divided into two categories: conventional and electronic. The film-based x-ray system is a conventional device; The digital camera is an electronic

imaging system. In the following sections, we will look at some important devices of each of these categories (Kang, 1997).

2.6.1 Conventional Imaging

Photographic films are so sensitive to x-rays through conventional imaging that they absorb only 1% of a typical x-ray film radiation. Typical photographic films cannot find x-rays below 0.1 photons per mm^2. Photographic film emulsions react in a logarithmic level to the event x-ray flux. As a result, the image contrast needs to be interpreted very carefully. Photographic films must be chemically developed to monitor the video. With modern technology, this process does not require more time and effort but is still incompatible with real-time data acquisition and processing offered by electronic imaging systems. Filming is difficult even if it is not impossible to record electronically on a computer memory device for archiving and electronic transfers (Schulze, Heiland, Thurmann, & Adam, 2004; White, Amos, & Fordham, 1987).

2.6.2 Electronic Imaging

Electronic imaging is one of the fastest growing areas, mostly due to its applicability in consumer electronics, cost-effectiveness, and high resolution. Digital cameras have literally changed traditional film cameras. These cameras use charged coupled devices (CCDs) to record photons from the object. A processor that restructures the image of the object uses the resulting signals. CCDs also have medical diagnostic applications. In other areas, such as astronomy and particle physics, electronic imaging devices have made tremendous progress. The rapid development of such devices has added a fair amount of complexity not only in hardware but also in software (Kang, 1997; Schreiber, 2012; Weeks, 1996).

2.6.3 Charged Coupled Devices

Most of the disadvantages of photographic films have been met through the development of different electronic imaging devices. Such a sensing system is called Charged Coupled Device or CCD. This semiconductor based multi-channel imaging system is used for two-dimensional imaging and is now standard in many applications. The basic operating principle of a CCD is the same as other semiconductor detectors, which convert incident radiation into electron-hole pairs and measure the resulting signal. There are different CCD designs developed over the years depending on specific applications. However, we can confidently divide these devices into two main categories: direct and indirect imaging systems (Amelio, 1974; Janesick, 2001; Theuwissen, 2006).

2.6.4 Direct Conversion

A direct imaging CCD is used to convert incident radiation directly into binary pairs of electrons interacting with the semiconductor material. Free electrons and holes move towards the opposite electrodes under the influence of the externally applied electric field and create a load on the reading electrodes. The resulting signal pulse is processed by electronics connected to the reading electrodes (Engel & Herrmann, 2015). This direct detection method works well for x-rays, which have the potential for high interaction in the depletion zone. However, the system suffers from some less desirable disadvantages for x-ray imaging. For example, the production of electron-hole pairs in the depletion zone depends on the energy of the event x-ray photons. At energies above 20 keV, the probability of interaction is so low that the direct detection method does not produce a reasonable signal-to-noise ratio.

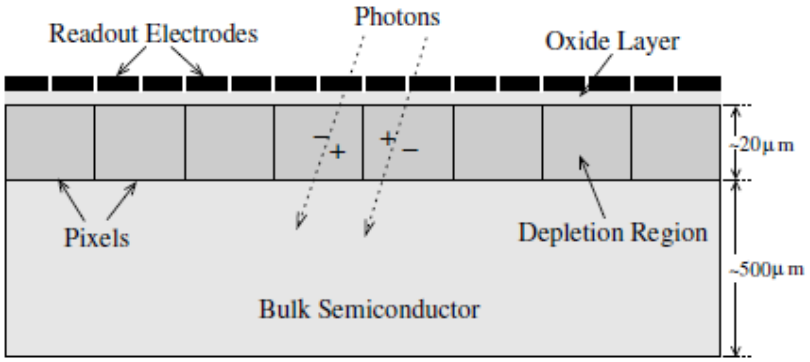

Figure 2.14 Schematic of a typical CCD working in direct detection mode with front illumination (Ahmed, 2007)

In addition, like all semiconductor detectors, CCDs are also damaged by instantaneous and integrated radiation doses. Direct detection exposes the CCD to radiation and therefore reduces its performance over time due to damage caused by radiation. Direct detection CCDs have a small active area and are not suitable for most imaging needs (Ergler, Freund, Kreisler, Schröter, & Wirth, 2016; Kasap & Rowlands, 2002).

2.6.5 Indirect Conversion

The disadvantages of direct detection can be overcome by converting x-ray photons to visible light photons with the highest sensitivity of standard CCD sensors. Of course, the trick is to ensure the linearity of the transformation process and make it as efficient as possible. Different phosphor and scintillator types are defined as effective photon transducers. Phosphorus is added to the granule while scintillators are in the form of polycrystalline dust. In general, the phosphor is used in CCD cameras. The efficiency of the conversion process can be optimized by changing the chemical composition of the phosphors and the grain size. Occasionally, additional mirror coating is also provided to increase the x-ray interaction in the material (Yaffe & Rowlands, 1997).

Figure 2.15 shows the outline of the main components of a typical imaging device based on CCD sensors. Phosphorus absorbs x-rays which immediately attracts the

light. These light photons are directed to the photocathode of the image intensifier through an optical coupling, such as a fiber optic. The role of this intensifier is to raise the light from the first phosphor. The photo-cathode transforms light photons into electrons by multiplying them through multiple stages of a photomultiplier tube. These electrons are then converted to light photons by another phosphor or scintillator layer. These light photons are passed through a fiber optic guide before entering the CCD discharge area to produce electron-hole pairs. Such a multi-step process extends the life of the detector by preventing x-rays from reaching sensitive CCD sensors. In addition, such a device can be used for a wide range of x-ray energy compared to direct imaging systems, which are substantially insensitive even at moderate energy (Hoheisel et al., 1998; Spahn et al., 2000).

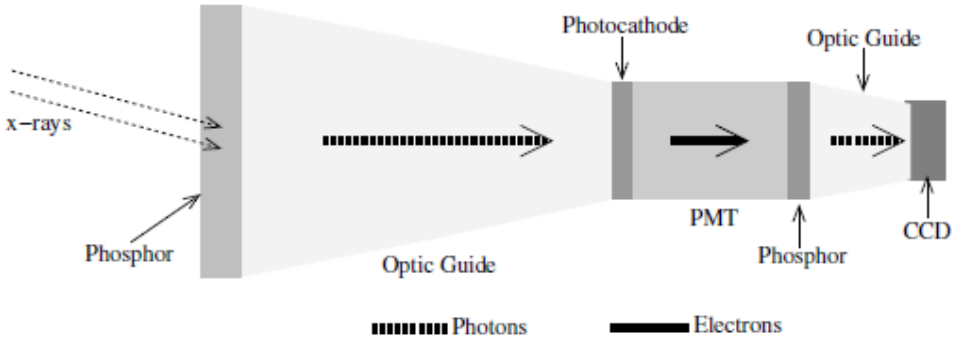

Figure 2.15 Sketch of an indirect CCD for x-ray imaging (Ahmed, 2007)

CHAPTER THREE
EXPERIMENTAL PROCEDURE

In this thesis, pure and Dy^{3+}, Ce^{3+}, Eu^{3+}, Ho^{3+}, $Pr^{3+,}$ and Tb^{3+} doped $Gd_2O_2SO_4$ phosphorescence nanoparticles were synthesized by sol-gel method. Amount of dopants were optimized according to the concentration of the additive element and then material production and characterization were realized. The characterization process was carried out separately in three different production stages, namely solution, gel, and final product. In these processes, the pH and turbidity values of the solutions were determined. Nearly neutral or slightly acidic (pH: 6.1) and fully dissolved solutions were obtained. FTIR analysis was performed to determine organic bonds to the sol-gel material, and DTA-TG thermal analyzes were performed to determine exothermic-endothermic reactions. The heat treatment temperature required to find the correct phase was determined at this stage. The final product was then obtained and characterization was completed using FTIR, XRD, XPS, SEM and PL devices respectively.

3.1 Preparation of Nanoparticles by Sol-Gel Technology

3.1.1 Sol-Gel Techniques

The sol-gel method is a chemical technique that uses metal alkoxides for the synthesis and production of glasses or ceramics by a series of chemical processes including hydrolysis, gelation, drying and heat treatment (Hench & West, 1990).

3.1.2 Material and Methodology

All solvents and chemicals used in the study were of high purity and purchased from Sigma Aldrich. Gadolinium(III) acetate hydrate ($Gd(CH_3CO_2)_3 \cdot xH_2O$), ammonium sulfate, urea, dysprosium (III) nitrate hydrate ($Dy(NO_3)_3. xH_2O$, >99 %), europium (III) nitrate pentahydrate ($Eu(NO_3)_3.5H_2O$, >99 %), terbium (III) nitrate pentahydrate ($Tb(NO_3)_3.5H_2O$, >99 %), holmium (III) acetate hydrate,

($(CH_3CO_2)_3Ho \cdot xH_2O$,>99%) and cerium (III) acetylacetonate hydrate ($Ce(C_5H_7O_2)_3. xH_2O$, >99 %) were utilized as initial precursors. Distilled water was utilized to dissolve precursors as a solvent. In general, the sol-gel process consists of three steps, hydrolysis, and condensation of alkoxide or nitrate precursors, followed by gelation, drying, and heat treatment. Sol-gel precursors react chemically with solvents and other agents present in the solution (Pierre, 2013).

The starting materials and properties used in the production of nanomaterials by sol-gel are described in detail. Initial solids for sol-gel preparations include metal alkoxides in solid or liquid form (Table 3.1). $Gd_2O_2SO_4$ and $Gd_2O_2SO_4$: RE sols were synthesized via the sol-gel process utilizing urea, ammonium sulfate and rare earth chemical components as initial precursors. We obtained homogenous solutions using distilled water as the solvent. Solutions were prepared in a glove box device (Figure 3.1) under a nitrogen atmosphere to avoid any oxidation of precursors owing to the presenting highly sensitive to the environment. To create a 0.1 M solution for pure $Gd_2O_2SO_4$, the precursor of 0.001 moles of $Gd(CH_3CO_2)_3$ was dissolved in 100 ml of purified water. A 0.1 M urea solution was formed in another beaker. A 0.1 M ammonium sulfate solution was then formed in another beaker. Then, these three solutions were mixed together and allowed to evaporate at 90 ^{0}C until gelation occurs. For the preparation of rare earth elements activated $Gd_2O_2SO_4$ solutions, three different beakers were used. Optimization is done to determine the optimum additive concentration. Three different additive rate amounts were tested for the dysprosium element. 0.5 percent, 1 and 1.5 percent of $Gd_2O_2SO_4$: Dy^{3+} productions were made and characterized. Since the optical luminescence intensity is the highest at 1 percent contribution ratio, only 1 percent of the other additive elements are selected. 0.099 M $Gd(CH_3CO_2)_3 \cdot xH_2O$ solution and 0.001 M solution of each of the rare earth precursors were added to make the final solution. The experimental steps after the solution are formed are the same in all productions. Solutions were stirred vigorously for 30 minutes to assist disperse particles in a solvent on a magnetic stirrer. All solutions were then mixed to form the final transparent solution. The solutions were retained in an airtight beaker at room temperature for 30 min. for complete hydrolysis to obtain homogeneous and transparent clear solutions.

Table 3.1 The chemicals used for the production of the nanoparticles scintillators

Chemicals	**Formula**	**Purity**
Urea	CH_4N_2O	>99%
Ammonium sulfate	$(NH_4)_2SO_4$	>99%
Gadolinium(III) acetate hydrate	$Gd(CH_3CO_2)_3 \cdot xH_2O$	>99%
Dysprosium (III) nitrate hydrate	$Dy(NO_3)_3 \cdot xH_2O$	>99%
Europium (III) nitrate pentahydrate	$Eu(NO_3)_3.5H_2O$	>99%
Terbium (III) nitrate pentahydrate	$Tb(NO_3)_3.5H_2O$	>99%
Holmium(III) acetate hydrate	$(CH_3CO_2)_3Ho \cdot xH_2O$	>99%
Cerium (III) acetylacetonate hydrate	$Ce(C_5H_7O_2)_3.xH_2O$	>99%
Praseodymium trinitrate hexahydrate	$Pr(NO_3)_3 \cdot 6H_2O$	>99%
Distilled water	H_2O	>99%

An alkoxide is a metalorganic compound in which a hydrogen atom of an alcohol hydroxyl group (OH) is replaced by a metal atom. Herein we used $Gd(CH_3CO_2)_3 \cdot xH_2O$ instead of the metal alkoxide. Since the sol-gel process is a wet chemical process, a suitable solvent is required to convert to liquid when used. We used distilled water as the solvent. The 0.01M solution of doping or activator ions of Dy^{3+}, Ce^{3+}, Eu^{3+}, Ho^{3+}, Pr^{3+}, Tb^{3+} are introduced into the solution prior to the gelation stage. This liquid mixture is stirred for a long time. A water- acid mixture is added to induce hydrolysis (Sheldon, 2012). Potential mechanism of the reactions taking place in the reaction pot can be given as follows (J. Lian et al., 2014)

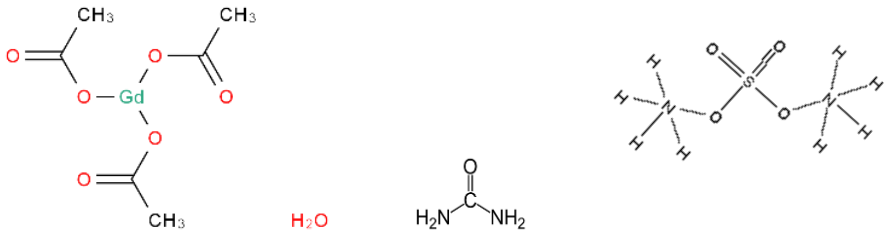

Figure 3.1 Chemical structure of the precursors; from left to right; gadolinium acetate hydrate, urea, and ammonium sulfate.

$$CO(NH_2)_2 + 4H_2O \leftrightarrow 2NH_4OH + H_2CO_3 \quad (3.1)$$

$$NH_4OH \leftrightarrow NH_4^+ + OH^- \quad (3.2)$$

$$H_2CO_3 \leftrightarrow 2H^+ + CO_3^{-2} \tag{3.3}$$

$$2Gd^{3+} + 3SO_4^{2-} \leftrightarrow Gd_2(SO_4)_3 \tag{3.4}$$

$$2Gd^3 + 2OH^- + CO_3^{2-} + SO_4^{2-} + nH_2O \leftrightarrow Gd_2(OH)_2(CO_3)(SO_4).nH_2O \tag{3.5}$$

$$Gd_2(OH)_2(CO_3)(SO_4).nH_2O \leftrightarrow Gd_2O_2SO_4 \tag{3.6}$$

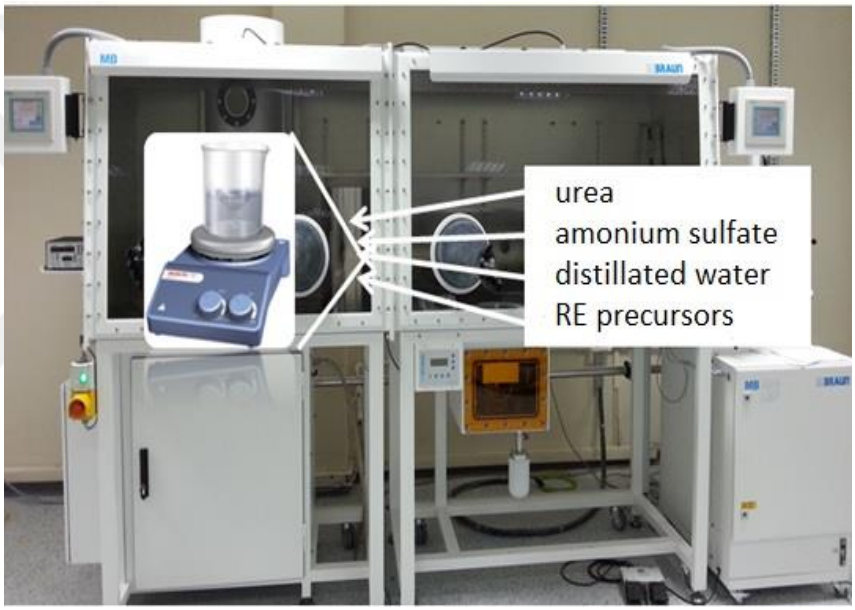

Figure 3.1 Glovebox system for preparation of solutions (Personal archive, 2018)

In a conventional sol-gel reaction the deprotonation of a dissolved metal (M) cation results in the subsequent hydrolysis. During this process, water molecules around M cause a loss of a proton. In this thesis, the metal used is the Gd^{3+} ions in form of acetate chelate. After the hydrolysis reactions, a condensation reaction takes place to form the polynuclear complex formed between the two metal atoms. Condensation observed in aqueous solutions results in either olation or oxidation reactions. In both cases, the available oxygen should sometimes be controlled as it accelerates the reaction. In order to control this situation, herein we studied in a nitrogen atmosphere.

As a result of the hydrolysis and condensation reactions, a three-dimensional network structure is formed and then a solid phase usually forms. As the heat of both reactions increases with temperature, the reaction rate increases accordingly. The pH affects both the hydrolysis and condensation reactions at the same time as the formation of the polymer like structures. Thus, various materials with different structures can be obtained. These structures may also include linear polymers, dense colloidal particles, or more or less weakly bonded cross-linked clusters of polymers (Pierre, 2013).

After each gelling process, drying at 250 °C was performed for 30 minutes. The dried materials were characterized by FTIR and then heat treated. This process was carried out for all of the materials.

The gel samples were treated by heat at 400, 600, 800, 900, 1000 and 1100 ºC for 2 hours under argon gas atmosphere. Temperature values were determined according to DTA-TG results. The purpose of the thermal treatment is to vaporize or disintegrate the organic additives and other impurities and to remove residual and chemically bound water. Steps of the heat treatment process are given in Figure 3.3.

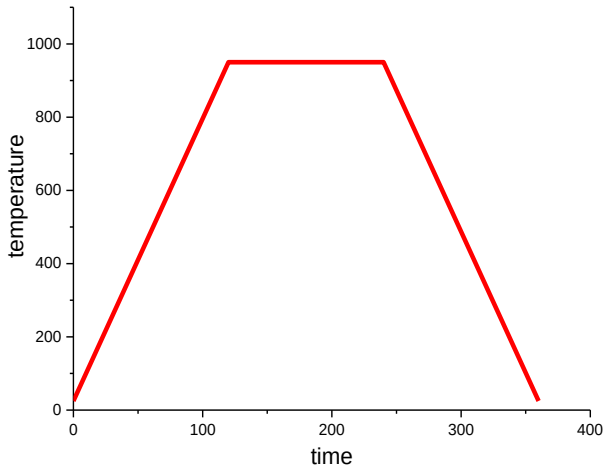

Figure 3.3 Steps of the heat treatment process of the $Gd_2O_2SO_4$: RE nanoparticles

The conversion of a sol or solution into a gel is called as gelation. In order to form a 3-dimensional solid network, links between the sol particles or solution molecules

should be formed. As result of hydrolysis and condensation, clusters grow to bound together to create gel (Brinker & Scherer, 2013).

The heat treatment is a thermal treatment that densification accompanies. Sol-gel ceramics just after drying and even after heat treatments at intermediate temperatures often have a very high specific surface area and an extremely small grain size. "Since states with a lower Gibbs free energy are more stable at a given temperature and pressure, the specific surface area should tend to decrease, an evaluation which can proceed according to two types of pore evaluation: (a) by changing the shape of pores but not their volume and (b) by eliminating the pores. Hence, the dense materials can be obtained after the heat treatment process" (Woodhead & Segal, 1984).

In this study, rare earth doped and undoped scintillator particles were successfully produced by the sol-gel method and heat treatment applied. Both the doped and undoped forms were tested between 400-1100 ^{o}C. However, after 1000 ^{o}C structure of the $Gd_2O_2SO_4$ changed to Gd_2O_3. Heat treatment temperature was determined as 900 degrees and applied. Therefore, in order to keep the structure in the $Gd_2O_2SO_4$ form, we did not exceed 1000 ^{o}C in further studies.

3.3 Characterization

3.3.1 Solution Characterization

In the sol-gel process, the pH and turbidity of the solution play an important role in determining the microstructure and properties of the final product. For this reason, initially prepared solutions were tested with pH meter and turbidity meter.

3.3.1.1 The pH Measurement

For pH measurements, a pH-sensitive electrode and a reference electrode are required. It can also be preferred as an extra apparatus in the temperature sensor (Rani, Suri, Shishodia, & Mehra, 2008; J. Zhang & Gao, 2004).

The pH of a solution affects the solubility of a compound, coating quality, the rate of a reaction and many chemical processes. In this study, WTW pH 3110 pH meter and a combined glass electrode were used to determine pH values.

3.3.1.2 Turbidity Measurement

Turbidity gives the optical properties of particles that are insoluble in a liquid. At the same time, it can be said that the extent of the blur of liquid. In this measurement, light passes through the sample and diffuses in all directions. The light emitted at 90^{o} to the light beam is then detected by a photodiode and converted into a signal that is linearized by the analyzer and shown as a nephelometric turbidity unit (ntu). If a suspended particle in the liquid is too large, the incoming light is very scattered and a higher ntu value is obtained (Ebeoglugil, 2011).

Turbidity properties of $Gd_2O_2SO_4$ and $Gd_2O_2SO_4$: RE solutions were detected to using standard solutions by VELP TB1 Model turbidimeter. The sample was placed in a vessel with a dimension of Ø25 mm and a height of 50 mm. Formazine is recognized throughout the world as a primary standard. The formation solution was used to calibrate the turbidity measurements. Measurement range was kept in the range of 0 and 1000 ntu.

3.3.2 Material Characterization

3.3.2.1 Differential Thermal Analysis-Thermogravimetry (DTA-TG)

Thermal methods often measure the dynamic relationship between certain properties of the material (mass and heat absorption or diffusion) that occur at varying temperatures. Therefore, differential thermal analysis (DTA) and thermogravimetry (TG) are important methods for determining the thermal properties of materials. In DTA the heat absorbed or emitted by a system is detected by measuring the temperature difference "ΔT" between the sample and an inert reference material

(generally alumina powder), as the temperature of both is raised at a constant rate. The TG analysis gives the result of changing the weight of the material with the increase in temperature. Many series of thermal analysis techniques can be combined with other non-thermal technique for valuable multiple-parameter information as in our DTA/TG system (Gaisford, Kett, & Haines, 2016; Herrmann, Spratte, & Schneider, 2017).

The thermal behaviors of $Gd_2O_2SO_4$ and $Gd_2O_2SO_4$: RE xerogel powders were performed to determine decomposition and phase formation at a heating rate of 10 °C/min in the temperature range of 25-950 ºC in dry air by using DTA/TG machine (DTG-60H Shimadzu).

3.3.2.2 Fourier Transform-Infrared Spectroscopy (FTIR)

The infrared spectra of the samples were recorded with a Thermo Scientific Nicolet iS10 instrument equipped with ATR apparatus in the spectral range between 4000 and 650 cm^{-1} with a resolution of 4 cm^{-1} at room temperature after the reactions in the temperature range of 25 ºC and 1100 ºC. All of the samples were characterized by FTIR by which percentage absorbance as a function of wavenumber curves can be obtained. The normal instrumental process is as follows:

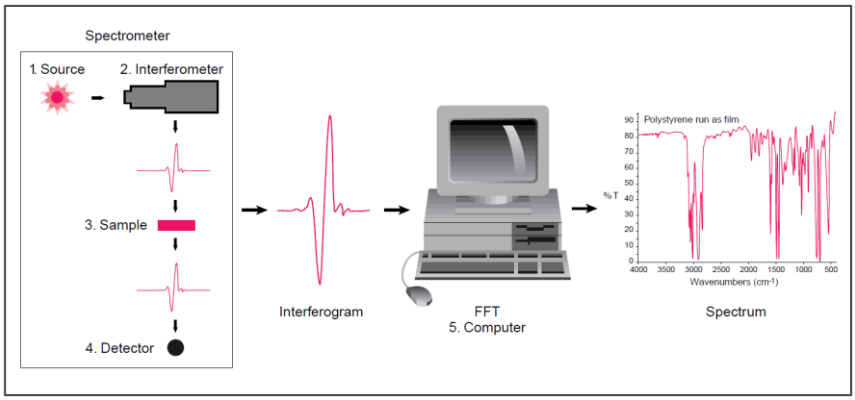

Figure 3.5 Sample Analysis Process (FTIR analysis, n.d.)

FTIR results of the starting solution, gel state and after heat treatment to nanoparticles at 400, 600, 800, 900, 1000 and 1100 ºC respectively were recorded and evaluated.

3.3.2.4 X-ray Photoelectron Spectroscopy (XPS)

Since the binding energies are element specific, the spectrum can be used to describe the components of the sample. This technique is called x-ray photoelectron spectroscopy or XPS.

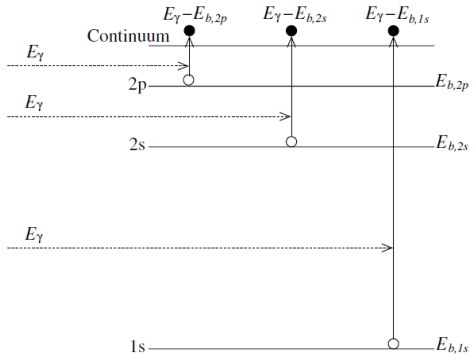

Figure 3.7 Principle of x-ray photoelectron spectroscopy (Ahmed, 2007)

The principle of XPS is graphically depicted in Fig. 3.7. The most tightly bound electron is the 1s electron, which assumes the lowest energy after absorbing an x-ray photon. The electrons in the higher energy levels are emitted with higher energies. Detection of these photons and measurement of their energies then leads to a spectrum as shown in Fig.3.8. The peaks correspond to the transitions shown in Fig. 3.7.

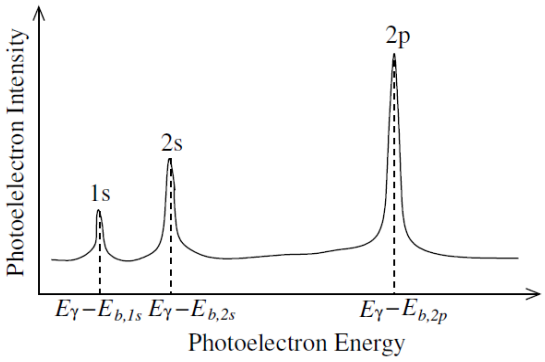

Figure 3.8 A simple XPS photoelectron spectrum. Each peak corresponds to emission of photoelectrons from an atomic level. A typical spectrum contains a number of peaks corresponding to different elements in the sample (Ahmed, 2007)

The reason is not only to detect electrons here but also to measure their energies. The sample and detector were held in a vacuum chamber since the electrons had a very short range even in the air.

Elemental composition and surface chemistry of all samples was analyzed by XPS (Thermo-Scientific) with monochromatic Al-Kα (1486.7 eV) X-ray source and a beam size of 400 nm diameter. The device was calibrated according to gold; 4f7/2. The pressure was kept below $5x10^{-10}$ mbar during spectral data acquisition. The XPS data of the survey scan was scanned from -10 to 1350 eV applying a pass energy of 150 eV and a resolution of 1 eV. 20 scans from a single point were recorded. The pass energy for high-resolution elemental scanning was 30 eV and the scan number was 15 scans.

3.3.2.5 X-ray Diffraction Spectroscopy (XRD)

In this study, phase structures of scintillator materials doped with various rare earth elements were determined by XRD device. The nanoparticles produced correspond to all peaks with the $Gd_2O_2SO_4$ orthorhombic structure. Phase identification and crystal structures of nanoparticles were performed by means of a Thermo Scientific ARL K-alpha X-ray diffractometer. This instrument works with voltage and current settings of 45 kV and 44 mA, respectively, and uses Cu-K_α X-radiation (1.5405 Å). For qualitative analysis, XRD diagrams were recorded in the interval $20° \leq 2\theta \leq 55°$ at a speed of 2 (°)/min.

3.3.2.6 Scanning Electron Microscopy (SEM)

Scanning electron microscopy (SEM) is the most widely used imaging method for examining the surface condition of solid materials. In the SEM device, we scanned the sample surface with a high-energy electron beam. The interaction between the electron beam and the sample resulted in different radiation. This device usually uses 2 types of radiation signal for imaging. They are scattered electrons (primary electrons) and are removed from the material (secondary electrons). Backscattered electrons provide information on the composition and topography of the sample surface. Secondary

electrons were used to show the details of the surface morphology of the material. Figure 3.12 shows the schematic operating principle of SEM.

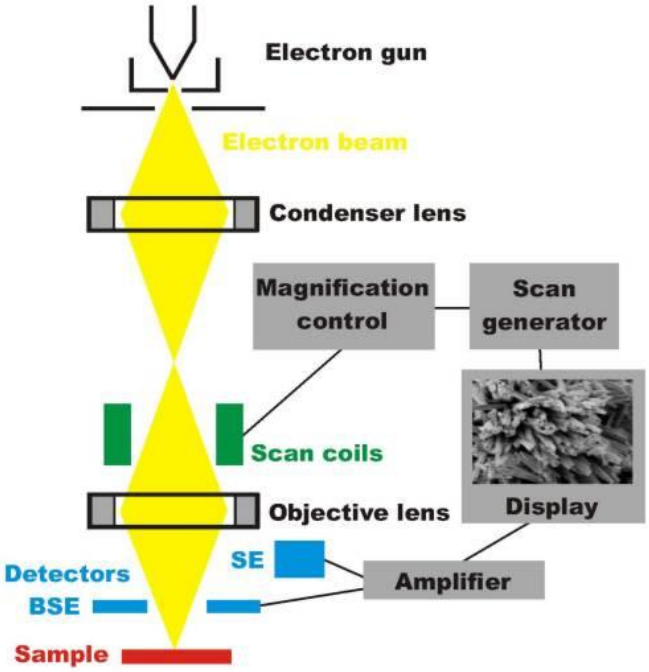

Figure 3.12 The Schematic representation of an SEM (Scanning Electron Microscopy (SEM), n.d.)

The surface qualities, topographies, and morphologies of $Gd_2O_2SO_4$ and $Gd_2O_2SO_4$: RE nanoparticles were examined by using SEM (COXEM E30 plus). Accelerating voltage of 20 kV was used for the SEM imaging.

3.3.2.7 Photoluminescence (PL) and Decay Time Measurements

When an insulator or semiconductor material absorbs electromagnetic radiation (such as a photon), an electron can be stimulated to a higher energy quantum level. If this exciting electron returns a lower energy quantum level by sending a photon, it is called photoluminescence. Photoluminescence spectroscopy is a non-contact, non-destructive method to investigate the electronic structure of materials. In this thesis, light is directed to gadolinium-based samples where it is absorbed and the energy is given to the material. The luminescence properties of the samples were determined as a result of the distribution of this excess energy by the sample. In the thesis,

photoluminescence properties and decay time values of $Gd_2O_2SO_4$ and $Gd_2O_2SO_4$: RE nanoparticles were investigated by using PL device.

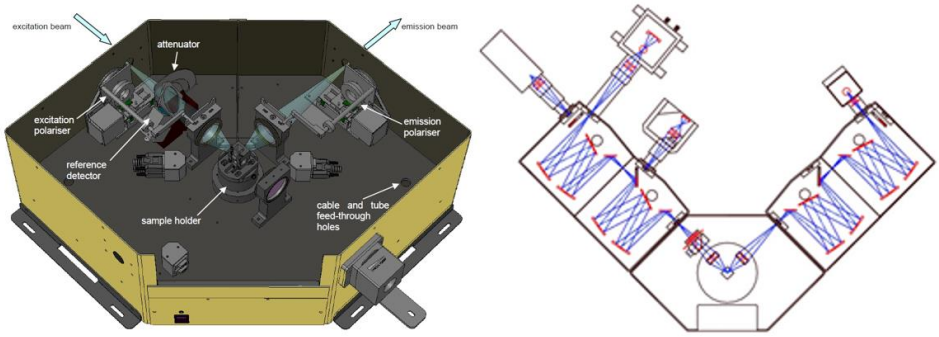

Figure 3.13 The internal structure and the path the light follows of the FLSP920 system (Yildirim, 2017)

The steady-state fluorescence measurements and decay times of the nanoparticles were measured by time-resolved fluorescence spectrometer of Edinburg Instruments of FLSP920. Figure 3.13 shows schematically the internal structure and the path the light follows of the FLSP920 system. "The decay times were recorded on principle of time correlated single photon counting (TCSPC). The instrument was equipped with a standard 15 W xenon lamp and a microsecond flash lamp for steady-state and lifetime measurements, respectively. During measurements, the Instrument Response Function (IRF) was obtained from a non-fluorescing suspension of colloidal silica (LUDOX 30%, Sigma Aldrich) in water. The lifetime parameters were recovered by iterative convolution (re-convolution) with a weighted, nonlinear least squares method using the measured IRF and emission decay data. The reduced chi-square values and plots of weighted residuals were used to determine the 'goodness of fit' between the calculated and measured decay curves. In all cases, the calculated chi-square values (χ^2) were less than 1.2 and the residuals trace symmetrically distributed around the zero axes" (Yildirim et al., 2017).

CHAPTER FOUR
RESULTS AND DISCUSSION

4.1 Solution Characteristics

The pH and turbidity values of the prepared solutions are shown in Table 4.1. The results are discussed in details.

Table 4.1 The characteristic results of the solutions

Phosphor codes	pH	Turbidity value (ntu)
$Gd_2O_2SO_4$	6.31	5
$Gd_2O_2SO_4$_0.5Dy	6.39	10
$Gd_2O_2SO_4$_1.0Dy	6.27	5
$Gd_2O_2SO_4$_3.0Dy	6.53	5
$Gd_2O_2SO_4$_1.0Eu	6.35	5
$Gd_2O_2SO_4$_1.0Pr	6.40	10
$Gd_2O_2SO_4$_1.0Tb	6.35	5
$Gd_2O_2SO_4$_1.0Ce	6.55	5
$Gd_2O_2SO_4$_1.0Ho	6.45	5

4.1.1 pH Results

pH is an important factor for many chemical treatments such as the solubility of the compound, the speed of a reaction and especially for the sol-gel formation (Woodhead & Segal, 1984). The pH value of the solution significantly influences the gelation speed of the solution and the polymeric chain structures formed during gelation. The sol-gel process is based on three reaction mechanisms as hydrolysis, condensation and complexation reactions. At low pH values, the reaction is governed by (H_3O^+) ionic molecules in the solution, and the rapid reaction $H_2O + H^+ \rightarrow H_3O^+$ reduces the amount of the water in the final product. However, for the high pH values of the solution, the

reaction is governed by hydroxides ions (OH^-). Furthermore, at low pH values, the hydrolysis and condensation can generate linear polymers. For high pH values, the reaction leads to highly branched polymers and large polymeric chain. Therefore, with increasing of pH value of reaction solution, the polymeric chains increase in size, which results in a larger crystallite size (Brinker & Scherer, 2013).

The pH properties of $Gd_2O_2SO_4$ based solutions were measured before nanoparticles were formed. These values are presented in Table 4.1. As can be seen from Table 4.1, the results were determined in the range of 6.27 and 6.55. These results show that $Gd_2O_2SO_4$ based solutions exhibit a slightly acidic character. It is easy to see that no changes were observed when the pH measurements of the solutions were repeatedly measured at regular intervals. This is an important factor in terms of gelling time.

4.1.2 Turbidity Results

Suitable precursors, solvents and chelating agents have been found to prevent aging of the solution during formation of the gel. Aging can lead to deterioration of chemical structure, nucleation and growth before solidification. For this reason, aging control should be controlled by turbidity measurement (Ebeoglugil, 2011).

"Turbidity measured this way uses an instrument called a nephelometer with the detector set up to the side of the light beam. More light reaches the detector if there are lots of small particles scattering the source beam than if there are few. The units of turbidity from a calibrated nephelometer are called Nephelometric Turbidity Units (NTU) and is determined in the range of 0-1000 ntu. After the powder-based precursors are dissolved, if the value is close to 0 ntu it is interpreted as completely dissolved and a transparent solution is obtained. If the turbidity value of the solution is close to 1000 ntu then the precursor is not completely dissolved and suspended particles are present in the solution (Wright & Sommerdijk, 2014).

Turbidity results of $Gd_2O_2SO_4$ based solutions are given in Table 4.1. The $Gd_2O_2SO_4$ solutions were determined to be 5.0 ntu. The values of the other solutions were determined between 5 and 10 ntu. The reason for this increase is that the rare earth metal precursors used are colored and the color of the solutions changes. The obtained values compared to 1000 ntu indicate that the powder precursors in the solutions were completely dissolved. Upon examination of the already obtained solutions, a completely transparent appearance was obtained. These results are extremely important in terms of both stoichiometric and physical properties of the nanoparticles (Y. Chen, Hu, & Lang, 1998; Kinekawa & Kitabatake, 1995).

4.2 Material Characterization

4.2.1 Differential Thermal and Thermogravimetric Analysis (DTA-TGA)

DTA-TGA is an extremely important analysis to see the endothermic and exothermic reactions that occur with temperature increase in the material. The weight loss due to the increase in temperature is also determined by this analysis. In this context, all solutions were dried at 100 °C for several hours until gelation occurred and xerogels formed, and subsequently, DTA-TGA analysis was performed by heating up at the rate of 10 ºC/min at temperatures between 25 ºC and 950 ºC under dry air. Almost all of the samples have similar analysis results. This is why the elements doped to $Gd_2O_2SO_4$, the main material, do not change much. Therefore, only the $Gd_2O_2SO_4$ xerogel powders were analyzed in this section. The DTA-TGA curves of $Gd_2O_2SO_4$ based powders are depicted in Figure 4.1. Generally speaking, upon examining the DTA curves, the thermal events can be divided into two categories. Firstly, it can be pointed out that the volatile components are removed from the structure up to 450 ºC, secondly, the oxidation of the material and the formation of different crystal structures. When examining in details, an endothermic reaction removed of water and OH groups is observed between 50-150 °C. These groups are the result of the chemical reactions of the solvents and precursors used in the structure. Many exothermic reactions occur between 150 and 450 ºC. These are the result of the removal of carbon and nitrate-based organic groups from the structure of the precursor materials. It is clearly seen

from Figure 4.1 that carbon-based materials burned out in the temperature range of 150 and 250 ^{o}C and nitrate $(NO_3)^{-1}$ group decomposed at temperatures between 300 and 400 ^{o}C. These reactions last up to 450 ^{o}C and are final because there are no volatile components in the structure. Thermal data for both samples indicated the start of recrystallization at temperatures higher than 450 ^{o}C. After 450 ^{o}C, three endothermic peaks were visible in the structure. The important finding here that these reactions taken place at 500-800 and 840-950^{o}C represent the recrystallization, phase transformation, and formation of the crystal structures, respectively. In spite of the fact that the DTA curve for $Gd_2O_2SO_4$ powder shows recrystallization at temperatures of 475, 620 and 822 ^{o}C, that of $Gd_2O_2SO_4$: RE ($Gd_2O_2SO_4$_RE) exhibits at 880 ^{o}C (I Aritman et al., 2017a; J. Lian et al., 2014).

More specially, as shown later by XRD measurements, this temperature range is characterized by the recrystallization of the product. The remaining endothermic peaks at temperatures above 800 ^{o}C are observed at 956 ^{o}C.

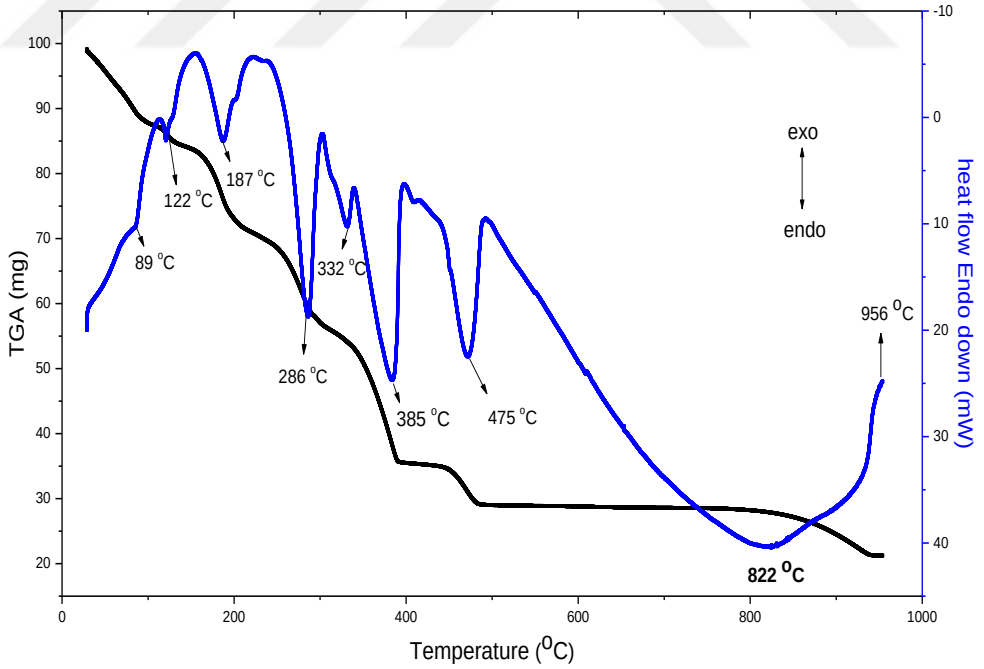

Figure 4.1 The DTA-TGA curves of $Gd_2O_2SO_4$ xerogels

Since our DTA device can process up to 950 ^{o}C, endothermic and exothermic reactions at temperatures above 950 ^{o}C have not been demonstrated. But since the desired phase

is already obtained at about 822 ^{o}C, the experiments made have been sufficient for the thesis. If we give information from extra literature, we can say that when we go over 950 ^{o}C, the sulfur bonds in the structure are broken. As a matter of fact, the Gd_2O_3 cubic structure is formed above these temperatures. This information is supported by the literature (Garcıa-Murillo et al., 2002; Guo et al., 2004). We can also support these results by looking at the organic links in the structure of FTIR results in the thesis.

When focused on TGA curves, the total weight loss value for $Gd_2O_2SO_4$ xerogel is about 68%. The maximum loss values for $Gd_2O_2SO_4$ xerogels were observed up to 450 ^{o}C. Then, in these samples, a slight difference in weight loss was detected up to 950 ° C. A slight increase in temperature up to 822 ^{o}C depends on the crystal structure change and the oxygen input to the material structure. In other words, the weight losses for $Gd_2O_2SO_4$ may show the escape of other volatiles at high temperatures, which may be a reasonable candidate for oxygen due to thermal expansion or thermal expansion of the crystal. The heat treatment regimens of the nanoparticles obtained by taking the temperature values into consideration in the light of this information were determined by using DTA-TGA results.

4.2.2 FTIR Analysis

As a result of the analyzes carried out, it was observed that the inclusion of additional elements did not cause a change in the FTIR results. For this reason, the FTIR results of pure $Gd_2O_2SO_4$ nanoparticles heat treated in solution, gel and at different temperatures were taken into account. In Figure 4.2 all organic binding constructions are seen in the solution at room temperature. FTIR analysis was performed to gain more insight into the structure and composition of the synthesized products. Fig. 4.3 shows FTIR spectra of the optimal precursor and its calcined products at a different temperature, respectively. Evidence of the presence of hydroxyl (OH^{-}), carbonate (CO_3^{2-}) and sulfate (SO_4^{2-}) groups in the precursor can be obtained from FTIR spectroscopy (Fig. 4.3. sol and gel). The spectrum shows the absorption peaks of physically absorbed water, crystal water, hydroxyl groups (near 3442 cm^{-1}, 2870 cm^{-1}), the SO_4^{2-} anions (near 1120 cm^{-1}, 620 cm^{-1}) and the CO_3^{2-} anions (near

1966, 1460 cm^{-1}, 1345, 1275, 1234, 1096, 962, 847 cm^{-1}), which indicates that the precursor is mostly composed of gadolinium hydroxyl, carbonate and sulfate groups with some crystal water. With increasing calcination temperature to 400 °C, the broad absorption band centered at 3400 cm^{-1} becomes much weaker, indicating the removal of crystal water from the precursor.

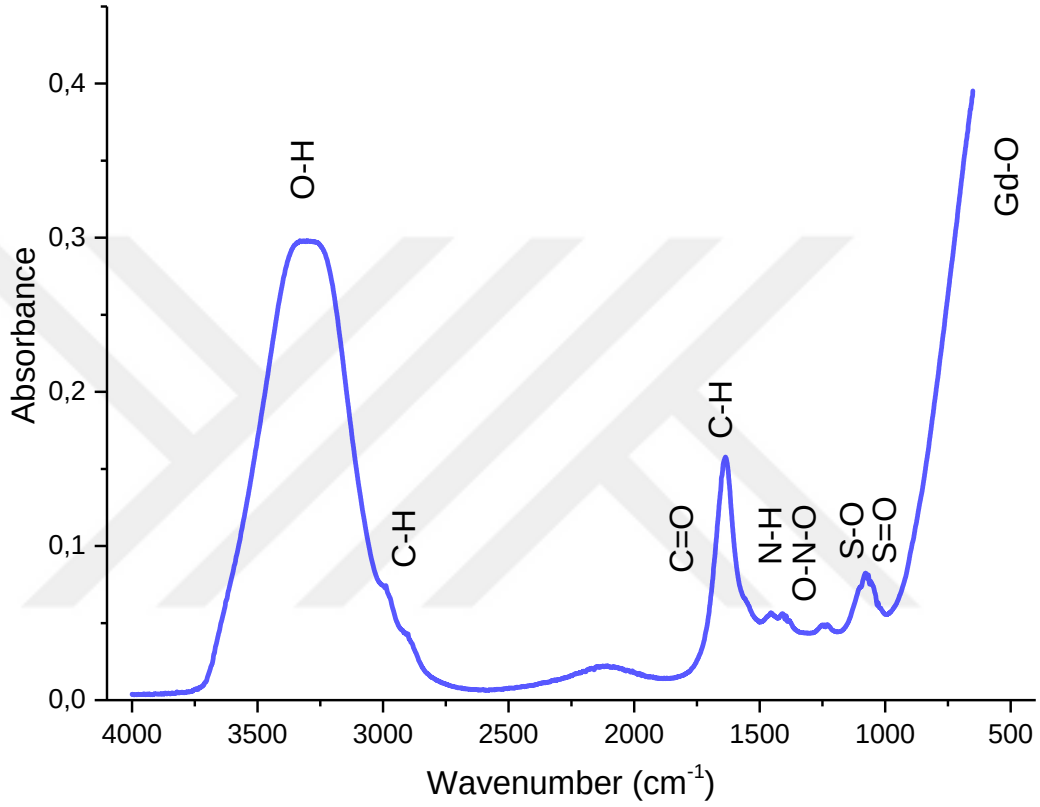

Figure 4.2 FTIR analyses of $Gd_2O_2SO_4$ solution

No significant changes appear for other absorption peaks. With increasing calcination temperature to 600 °C, the absorption band centered at 3400 cm^{-1} becomes negligible, which is associated with the dehydroxylation of hydroxyl groups in the precursor. Moreover, the absorption bands or peaks of CO_3^{2-} and SO_4^{2-} anions still exist, and a new absorption peak centered about 515 cm^{-1} appears, which corresponds to the characteristic vibration peaks of Gd\O bond in the synthesized product. Therefore, the calcined nanoparticles consist of gadolinium hydroxyl, carbonate and sulfate groups. Further increasing the calcination temperature to 800 °C, the CO_3^{2-} absorption bands (1440 cm^{-1} and 1750 cm^{-1}) become negligible, suggesting the

decomposition of CO_3^{2-} anions in the material. The broad SO_4^{2-} absorption bands (around 1120cm^{-1}) split into some narrow peaks and the broad Gd\O bond peak also splits into two narrow peaks (about 515 cm^{-1}), indicating that the precursor has been gradually transformed into $Gd_2O_2SO_4$ phosphor. These results are consistent with those obtained by the DTA–TG–DTG.

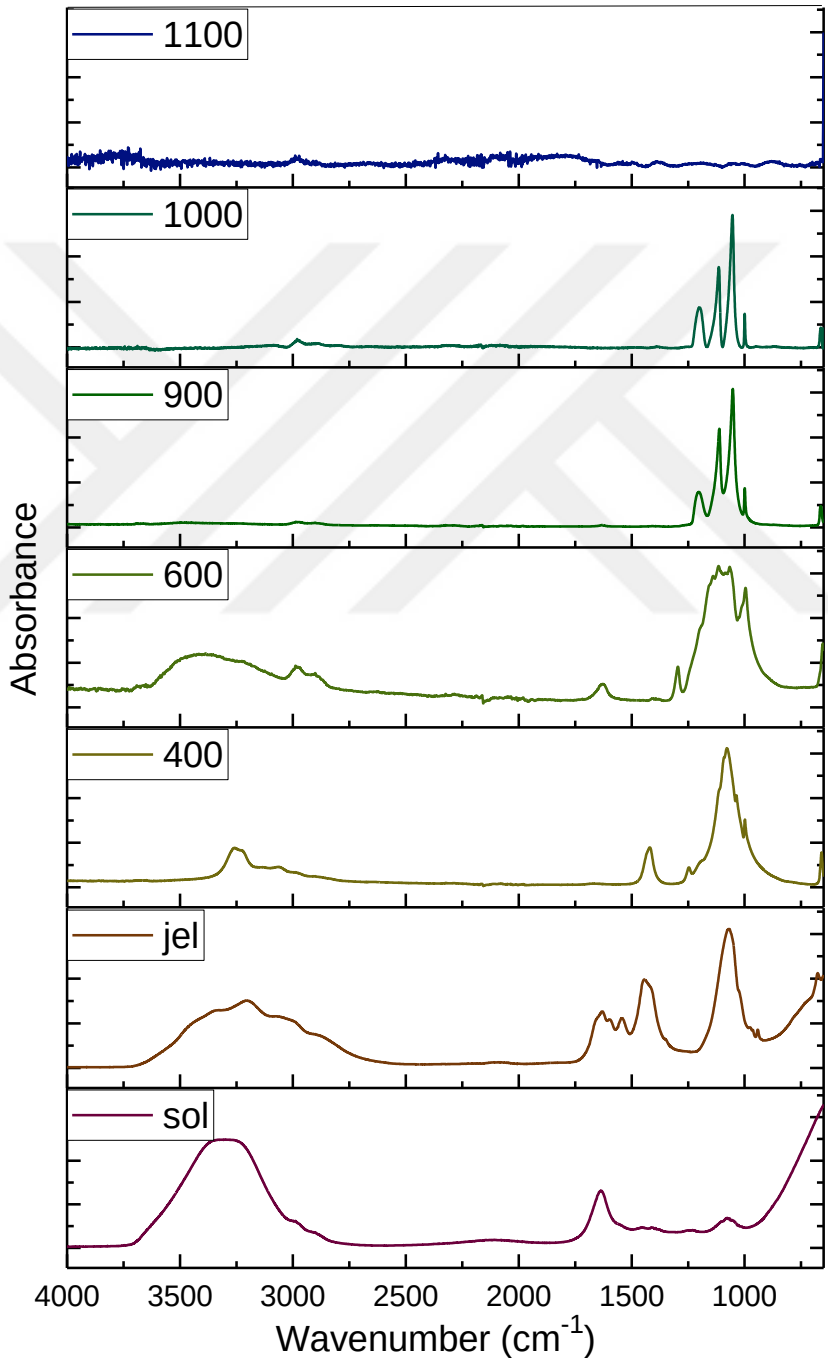

Figure 4.3 FTIR analyses of $Gd_2O_2SO_4$ sol, gel, and nanoparticles at a different temperature

4.2.3 Phase Analysis (XRD)

The XRD pattern of pure $Gd_2O_2SO_4$ nanoparticles produced by the sol-gel method is shown in Figure 4.4. The crystal orientation of a material is controlled by XRD analysis. $Gd_2O_2SO_4$ has an orthorhombic crystal structure. After 1000 degrees the $Gd_2O_2SO_4$ orthorhombic structure becomes Gd_2O_3 cubic structure. This conversion is also clearly visible on the DTA device. In addition, when the organic structures of after heat treatment to the nanoparticles at 900 degrees are examined, it is seen that the sulfate bonds are not in the structure. The unit cell parameters a = 12.996 Å, b = 8.117 Å, c = 4.184 Å and β = 96.58. As already mentioned, $Gd_2O_2SO_4$ has an orthorhombic crystal structure.

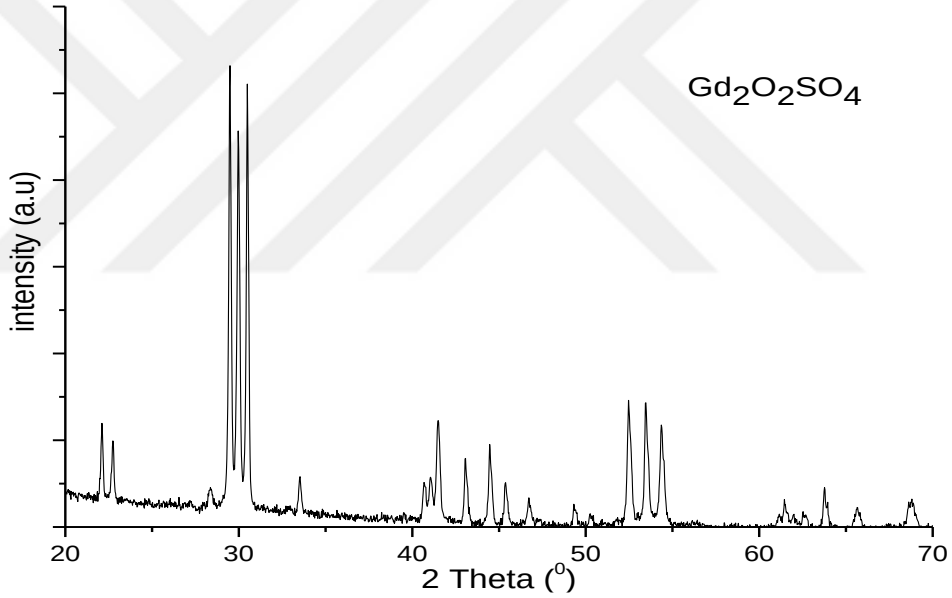

Figure 4.4 Pure $Gd_2O_2SO_4$ phase structure

Crystal structure and morphology strongly depend on temperature and synthesis conditions. The phase structure and crystallinity of phosphors play an important role in the intensity of the cluster. The orthorhombic phase displays an efficient charge transfer process that ensures efficient luminescence emission. This phase is also used in phosphor screens. As clearly shown in Figure 4.4, the nanoparticles heat-treated at 900 in an argon atmosphere were well crystallized. There is good agreement between the DTA-TGA, FTIR and XRD result at this point.

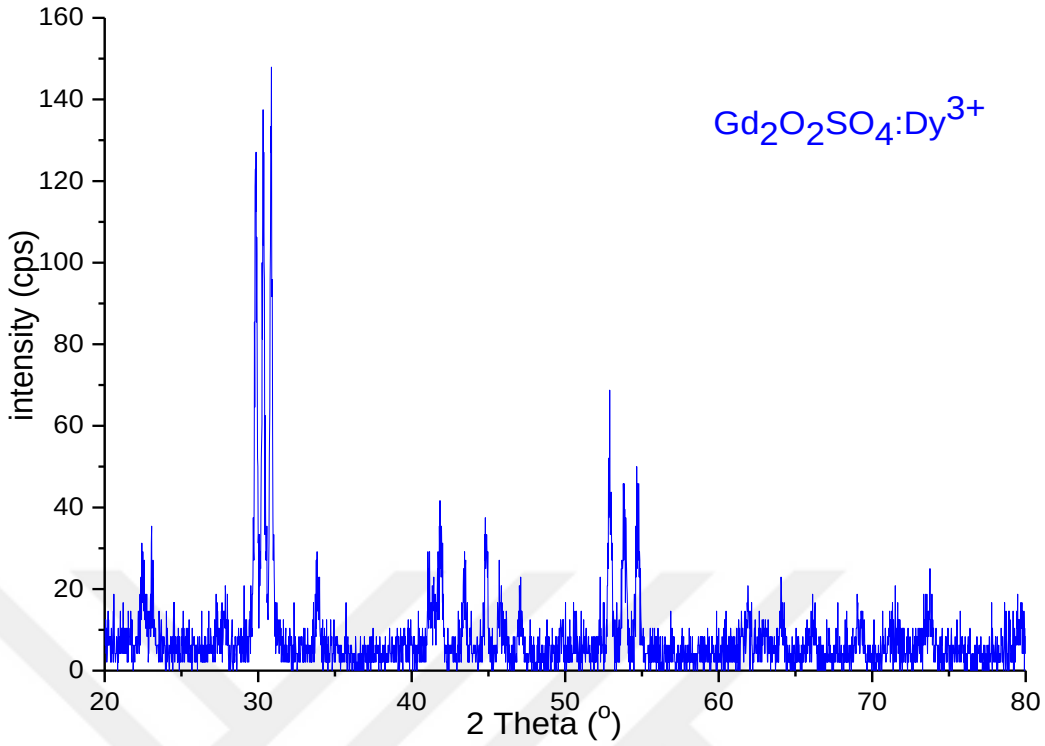

Figure 4.5 The XRD pattern of Dy^{3+} doped $Gd_2O_2SO_4$ nanoparticles

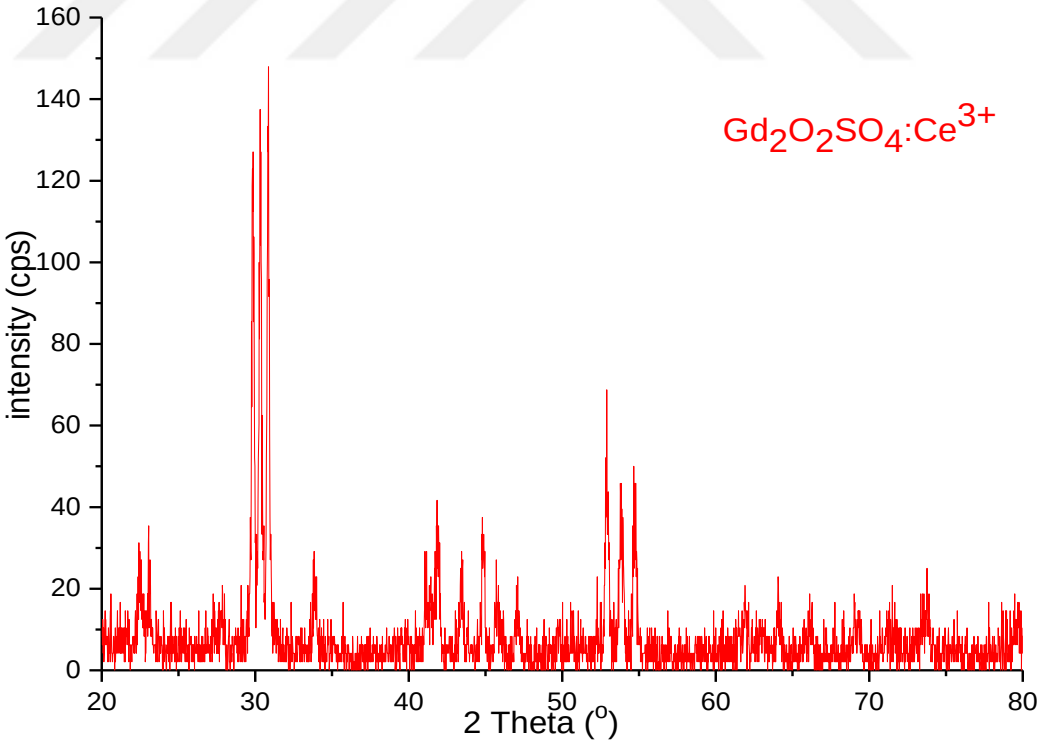

Figure 4.6 The XRD pattern of Ce^{3+}doped $Gd_2O_2SO_4$ nanoparticles

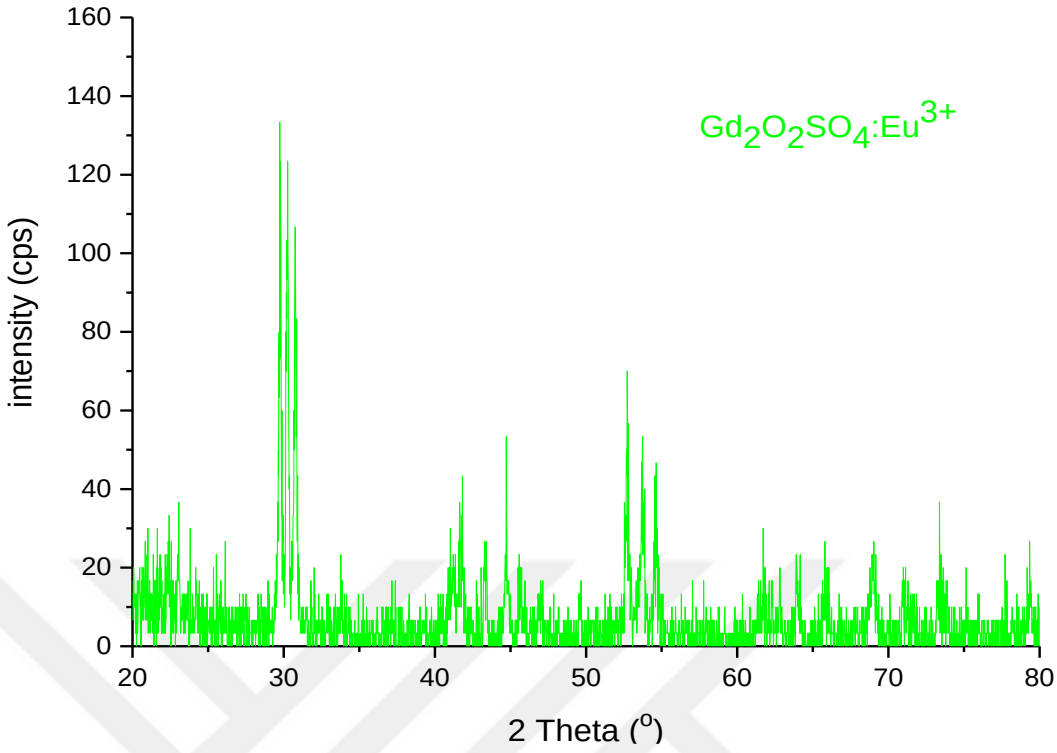

Figure 4.7 The XRD pattern of Eu^{3+} doped $Gd_2O_2SO_4$ nanoparticles

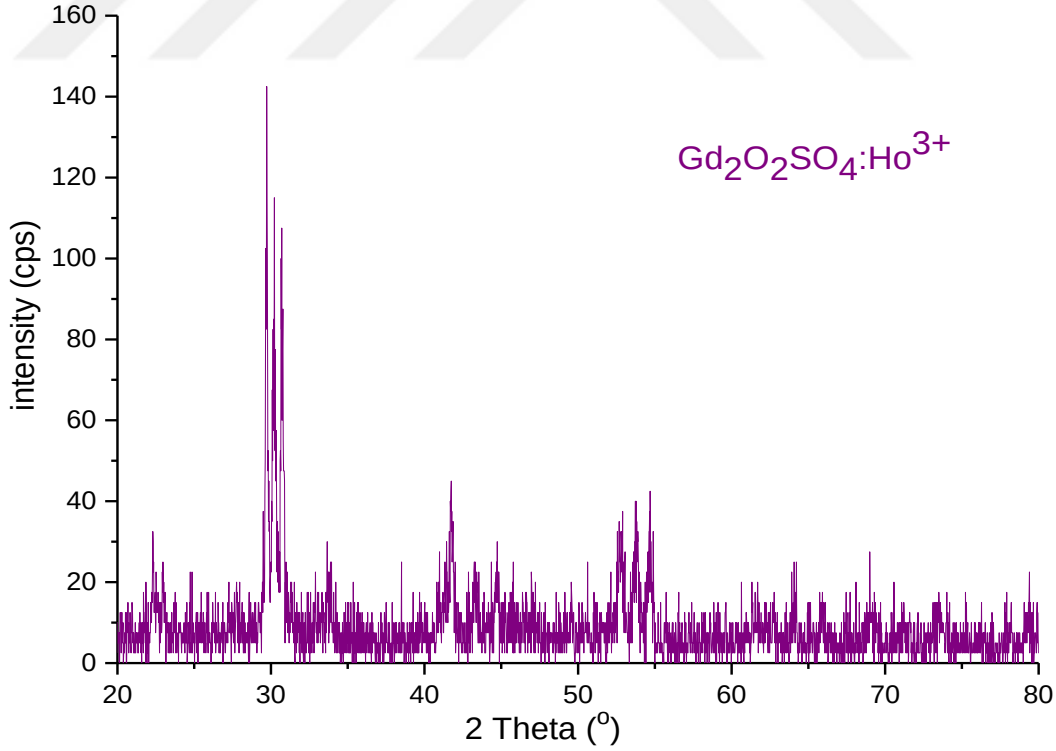

Figure 4.8 The XRD pattern of Ho^{3+} doped $Gd_2O_2SO_4$ nanoparticles

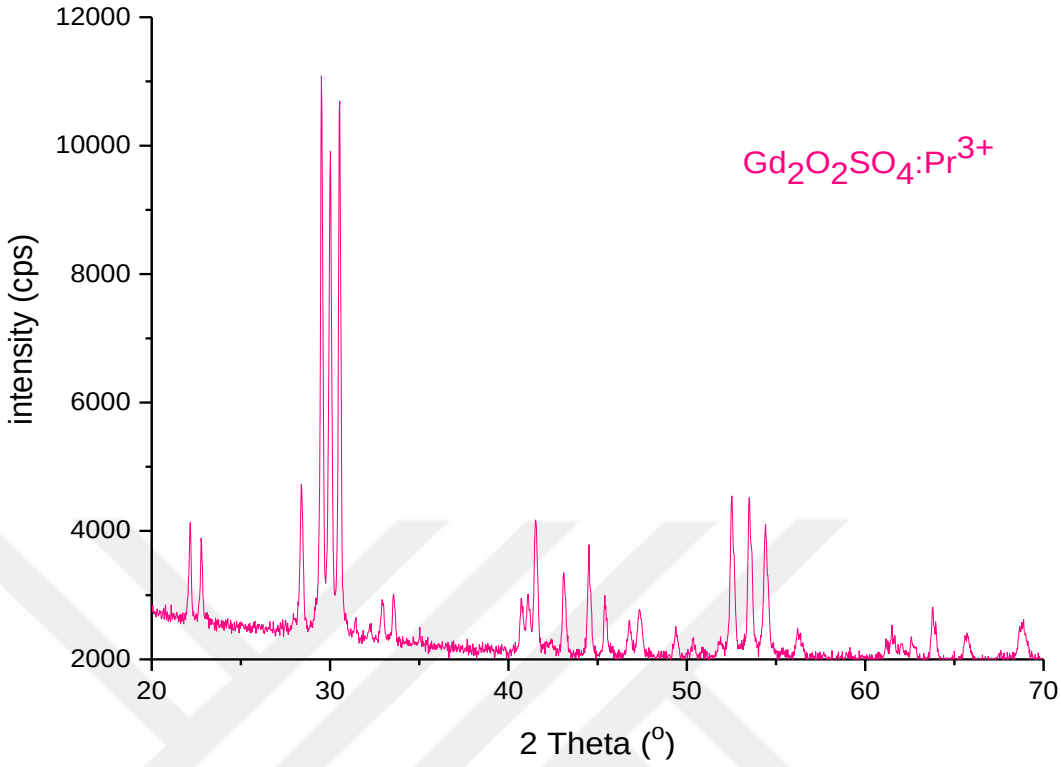

Figure 4.9 The XRD pattern of Pr^{3+} doped $Gd_2O_2SO_4$ nanoparticles

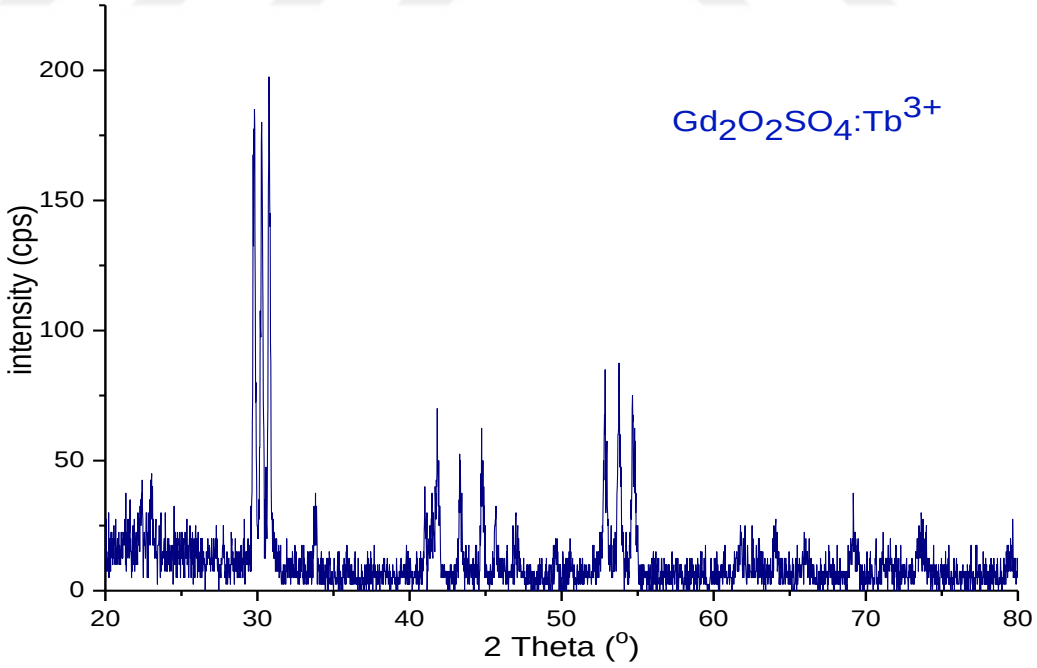

Figure 4.10 The XRD pattern of Tb^{3+} doped $Gd_2O_2SO_4$ nanoparticles

In rare earths-activated $Gd_2O_2SO_4$ nanoparticles, rare earth elements have replaced gadolinium atoms in the structure. The ionic radius of these elements is close to the radius of the gadolinium atom. For this reason, the phase structure did not change significantly. In other words, the substitution of the gadolinium atoms of rare earth elements in the structure did not change the orthorhombic phase crystal structure.

When XRD plots of nanoparticles activated with rare earth elements were examined, the orthorhombic phase structure of pure $Gd_2O_2SO_4$ (JCPDS Card No. 029-0613) was detected. When doped elements with different ion diameters enter the structure, crystal cage plays. This causes the XRD peaks in the different planes to decrease or increase. At the same time, there is a slight shift to the right or left. These results are given in Figure 4.5-4.10.

When XRD plots of $Gd_2O_2SO_4$ nanoparticles doped with different rare earth were examined, some slippage was observed in the cage spacing. The distinct lattice spacing of 0.302 nm and 0.293 nm corresponding to (103) crystal plane and (110) crystal plane, respectively, according to JCPDS Card no 029-0613. Slips in the XRD peaks are thought to originate from relatively different ion radii (Song et al., 2014). As a result, the XRD results were determined to be a single phase of orthorhombic $Gd_2O_2SO_4$: RE^{3+} structure and no other phase was observed.

4.2.4 Elemental Analysis of Nanoparticles (XPS)

XPS analysis was performed to determine the chemical composition and oxidation states of the nanoparticles. Figure 4.11 shows high-resolution elemental scans of pure $Gd_2O_2SO_4$ nanoparticles. The available elements, binding energies, and weights obtained as a result of the analyzes are detailed in Table 4.2. It was observed that $Gd_2O_2SO_4$ was observed at 141.94 eV for photoelectron Gd4d, 168.95 eV for S2p, 530.18 eV for O1 and 284.16 eV for C1s (Table 4.1). It is estimated that C1s elements observed in $Gd_2O_2SO_4$ phosphorus are derived from adventitious hydrocarbons originating from the XPS apparatus itself or from external contaminants. Summit positions are consistent with the values reported in the literature.

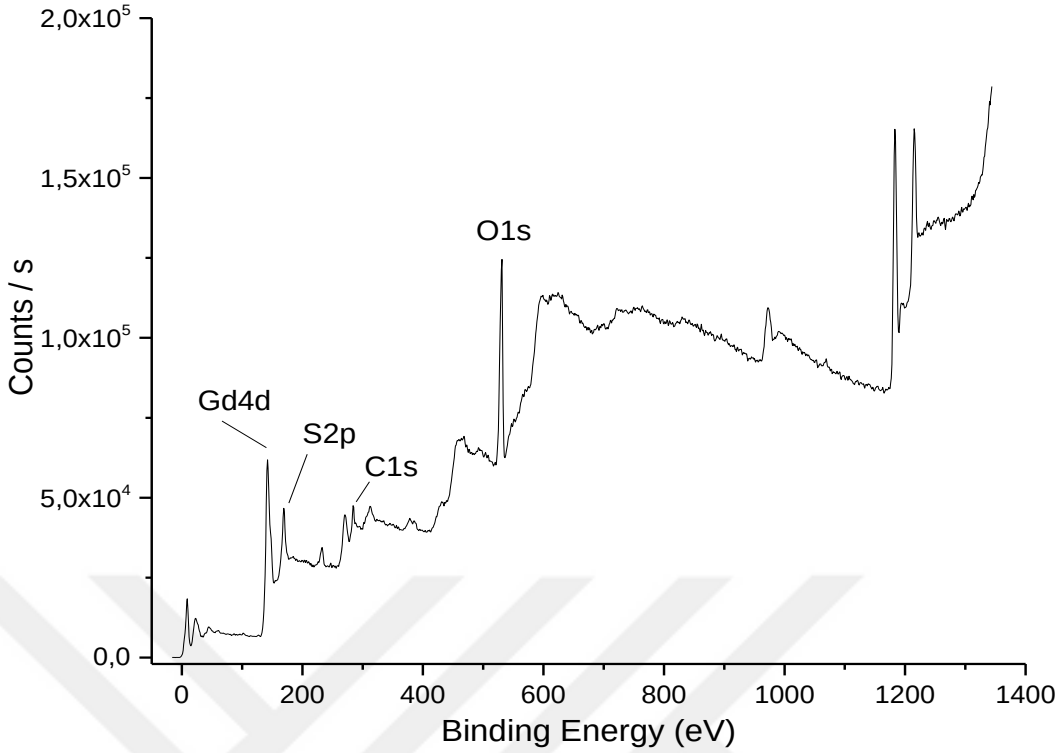

Figure 4.11 The XPS spectra of the $Gd_2O_2SO_4$ nanoparticles

Table 4.2 The XPS results (binding energy and weight %) of $Gd_2O_2SO_4$ nanophosphors

Name	***Binding Energy eV***	***Survey Weight %***
Gd4d	141.94	11.34
O1s	530.18	46.13
S2p	168.95	23.81
C1s	284.16	18.72

These peaks are detailed in the XPS results of all rare earth activated phosphors. Figure 4.12-4.23 show the XPS graphs of rare earth doped nanoparticles. In Figures, it is clear that doped elements such as Dy^{3+}, Ce^{3+}, Eu^{3+}, Ho^{3+}, Tb^{3+}, and Pr^{3+} are present in the structure of $Gd_2O_2SO_4$ phosphors.

High-resolution elemental scans have not been reexamined because the binding energies of these phosphorus elements are almost identical to the binding energies in Table 4.1. Similar results were obtained with the graphs in Figure 4.12-4.23. The detailed results of these particles are given in Table 4.2. Carbon (C1) is also not included in the weight percentages as long as it is present as impurities.

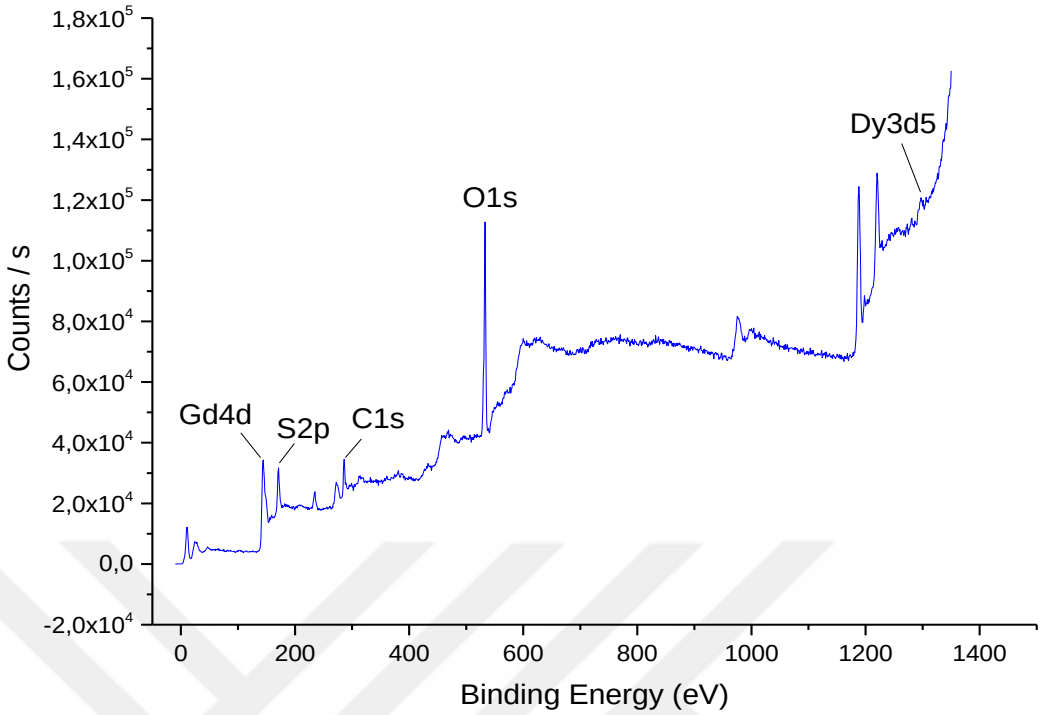

Figure 4.12 The XPS spectra of Dy^{3+} doped $Gd_2O_2SO_4$ nanoparticles (scanned between 0-1400 eV)

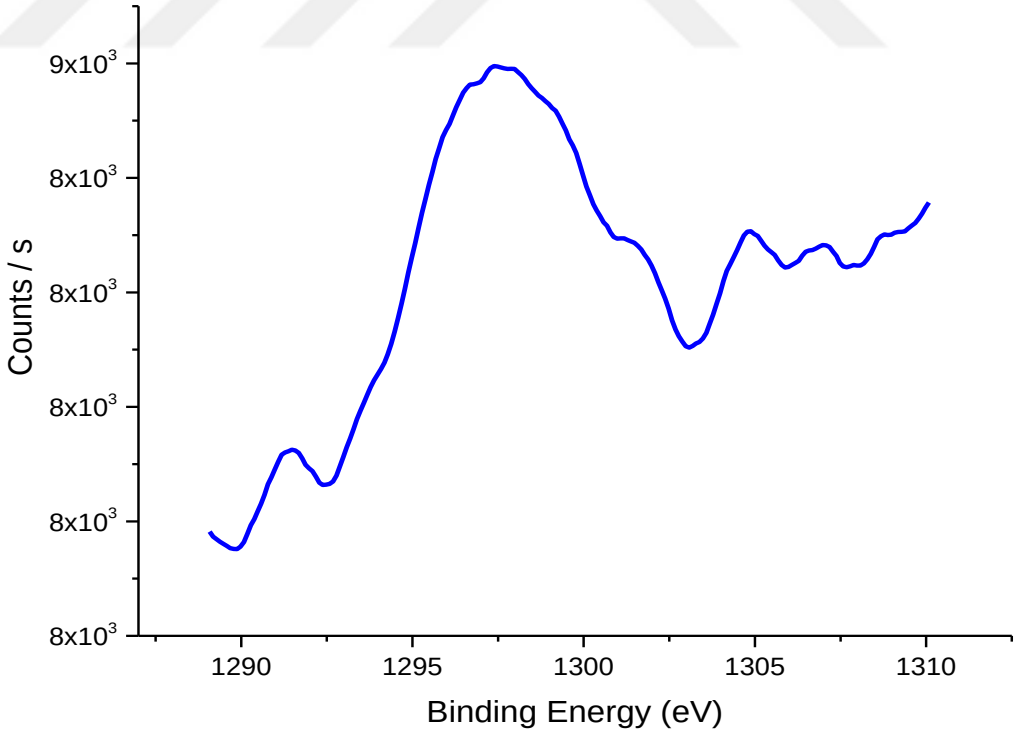

Figure 4.13 The spectra of Dy^{3+} binding energy (a close inside to Dy^{3+} peak)

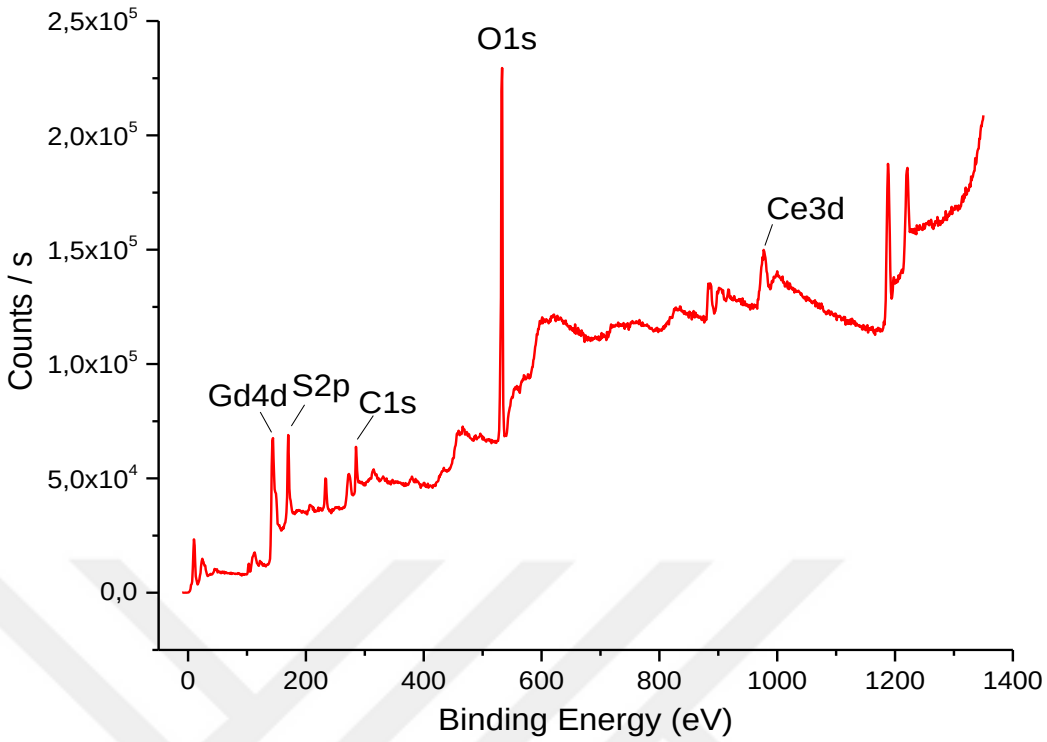

Figure 4.14 The XPS spectra of Ce^{3+} doped $Gd_2O_2SO_4$ nanoparticles (scanned between 0-1400 eV)

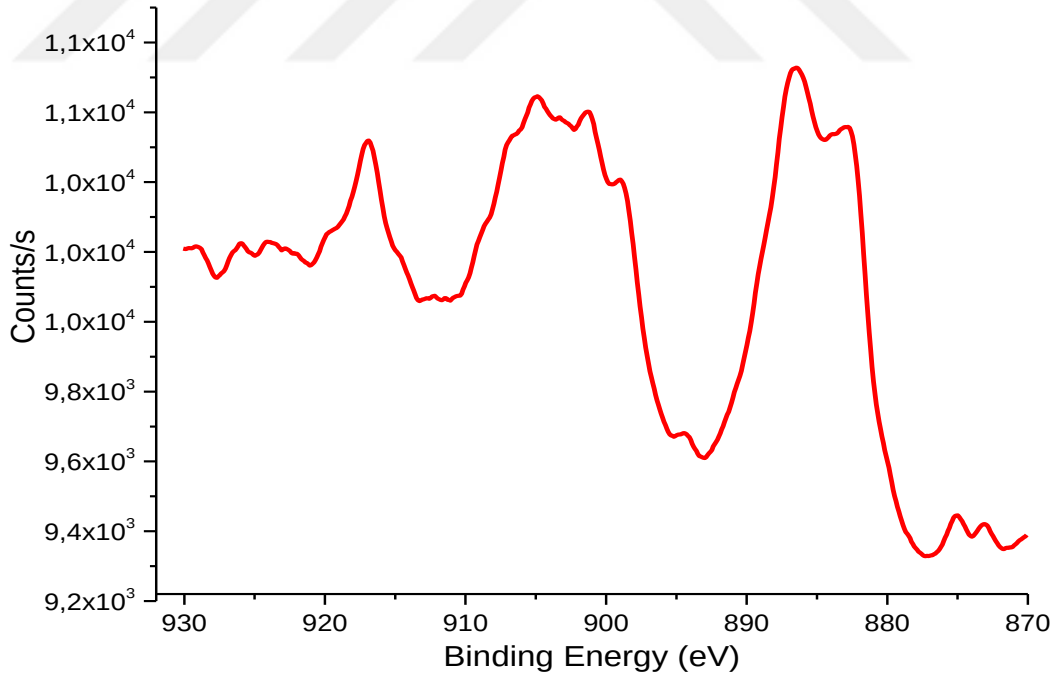

Figure 4.15 The spectra of Ce^{3+} binding energy (a close inside to Ce^{3+} peak)

XPS spectra show sensitivity to identify elements on the surface. Figure 4.12 shows the full XPS spectra of Dy (III) added to the structure of $Gd_2O_2SO_4$ nanoparticles for a large energy band. The Dy (III) can be easily identified by Dy^{3+} 3d XPS lines. Figure 4.13 shows only the binding energies of the Dy^{3+} element.

Figure 4.14 shows the XPS spectra of Ce (III) added to the structure of $Gd_2O_2SO_4$ nanoparticles. The Ce (III) can be easily identified by Ce 3d XPS lines. The binding energy of each element of Ce is shown in figure 4.15 on a large scale. Theoretically, the oxidation state in the bulk form of the Ce element is +3. When examining Figure 4.15, different peak points are detected.

Figure 4.16 shows the XPS spectra of Eu (III) added to the structure of $Gd_2O_2SO_4$ nanoparticles. The Eu (III) can be easily identified by Eu^{3+} 3d XPS lines. The $Gd_2O_2SO_4$: Eu^{3+} sample has four O1s peaks located at 529.6, 530.9, 532.1 and 533.1 eV, which can be assigned to oxygen-oxygen O^{2-}, bridge OH, terminal OH and adsorbed H_2O, respectively (Tan, Fan, Wang, & Grambow, 2009). The binding energies of Eu^{3+} are expressed in detail in Figure 4.17.

Figure 4.18 shows the XPS spectra of Ho (III) added to the structure of $Gd_2O_2SO_4$ nanoparticles. The Ho (III) can be easily identified by Ho^{3+} 3d XPS lines. Elemental analysis of Ho-doped phosphors is not done in the literature. When the binding energies of the Ho element are investigated, there are studies in the range of 130 to 1400 eV (Chopra, Babb, & Bhalla, 1976). In this case, Ho binding energy is the lowest (160 eV) compared to other rare earth elements.

In XPS elemental analysis in Figure 4.20,21, the binding energy of praseodymium element was found to be 933.85 eV. The binding energies of some praseodymium (III) tungstates have been studied in the literature. The value found (935.5 eV) corresponds to the value we obtained in the thesis (Chopra et al., 1976).

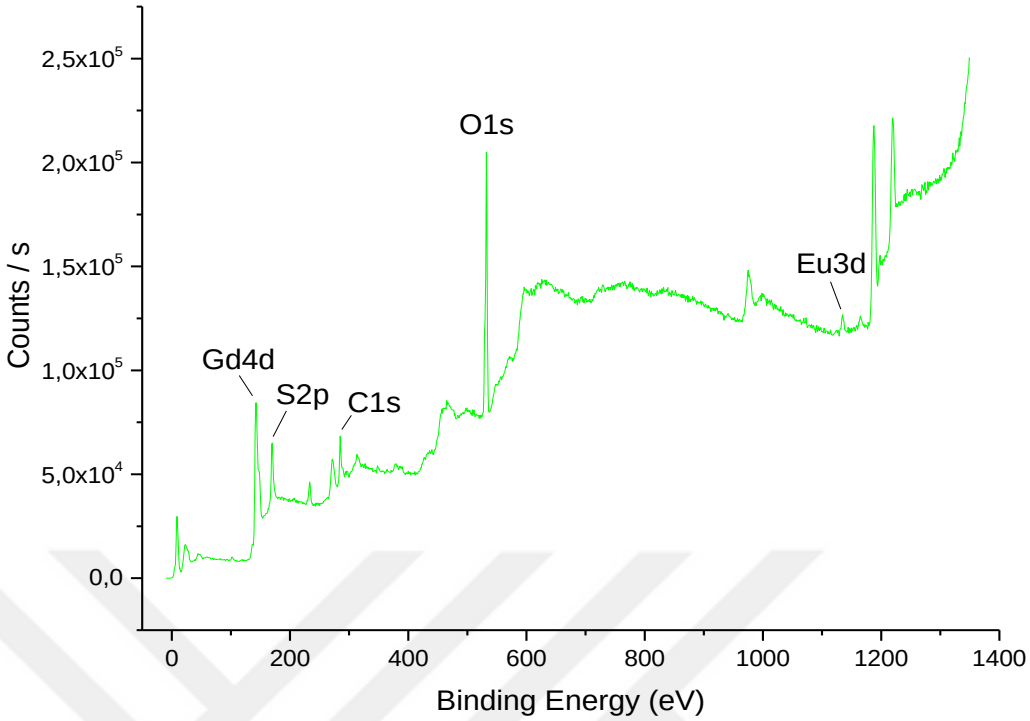

Figure 4.16 The XPS spectra of Eu^{3+} doped $Gd_2O_2SO_4$ nanoparticles (scanned between 0-1400 eV)

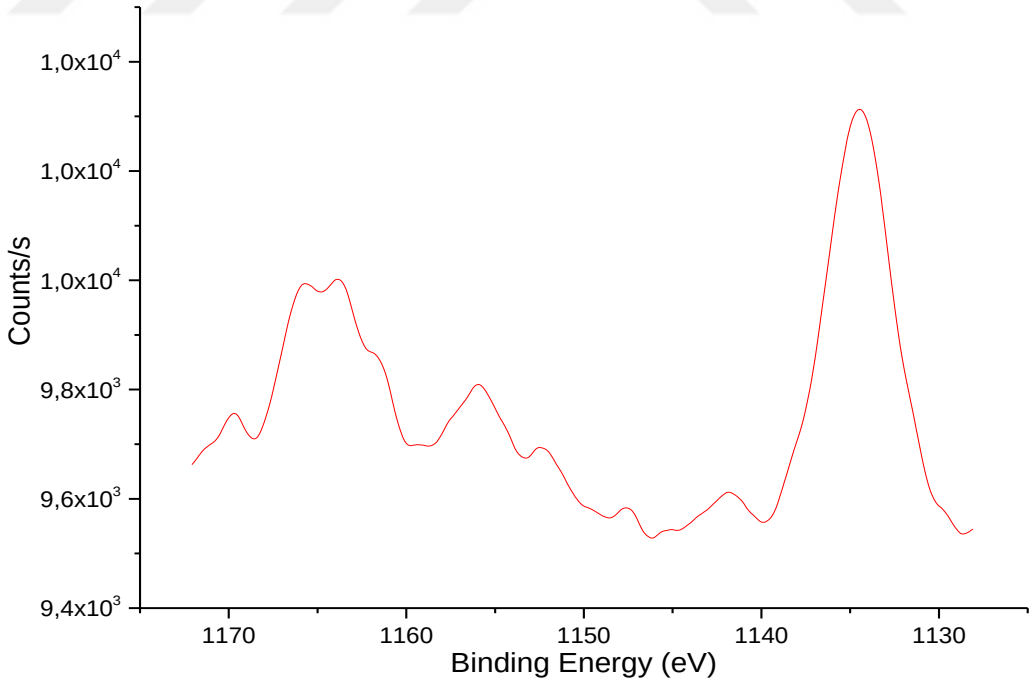

Figure 4.17 The spectra of Eu^{3+} binding energy (a close inside to Eu^{3+} peak)

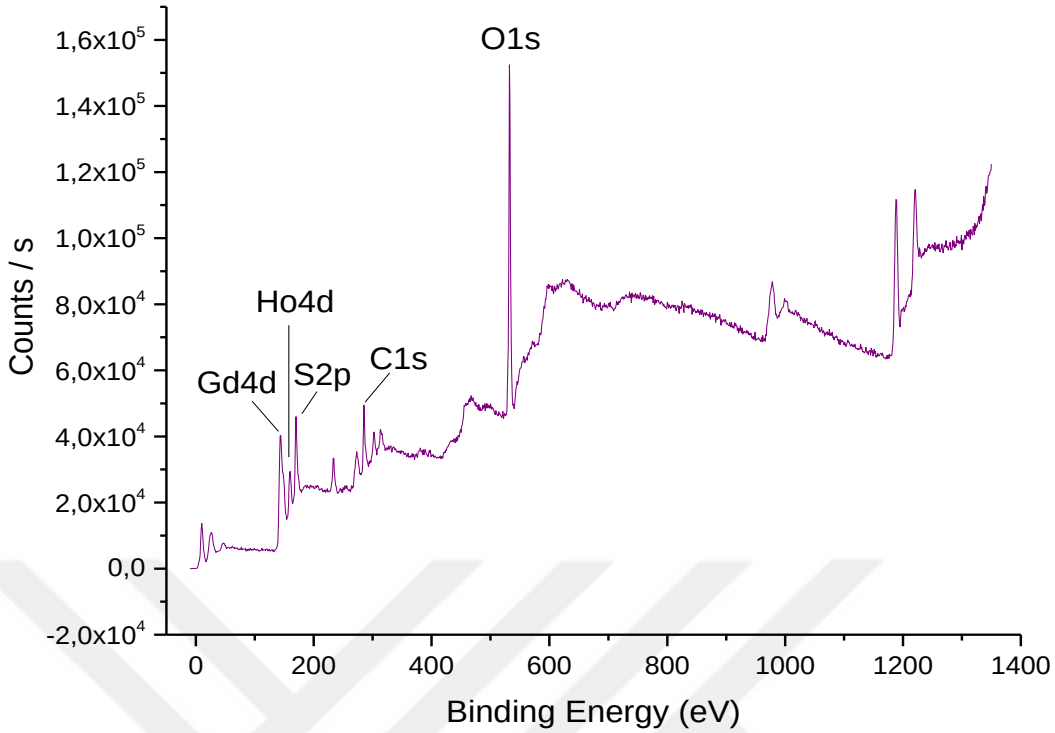

Figure 4.18 The XPS spectra of Ho^{3+} doped $Gd_2O_2SO_4$ nanoparticles (scanned between 0-1400 eV)

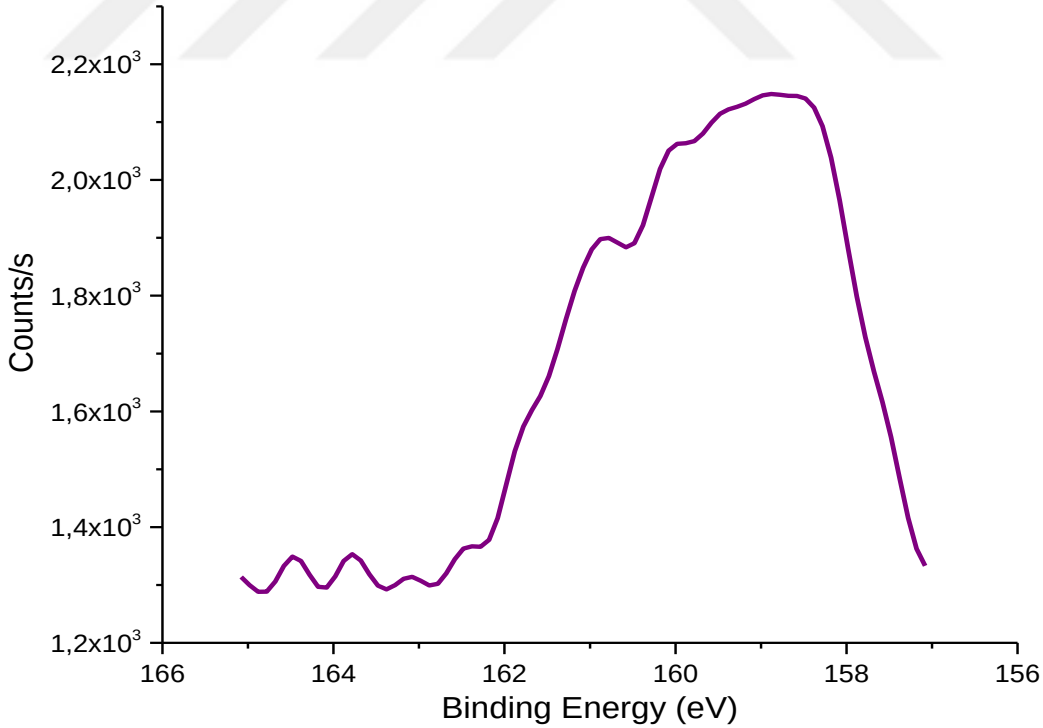

Figure 4.19 The spectra of Ho^{3+} binding energy (a close inside to Ho^{3+} peak)

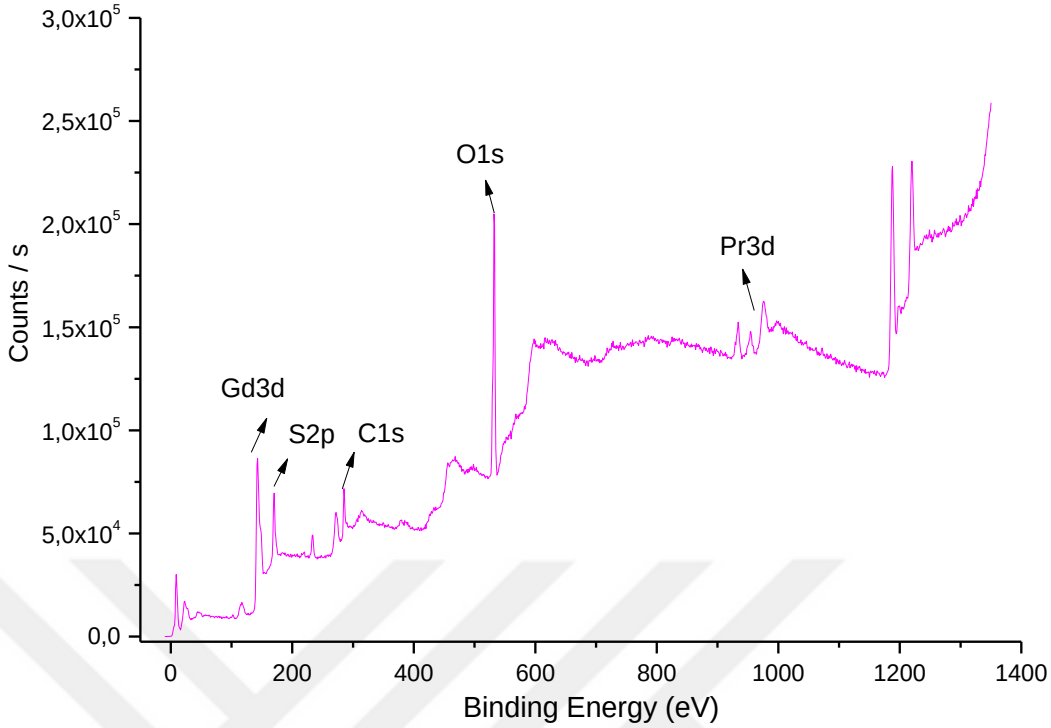

Figure 4.20 The XPS spectra of Pr^{3+} doped $Gd_2O_2SO_4$ nanoparticles (scanned between 0-1400 eV)

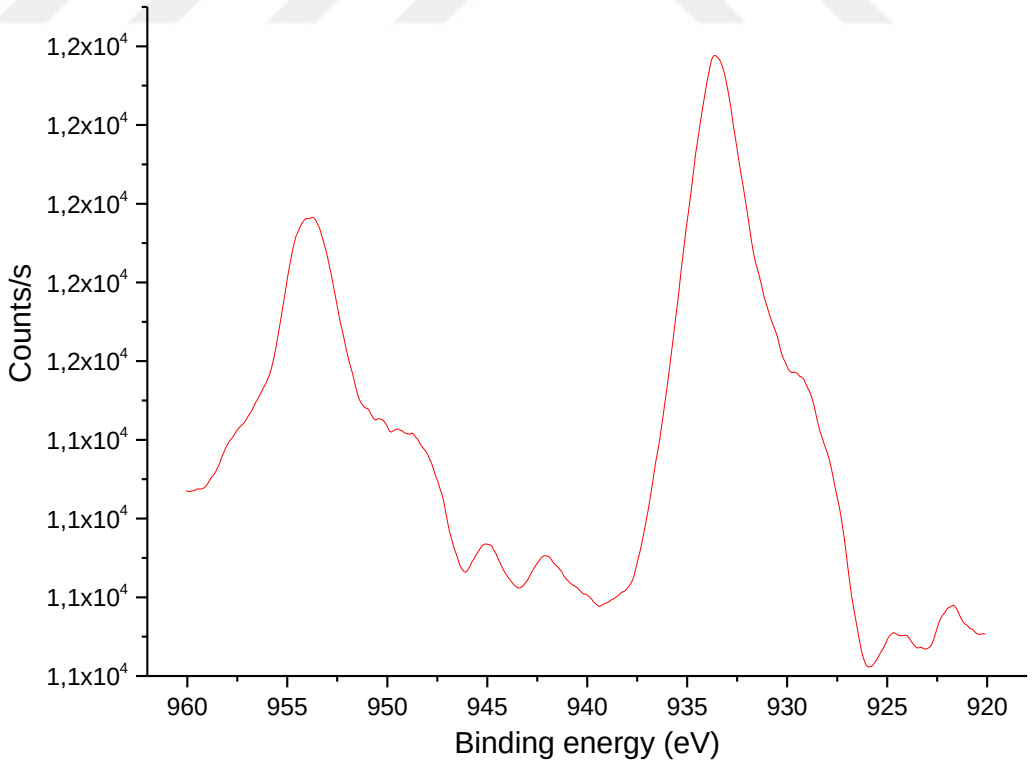

Figure 4.21 The spectra of Pr^{3+} binding energy (a close inside to Pr^{3+} peak)

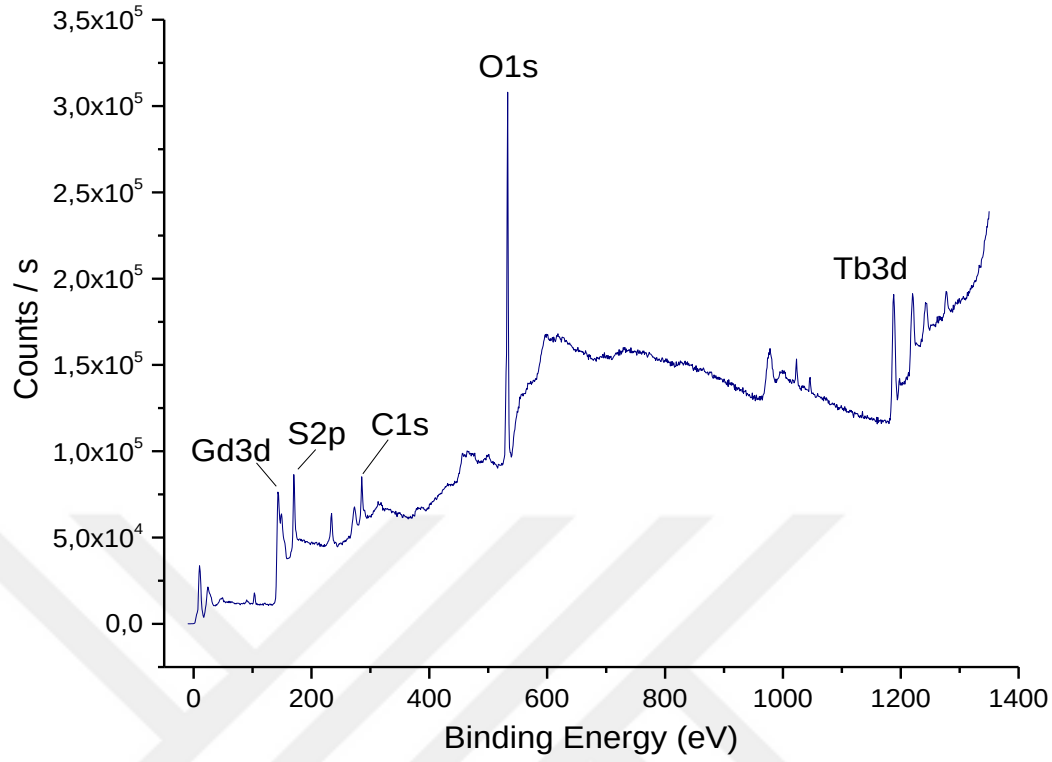

Figure 4.22 The XPS spectra of Tb^{3+} doped $Gd_2O_2SO_4$ nanoparticles (scanned between 0-1400 eV)

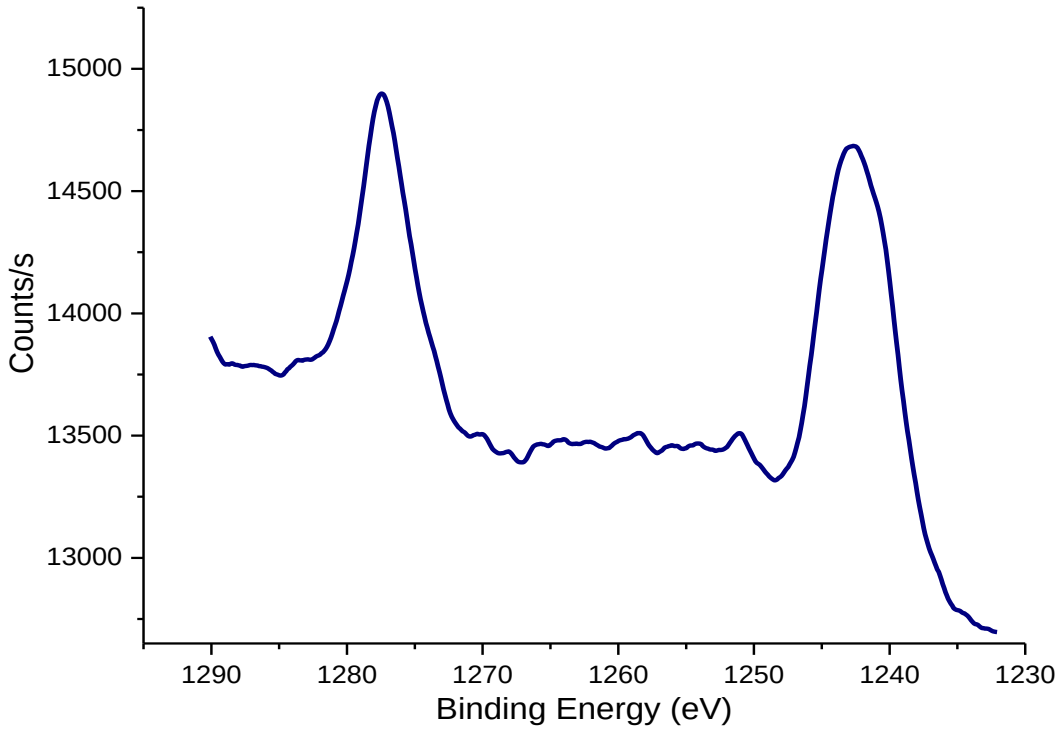

Figure 4.23 The spectra of Tb^{3+} binding energy (a close inside to Tb^{3+} peak)

Table 4.3 The XPS results (binding energy and weight %) of $Gd_2O_2SO_4$: Dy^{3+} nanophosphors

Sample name	Elements	Binding energy (eV)	Survey weight (%)
$Gd_2O_2SO_4$_1.0Dy	Gd 4d	143.95	34.89
	S 2p	170.85	19.55
	C 1s	285.99	8.82
	O 1s	532.97	30.82
	Dy 3d5	1296.34	0.93
$Gd_2O_2SO_4$_1.0Ce	Gd 4d	143.50	32.22
	S 2p	170.03	20.01
	C 1s	285.30	7.65
	O 1s	532.74	30.61
	Ce 3d	985.28	1.05
$Gd_2O_2SO_4$_1.0Eu	Gd 4d	158.21	24.77
	S 2p	169.56	21.83
	C 1s	285.07	7.63
	O 1s	532.11	21.99
	Eu 3d	1134.79	0.88
$Gd_2O_2SO_4$_1.0Ho	Gd 4d	143.52	34.49
	S 2p	170.02	31.46
	C 1s	285.25	8.60
	O 1s	532.38	24.67
	Ho 4d	160.27	0.78
$Gd_2O_2SO_4$_1.0Pr	Gd 4d	142.80	44.32
	S 2p	169.93	21.40
	C 1s	285.20	6.67
	O 1s	532.23	22.12
	Pr 3d	933.85	0.98
$Gd_2O_2SO_4$_1.0Tb	Gd 4d	143.81	27.50
	S 2p	170.14	31.45
	C 1s	285.27	16.1
	O 1s	532.86	27.50
	Tb 3d	1142.37	1.03

Figure 4.22, 23 shows the XPS spectra of Tb (III) added to the structure of $Gd_2O_2SO_4$ nanoparticles. The Tb (III) can be easily identified by Tb^{3+} 3d XPS lines.

The additive Tb^{3+} plays an intermediate role in activator energy transfer from the host absorption band. (Wu et al., 2002; Sohn, Kim, & Woo, 2003).

High-resolution elemental scans have not been reexamined because the binding energies of these phosphorus elements are almost identical to the binding energies in Table 4.3. Results obtained in the graphs shown between Figure 4.12-4.23 support these findings.

As a result, the binding energies of additive elements outside Ho^{3+} are found to be greater than the binding energy of all elements in the main structure. The elements Tb^{3+} and Dy^{3+} are the highest in terms of binding energies.

4.2.5 Surface Morphologies of Nanoparticles (SEM)

Surface morphology, composition, and topography are important factors for nanoparticles. In principle, these factors strongly influence surface quality. Regarding this, SEM images have been examined and their results discussed.

Figure 4.24 shows the surface morphology of $Gd_2O_2SO_4$ nanoparticles activated with rare earth at different magnifications. Numerous small nuclei were formed in the sol-gel system, and the growth of the nucleus leads to the formation of nanoparticles due to the high anisotropic crystal structure nature.

Most of the nanoparticles tend to aggregate into an orthorhombic structure during the course of the reaction, in order to reduce the surface energy. Sol-gel synthesis involves dissolution-recrystallization and further growth processes (Wright & Sommerdijk, 2014).

The SEM image of $Gd_2O_2SO_4$: Tb^{3+} nanoparticles at 10x magnifications are shown in Figure 4.24. The SEM image clearly indicated that $Gd_2O_2SO_4$: Tb^{3+} structure consisted of cactus needle-like nanoparticles assembled by orientation mechanism. Each needle grains were observed to be 100-200 nm in size. These results showed that

the rod-like structure was more stable than the spherical structure. The results are consistent with the literature (I Aritman et al., 2017a; Song et al., 2014).

The SEM image of $Gd_2O_2SO_4$: Eu^{3+} shows a cactus needle-like particle formation. Examination of images shows that fusion between particles may contribute to growth by the orientation mechanism in the complexation method. Consistent with the SEM results, the mean width of the middle of the needles was measured at 80-100 nm. The results are consistent with the literature (I Aritman et al., 2017b; J. Lian et al., 2014; Manigandan et al., 2015).

The $Gd_2O_2SO_4$: Dy^{3+} nanoparticles are shown at 5x magnification. A homogeneous distribution and needle structure are also evident here. As shown in Figure 4.24, Dy-doped nanoparticles have a diameter of about 200-800 nm. The results are consistent with the literature (J. B. Lian et al., 2011).

Also, it can be clearly seen in Fig. 4.24 that the Pr^{3+} particles are orthogonal in shape, well dispersed and about 100-800 nm in size. The urea used in the synthesis of phosphorus nanoparticles removes the nanoparticles from the round, resulting in a rod shape. Since the surface energy of the rod-shaped nanoparticles will be lower, a more stable structure is formed. The results are consistent with the literature (I Aritman et al., 2017c).

The $Gd_2O_2SO_4$: Ce^{3+} nanoparticles are shown at 5kx magnification. Clusters can be seen when the structure is activated with cerium. Particles are in different nano sizes and needle-shaped.

$Gd_2O_2SO_4$: Ho^{3+} nanoparticles are shown at 10kx magnification. When the microstructure is examined, it is a homogeneous distribution. Needle-shaped nanoparticles are regularly distributed.

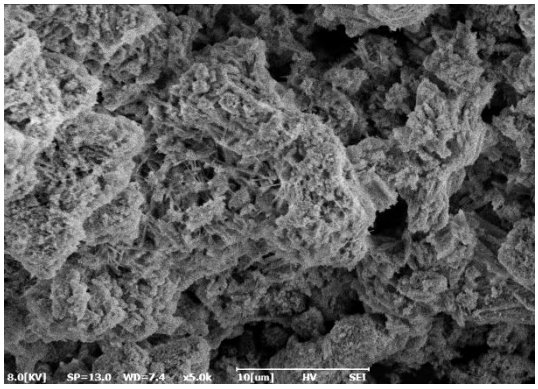

$Gd_2O_2SO_4$: $1.0Ce^{3+}$

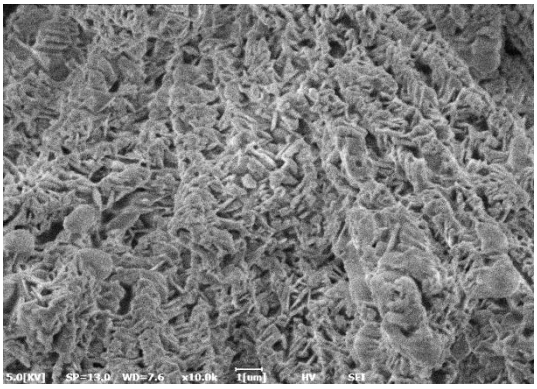

$Gd_2O_2SO_4$: $1.0Dy^{3+}$

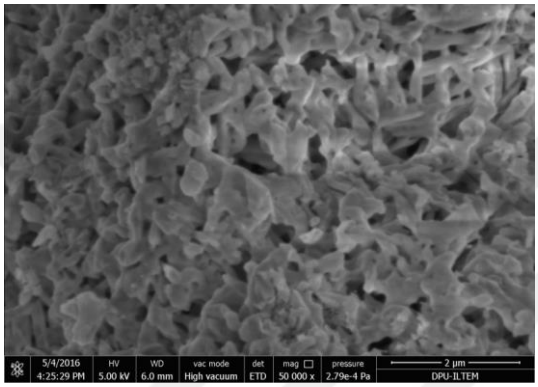

$Gd_2O_2SO_4$: $1.0Eu^{3+}$

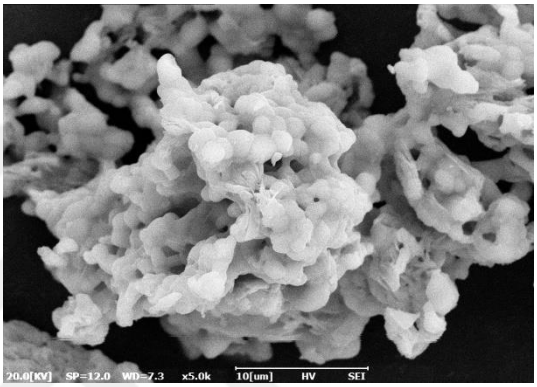

$Gd_2O_2SO_4$: $1.0Ho^{3+}$

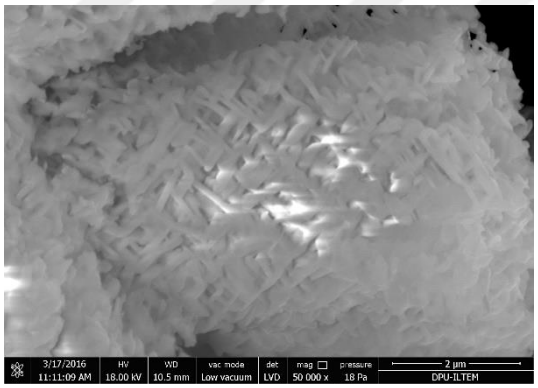

$Gd_2O_2SO_4$: $1.0Pr^{3+}$

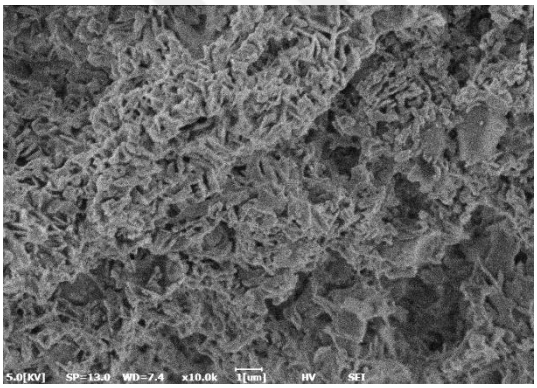

$Gd_2O_2SO_4$: $1.0Tb^{3+}$

Figure 4.24 The SEM images of $Gd_2O_2SO_4$: RE^{3+} (Ce, Dy, Eu, Ho, Pr, Tb) nanoparticles

4.2.6. Luminescence Properties of Nanoparticles

4.2.6.1 Photoluminescence Properties of Nanoparticles

The energy transfer process can increase the excitation light and hence the intensity of the intensity of the light. For phosphors with sensitizer and activator, effective

energy transfer occurs with the excitation spectrum of the activator and the emission spectrum of the sensitizer. In the excitation and emission spectra, the peaks arising from Raman scattering were removed from the graphs. In all the results, Raman scatterings were seen in wavelengths of two and three times the excitation wavelength. Interruptions in the graphs are the result.

Photoluminescence spectra were tested at room temperature for all samples to investigate the luminescence properties of $Gd_2O_2SO_4$ phosphors doped with rare earth elements. When the rare earth element ions are incorporated into the host crystal lattice, an electric dipole f-f transition is partly permitted due to a single crystal field component. The site symmetry of the rare earth elements and the crystal of the doped material is important for the intensity of the electric dipole transitions. On the contrary, the magnetic dipole f - f transitions are only a small measure affected by the symmetry of the ground, because parity is allowed (D. Xu, Yu, & Tian, 2017).

Figure 4.25 shows PL emission spectra due to the Dy^{3+} concentration of $Gd_2O_2SO_4$: Dy^{3+} nanoparticles. Three different Dy^{3+} concentrations were studied, 0.5, 1.0 and 2.0, respectively. As shown in the graph, the emission intensity is increased until the amount of reinforcement is 1%. When this value was exceeded, it was observed that the emission intensity decreased. For this reason, only 1.0 percent of the other rare earth elements have been studied. In the literature, the concentration of emission peaks increases up to 1.0% of RE^{3+} ions, after which the concentration decreases due to the concentration quenching. This quench results from an increase in the ion-ion interaction triggered by the shorter distance between the interacting activators as the concentration increases.

In addition, in the photoluminescence graphs of $Gd_2O_2SO_4$ nanoparticles activated with all rare earth, the peaks observed at about 310 nm are attributed to the transition of the gadolinium element. For this reason, it is seen in all emission results.

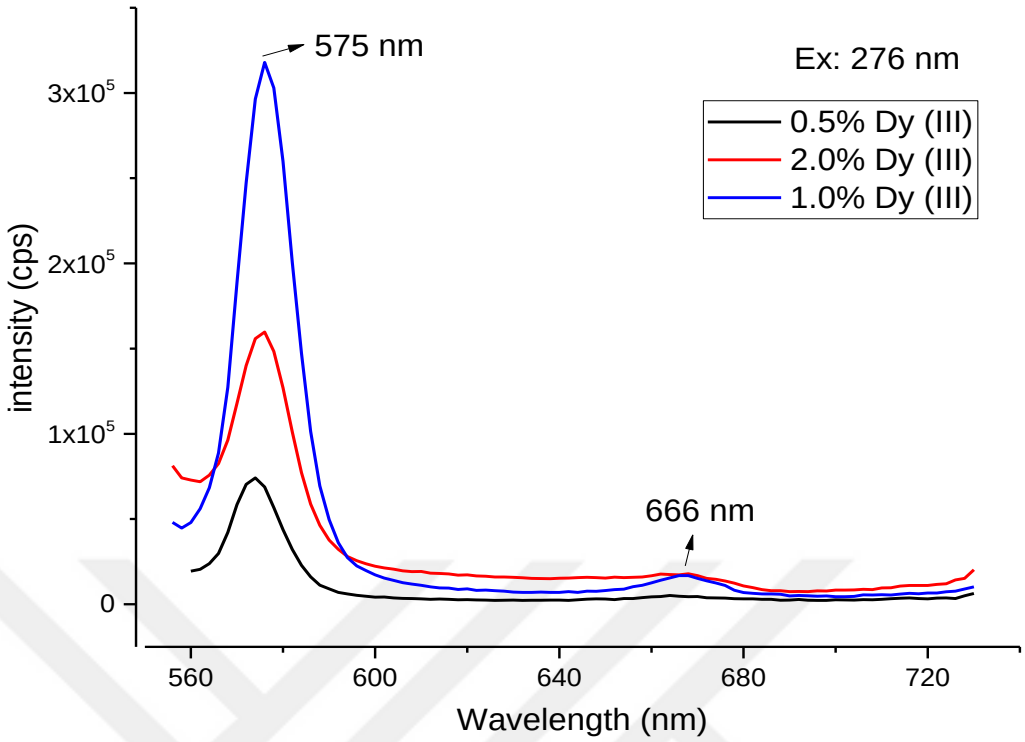

Figure 4.25 The emission spectrum of $Gd_2O_2SO_4$ nanoparticles, depending on the Dy^{3+} concentration

Figure 4.25 shows the $Gd_2O_2SO_4$: Dy^{3+} PL emission spectrum under UV excitation at 276 nm. Significant transitions of Dy^{3+} at the end of excitation were observed. Photoluminescence (PL) spectroscopy reveals that the strongest and second emission peaks are located at 575 nm and 666 nm under 276 nm UV light excitation, which corresponds to the $^4F_{9/2} \rightarrow {}^6H_{13/2}$ and $^4F_{9/2} \rightarrow {}^6H_{11/2}$ transitions of Dy^{3+} ions, and both transitions of Dy^{3+} ions have three exponential decay behavior. The inversion of the dysprosium atom is allowed because it contains a non-symmetric symmetry field. White light means daylight. Daylight turns into different colors at different wavelengths and frequencies after passing through any prism. Dy^{3+} is very close to white color emission and actively used as an activator ion in the design of LED-based light source (Dutta, Som, & Sharma, 2015; J. B. Lian et al., 2011). Herein we offered $Gd_2O_2SO_4$: Dy^{3+} nanoparticles as potential scintillator materials however they also can be concluded as promising white light producing materials.

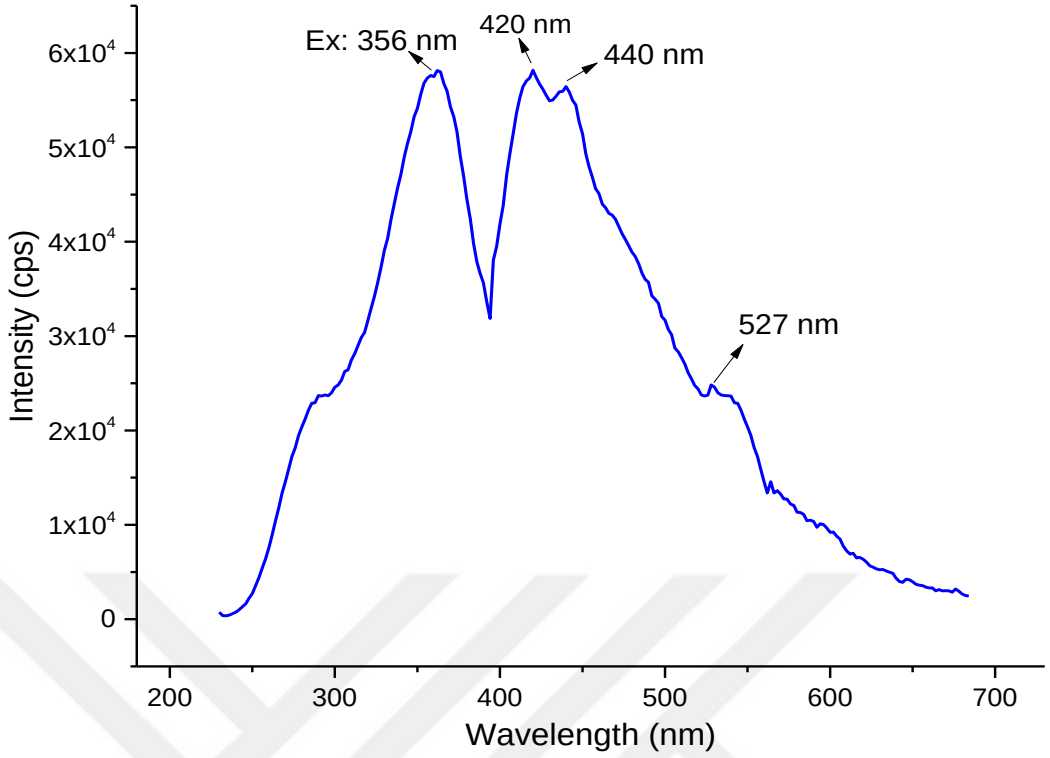

Figure 4.26 Excitation and emission spectra of the $Gd_2O_2SO_4$: Ce^{3+} doped nanoparticles

Figure 4.26 shows the excitation and emission spectra of $Gd_2O_2SO_4$: 1.0 % Ce^{3+} doped phosphors. When excited at 356 nm, three emission bands observed at 420, 440 and 527 nm, respectively. These three bands are caused by the permissible transitions between the crystal field divided by 5d levels and the ground state. Under 356 nm excitation, an asymmetric blue emission band centered at approximately 527 nm can be observed, which can be attributed to the $^5D_1 \rightarrow {}^4F_1$ transition of Ce^{3+}. Asymmetry of the emission band for $Gd_2O_2SO_4$: 1.0 mole % Ce^{3+} leads to two-level ground state from the spin-orbit coupling (Bachmann, Ronda, & Meijerink, 2009; Mihokova et al., 2007).

The luminescence excitation and emission spectra of $Gd_2O_2SO_4$ nanoparticles containing 1.0 mole Eu^{3+} are presented in Figure 4.27. All the energy transitions of Eu^{3+} ions are clearly seen. Emission spectra show five emission bands in the 570-710nm spectral range. According to the energy level diagram and reference, the observed emission bands belong to the Eu^{3+} ion transitions of $^5D_0 \rightarrow {}^7F_J$ (J = 0, 1, 2,

3, 4). In addition, very weak emission bands related to $^5D_1 \rightarrow {}^7F_J$ (J = 0, 1, 2) transitions were observed in the spectral range of 520-560nm (Figure 4.27).

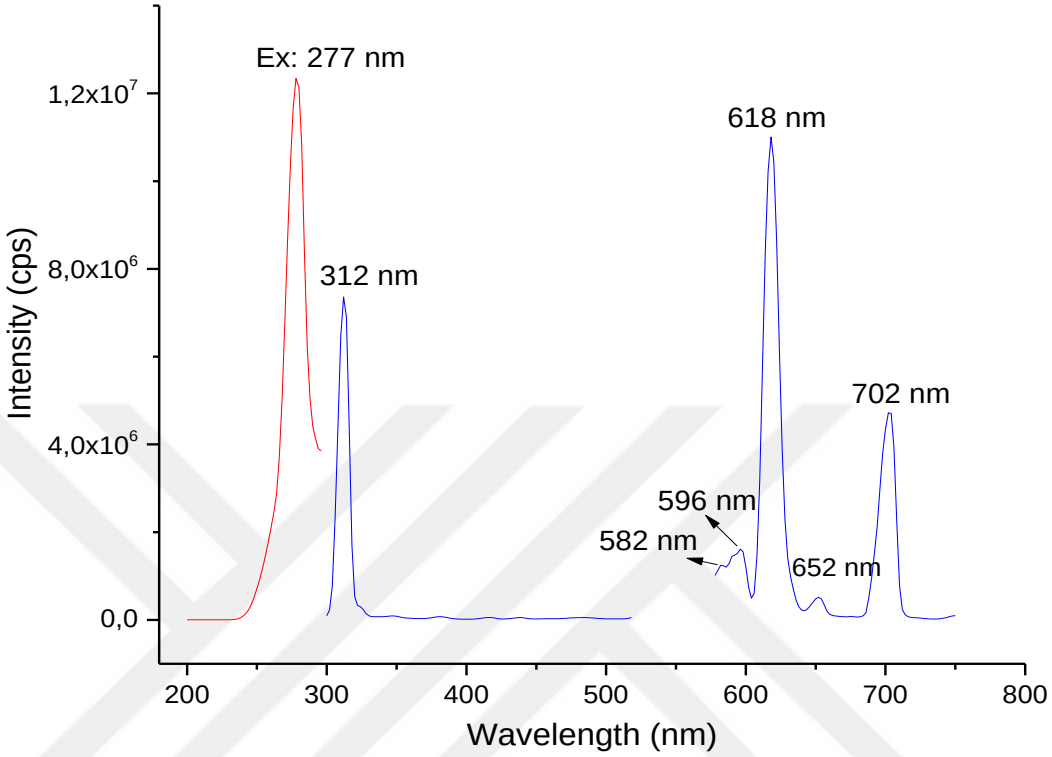

Figure 4.27 Excitation and emission spectra of the $Gd_2O_2SO_4$: Eu^{3+} doped nanoparticles

The emission observed at the $^5D_1$ level is very weak due to the strong non-radial deactivation of this energy level. Let us elaborate on the transition of Eu^{3+} ions from $^5D_0$ to ^7F_J (J = 0-4). The transition from $^5D_0$ to $^7F_0$ is prohibited because of the 0-0 ΔJ selection rule (De Sa et al., 2000). However, the $^5D_0 \rightarrow {}^7F_0$ transition is only observed for certain circumferences around Eu^{3+} centers. During J-mixing, the point is caused by the dependency between the symmetry group and the crystal field perturbation. The transition from $^5D_0$ to $^7F_0$ is also used to determine non-equivalent areas occupied by Eu^{3+} ions in a host. Observation of multiple peaks of the $^5D_0 \rightarrow {}^7F_0$ transition indicates the presence of more than one Eu^{3+} ion region in a compound. The transition from $^5D_0$ to $^7F_1$ belongs to the magnetic dipole transition. The density of a magnetic dipole transition is usually independent of the local environment of Eu^{3+} ions in the compounds. The transition from $^5D_0$ to $^7F_1$ is the most intensive transition in the spectrum of the inert with symmetry structure because when the Eu^{3+} occupies a

centrosymmetric field, the electric dipole transitions are very weak. The most intense $^5D_0 \rightarrow {}^7F_2$ transition observed belongs to the induced electric dipole transitions. This transition is also called hypersensitive transition because its density is much more sensitive to the local symmetry of the Eu^{3+} ion and the intrinsic nature of the ligands than the other electric dipole transitions. The density of the $^5D_0 \rightarrow {}^7F_2$ hypersensitive passage is generally used for the characterization of the asymmetry of areas occupied by Eu^{3+} centers (Huignard, Gacoin, & Boilot, 2000; Wakefield, Holland, Dobson, & Hutchison, 2001).

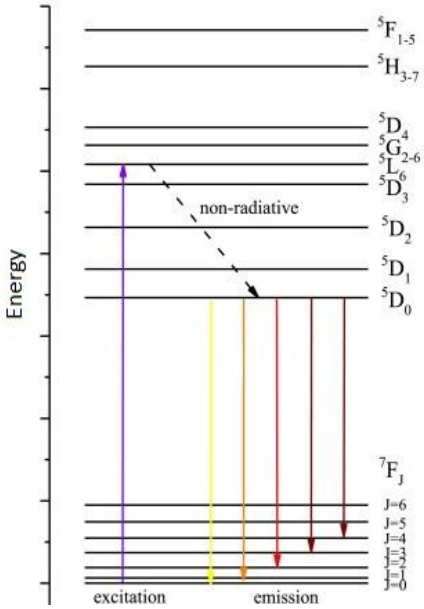

Figure 4.28 The partial energy diagram of Eu^{3+} ions in the $Gd_2O_2SO_4$ nanoparticles showing the luminescence mechanism

The transition from $^5D_0$ to $^7F_3$ is weak because it is prohibited by selection rules. This transition's existence is related to a strong J-mixing and a strong perturbation of the crystal field. The transition from $^5D_0$ to $^7F_4$ is allowed by the selection rules and belongs to the induced electric dipole transitions. Eu^{3+} ions are often used as a spectroscopic probe to study the local symmetry of Eu^{3+} centers in compounds. Eu^{3+} ions are preferred for different reasons. First, almost all Eu^{3+} doped compounds show a dense Eu^{3+} luminescence due to the large energy vacancy between the $^5D_0$ excited state and the $^7F_6$ highest level of ^7F. Second, the ground $^7F_0$ state and the excited $^5D_0$ state do not degenerate and are not divided by the crystal field. Third, transitions in the

luminescence spectra of Eu^{3+} ions are carried out at low J values (J = 0, 1, 2) up to ^7F_J states with $^5D_0$. This reason simplifies the interpretation of the Eu^{3+} spectra because the number of possible crystal field components is small and does not exceed (2J + 1) (*Rare Earth Nanotechnology*, 2012). As a result, in figure 4.28, the $^5D_0 \rightarrow {}^7F_0$ electronic transition appears at the emission wavelength of 582 nm. The $^5D_0 \rightarrow {}^7F_1$ electron transition is observed at 591 nm wavelength, the $^5D_0 \rightarrow {}^5F_2$ electron transition is 618 nm wavelength, the $^5D_0 \rightarrow {}^7F_3$ electron transition is 650 nm wavelength, and the $^5D_0 \rightarrow {}^7F_4$ electron transition is 700 nm wavelength, respectively.

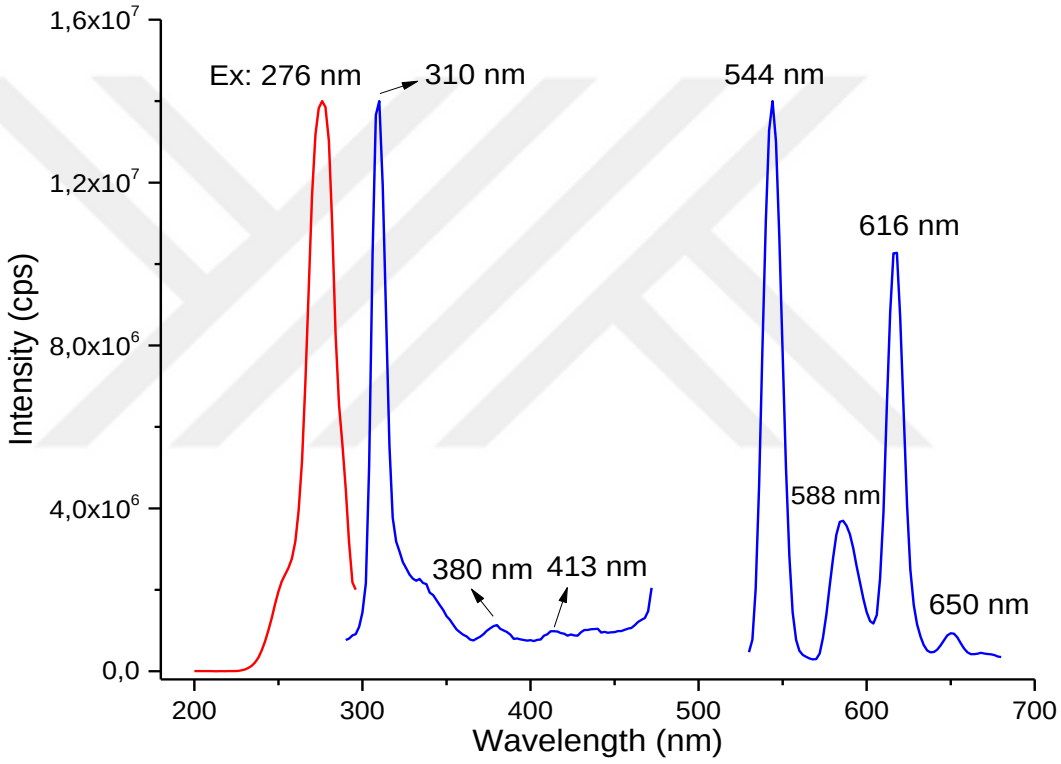

Figure 4.29 Excitation and emission spectra of the $Gd_2O_2SO_4$: Tb^{3+} doped nanoparticles

Figure 4.29 presents PL spectra of $Gd_2O_2SO_4$: $1.0Tb^{3+}$ nanoparticles under 276 nm excitation. Under 276 nm excitation, the emission spectra of Tb^{3+} ions are shown towards green emission in the regions of 380-460 and 544-650 nm. The energy transitions in these regions depend on $^5D_3 \rightarrow {}^7F_J$ (J = 6, 5, 4, 3) and $^5D_4 \rightarrow {}^7F_J$ (J = 5, 5, 4, 3. 2). It can be clearly seen that the excitation spectrum has a broad peak at the region of 276 nm and a series of peaks at 276 to 420 nm, which are related to host absorption and Tb^{3+} 4f-4f transitions.

Emission spectra have the densest green emission band at 544 nm, corresponding to the $^5D_4 \rightarrow {}^7F_5$ transition. Subsequently, the yellow emission band at 588 nm belongs to $^5D_4 \rightarrow {}^7F_4$, the yellow emission at 616 nm belongs to the $^5D_4 \rightarrow {}^7F_3$ transition, and the yellow emission at 650 nm belongs to the $^5D_4 \rightarrow {}^7F_2$ energy transition.

The blue emission spectra at 380 nm, 413 nm, and 440 nm belong to the energy transitions $^5D_3 \rightarrow {}^7F_J$ (J: 5, 4, 3), respectively. The blue emission peak at around 488 nm of the Tb^{3+} ion was not visible because it was associated with Raman scattering in our study. However, the $^5D_4 \rightarrow {}^7F_6$ energy transition of this blue emission has been repeatedly shown in the literature (K. Li et al., 2015; M. Xu, Wang, Jia, & Le, 2015; J. Zhou & Xia, 2015; Y. Zhou, Lin, Yu, Wang, & Zhang, 2002).

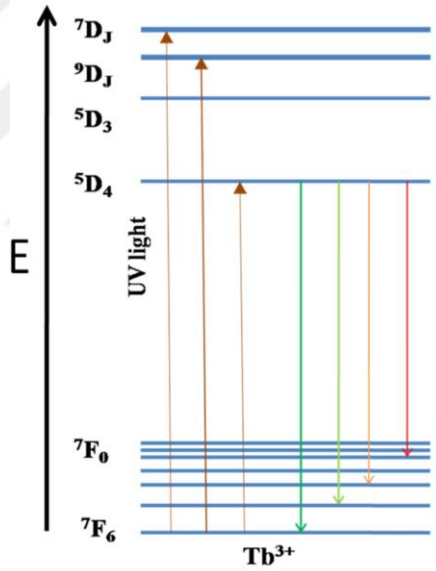

Figure 4.30 The partial energy diagram of Tb^{3+} ions in the $Gd_2O_2SO_4$ nanoparticles showing the luminescence mechanism

Figure 4.31 shows the $Gd_2O_2SO_4$: 1.0 Pr^{3+} excitation and emission spectra at room temperature. As shown in the picture, the excitation spectrum forms a dominant band at 277 nm. It contains an absorption band corresponding to the transitions from the ground state $^3H_4$ to excited levels belonging to the $^4f_2$ configuration of the Pr^{3+} ion. These transitions are easily assigned according to the selection rules. The weak

stimulation peak at 480 nm can be attributed to the $^3H_4 \rightarrow {}^3P_0$ transition. It is important to remember that crystal field separation is quite small for lanthanide ions and is less important than spin-orbit coupling compared to energy levels.

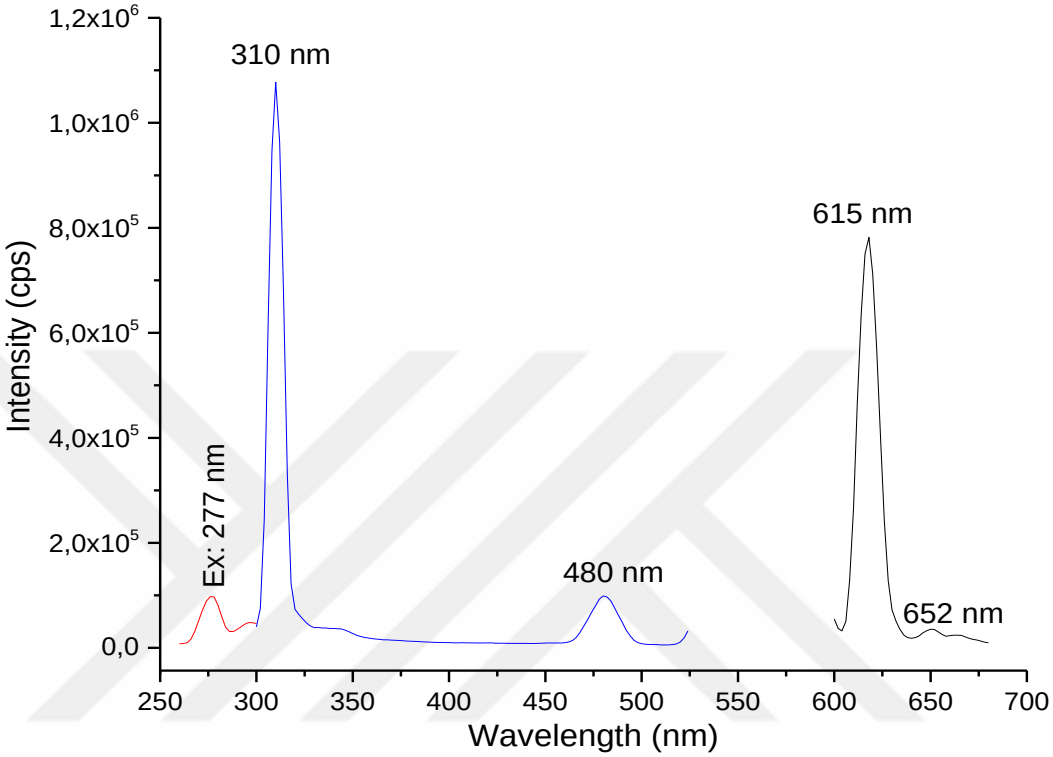

Figure 4.31 Excitation and emission spectra of the $Gd_2O_2SO_4$: Pr^{3+} doped nanoparticles

The Laporte rule prohibits electron transitions between orbitals. Moreover, due to the "buried" structure of f orbitals, bonding with molecular vibrations is weak. As a result, the spectra of the lanthanide ions are rather weak and the absorption bands are similar. The prominence of optical spectroscopy of rare earth ions (RE^{3+}) is principally associated with narrow emission bands originating from interstitial 4f-4f transitions and longevity, which make these ions unique among concave coordination compounds. The Laporte rule is slightly relaxed for these transitions due to the mixing of the counterpart electronic configurations produced by the strange compounds of the synthesis-free ligand domain. It has also been shown that ligand polarization effects are important for f-f transitions (Souamti, Martín, Zayani, Lozano-Gorrín, & Chehimi, 2017).

As we know, Pr^{3+} displays various lighting spectra in different host cages. In fact, the other passages are from $^3P_0 \rightarrow {}^3H_6$ (615 nm) and $^3P_0 \rightarrow {}^3F_2$ (644 nm). The most intense emission of the Pr^{3+} ion in the $Gd_2O_2SO_4$ matrix is the band at 615 nm corresponding to the $^3P_0 \rightarrow {}^3H_6$ transition. In the NIR region, this material has low-intensity emissions (Seferis et al., 2017).

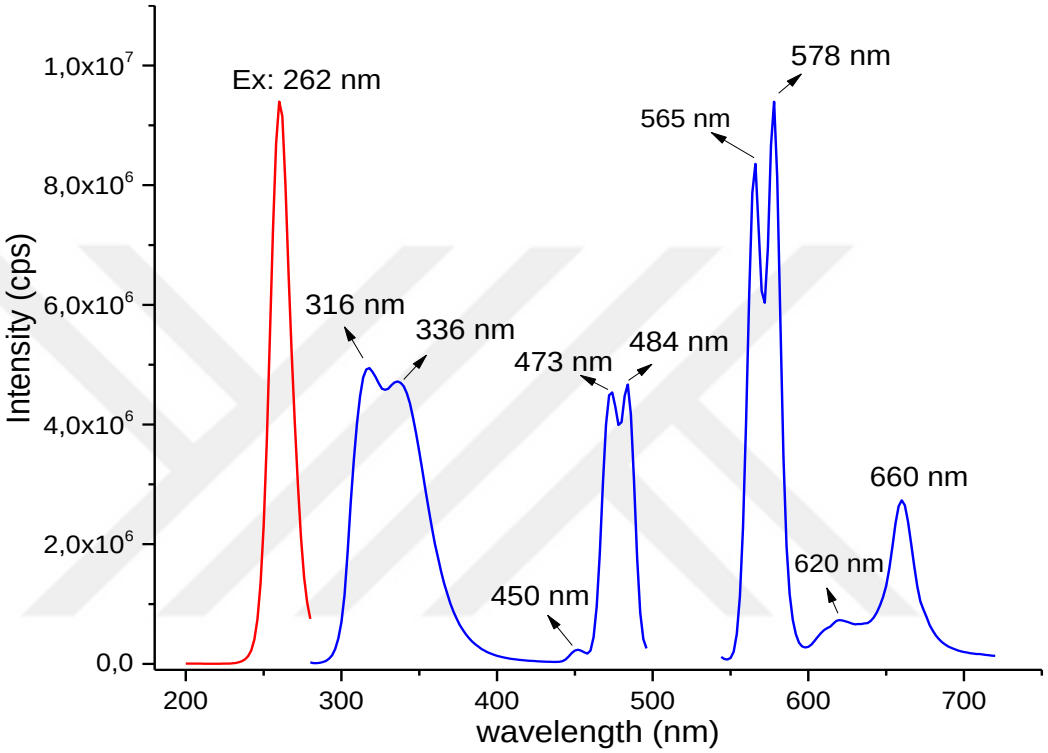

Figure 4.32 Excitation and emission spectra of the $Gd_2O_2SO_4$: Ho^{3+} doped nanoparticles

In Figure 4.32, emission peaks were observed at a wavelength range of 300 to 700 nm under UV light excitation at 262 nm. The emission bands formed around 316 nm are due to the $Gd_2O_2SO_4$ host structure. The emergence of these peaks in all structures activated with different rare earths reveals that the emission bands there are originated from the host structure. The blue emission spectra at 450 nm, 473 nm, and 484 nm are $^5G_6 \rightarrow {}^5I_8$ and $^5F_3 \rightarrow {}^5I_8$ energy transitions, respectively, of the Ho^{3+} element. The green emission peaks at 565 nm and 578 nm are attributed to the $^5F_4 \rightarrow {}^5I_8$ and $^5S_2 \rightarrow {}^5I_8$ energy transitions of the Ho^{3+} element. This shows energy transfer from the $Gd_2O_2SO_4$ host structure to Ho^{3+} ions. The UV light stimulates the electrons of the filled oxygen 2p levels in the valence band to the empty gadolinium 3d levels of the transmission band and relaxes the ground state by transferring the output state to the

energized holmium ions (Du et al., 2016; He et al., 2016; Krishnan & Thirumalai, 2014). Finally, the red emission band on the 660 nm band is attributed to the $^5F_5 \rightarrow {}^5I_8$ energy transition.

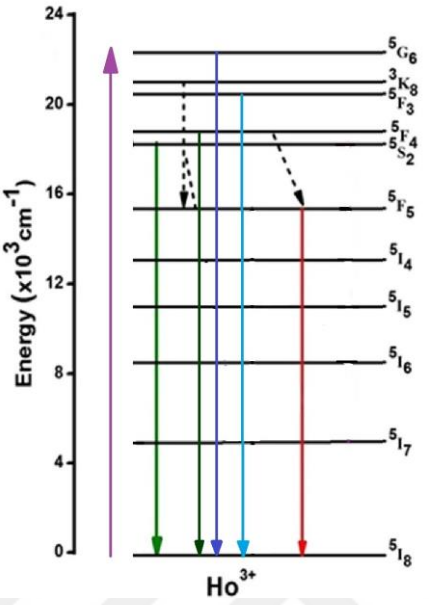

Figure 4.33 The partial energy diagram of Ho^{3+} ions in the $Gd_2O_2SO_4$ nanoparticles showing the luminescence mechanism

4.2.6.2 Decay Time Measurements of Nanoparticles

$Gd_2O_2SO_4$: RE nanoparticle phosphors were stimulated with a microsecond flash lamb at different wavelengths, as shown in Table 4.4. The decay curves of the phosphors were recorded at the maximum emission level for all. While the data obtained at around 300-400 nm is due to the transitions of the host and the synthesizer, the data obtained at other regions can be assigned to characteristic transitions of rare earth elements. The decay rate obtained at the maximum emission level for all phosphors was determined after the pulse excitation and according to the principle of the exponential formula, and the decay time was determined, that is, the time period for the intensity to fall to 1 / e from the initial value. As mentioned earlier the decay time of typical scintillation material can be as low as a few nanoseconds and as high as several milliseconds.

Table 4.4 Excitation and emission wavelength, and decay time measurement results of the nanophosphors with standard deviations and percentage distribution

Sample Name	λ_{max}^{ex}, λ_{max}^{em}	χ^2		**Decay Time (µs)**	**Standart Dev. (µs)**	**Rel %**
$Gd_2O_2SO_4$: Dy^{3+}	Ex: 276 nm Em: 575 nm	1.879	τ_1	72.99	0.40	19.06
			τ_2	231.03	2.81	19.18
			τ_3	715.36	0.93	61.76
$Gd_2O_2SO_4$: Ce^{3+}	Ex: 356 nm Em: 420 nm	1.237	τ_1	484.84	2.93	35.13
			τ_2	871.96	2.44	64.87
$Gd_2O_2SO_4$: Eu^{3+}	Ex: 277 nm Em: 618 nm	1.396	τ_1	337.10	2.36	13.36
			τ_2	1333.33	1.85	86.64
$Gd_2O_2SO_4$: Ho^{3+}	Ex: 262 nm Em: 578 nm	1.028	τ_1	2463.93	284.89	2.62
			τ_2	5250.39	68.85	97.38
$Gd_2O_2SO_4$: Tb^{3+}	Ex: 276 nm Em:544 nm	1.667	τ_1	281.62	0.35	24.12
			τ_2	1685.91	1.14	75.88
$Gd_2O_2SO_4$: Pr^{3+}	Ex: 277 nm Em: 615 nm	1.195	τ_1	35.80	0.83	10.9
			τ_2	261.58	5.02	32.05
			τ_3	1773.03	30.53	57.05

$$I(t) = Ae^{(-t/\tau 1)} + Be^{(-t/\tau 2)} + Ce^{(-t/\tau 3)}$$

In the given equation, "I" is the luminescence intensity, "A", "B" and "C" are the constants and "t" is the time. The curves can be determined by one or more decay time values. The exponent value for each material may be different. In the above equation, three different decay time values are used to determine the luminescence intensity.

Table 4.4 details the data on the time of decay of the studied structures. When emissions were monitored in the host and rare earth passages, phosphorus nanoparticles exhibited two or three exponential decay. The three exponential decay times observed in these nanoparticles can be attributed to the structural properties of the host matrix and the formation of different micro-environment for the rare earth additive.

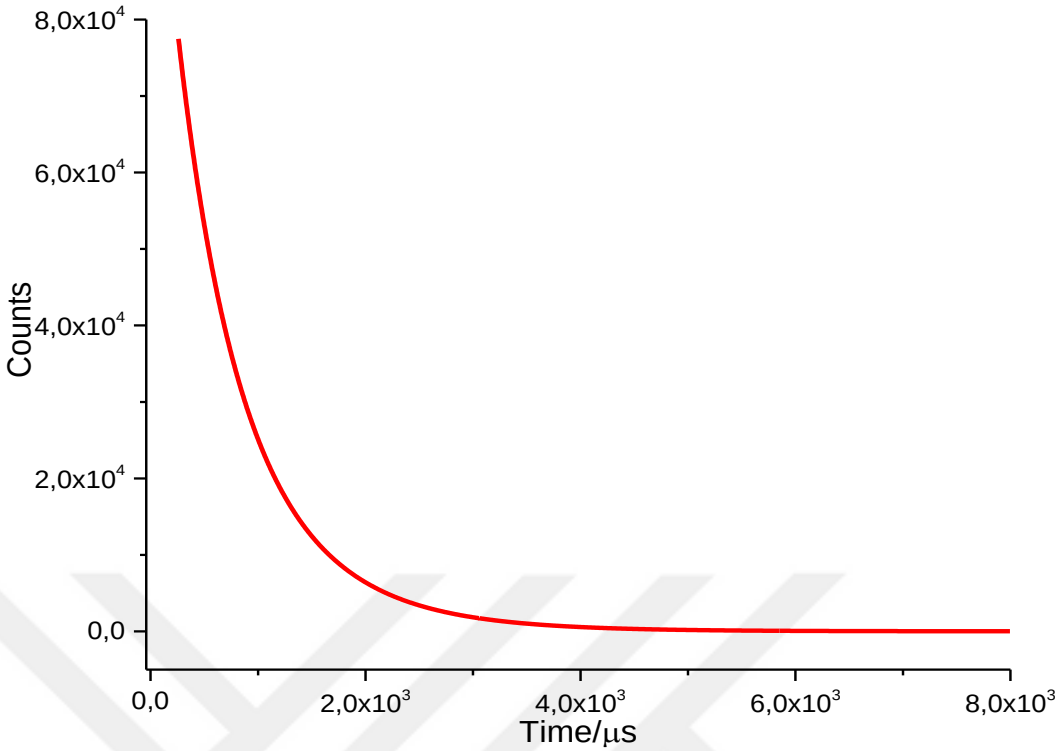

Figure 4.34 PL decay curves of the $Gd_2O_2SO_4$: Ce^{3+} nanoparticles

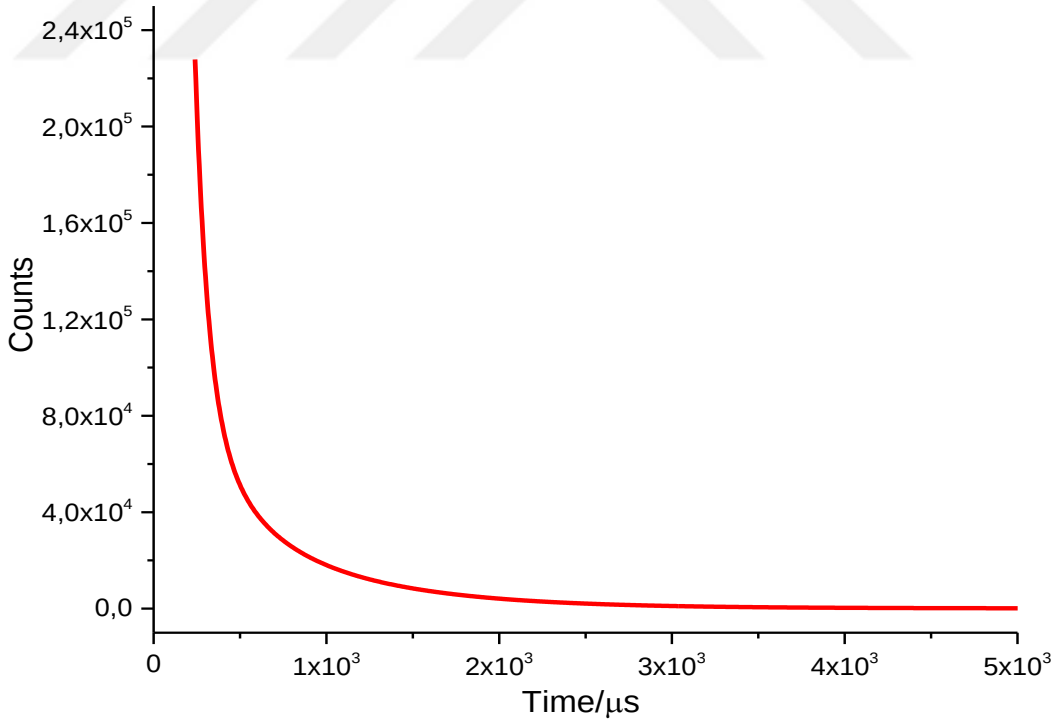

Figure 4.35 PL decay curves of the $Gd_2O_2SO_4$: Dy^{3+} nanoparticles

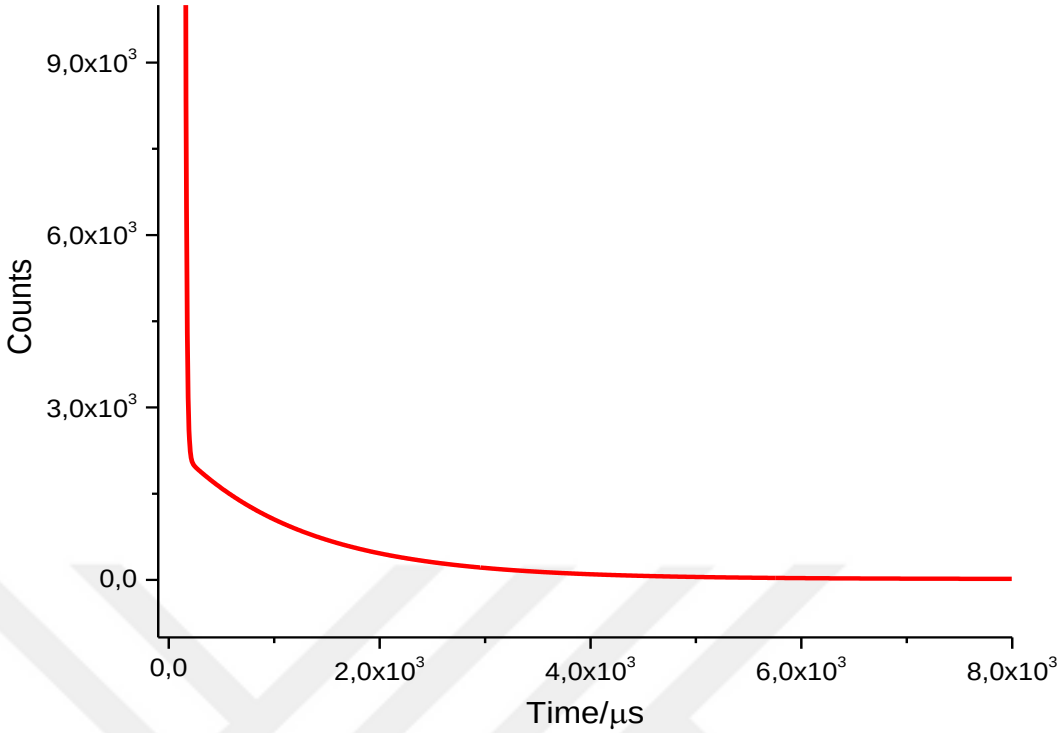

Figure 4.36 PL decay curves of the $Gd_2O_2SO_4$: Eu^{3+} nanoparticles

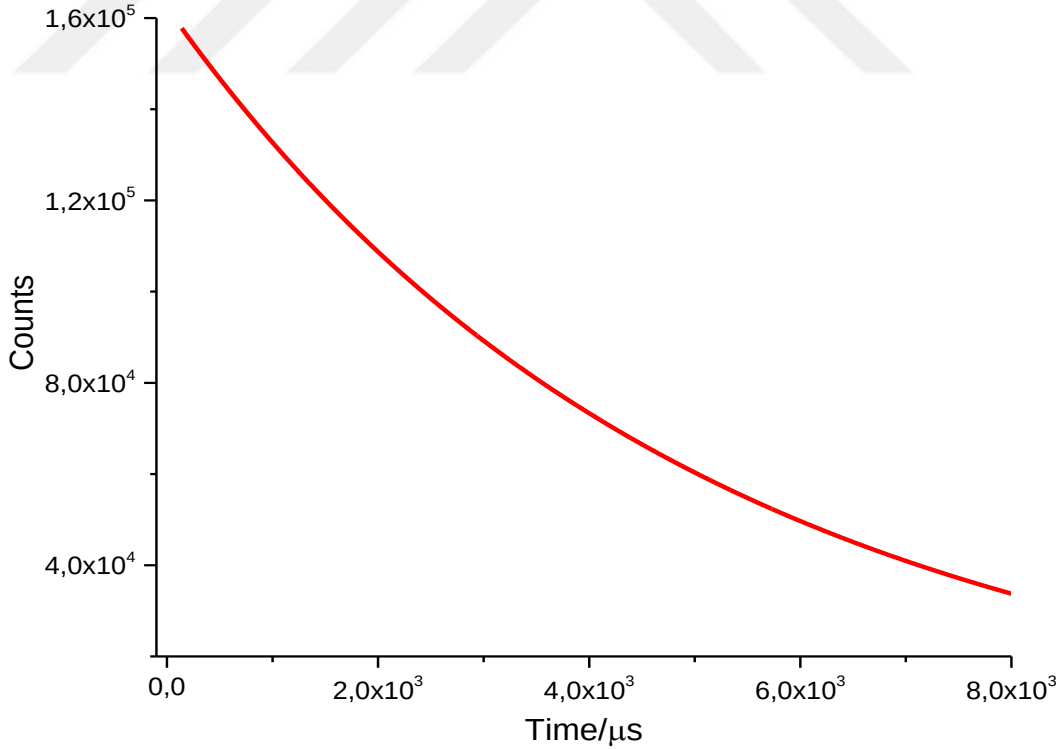

Figure 4.37 PL decay curves of the $Gd_2O_2SO_4$: Ho^{3+} nanoparticles

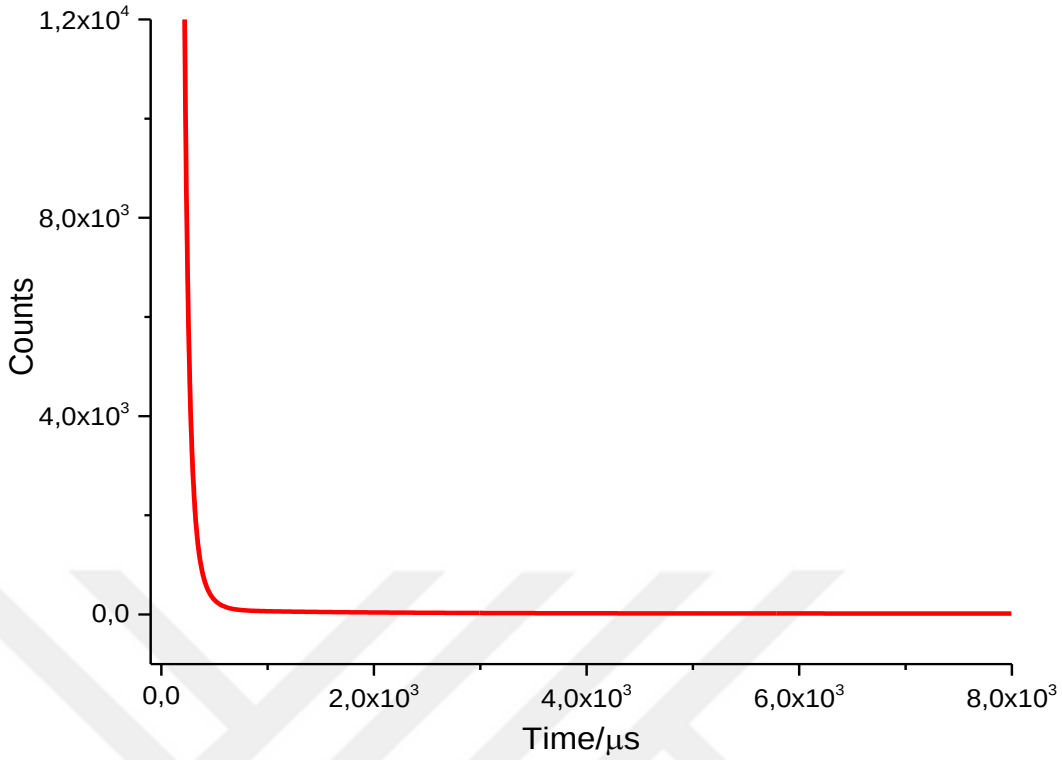

Figure 4.38 PL decay curves of the $Gd_2O_2SO_4$: Tb^{3+} nanoparticles

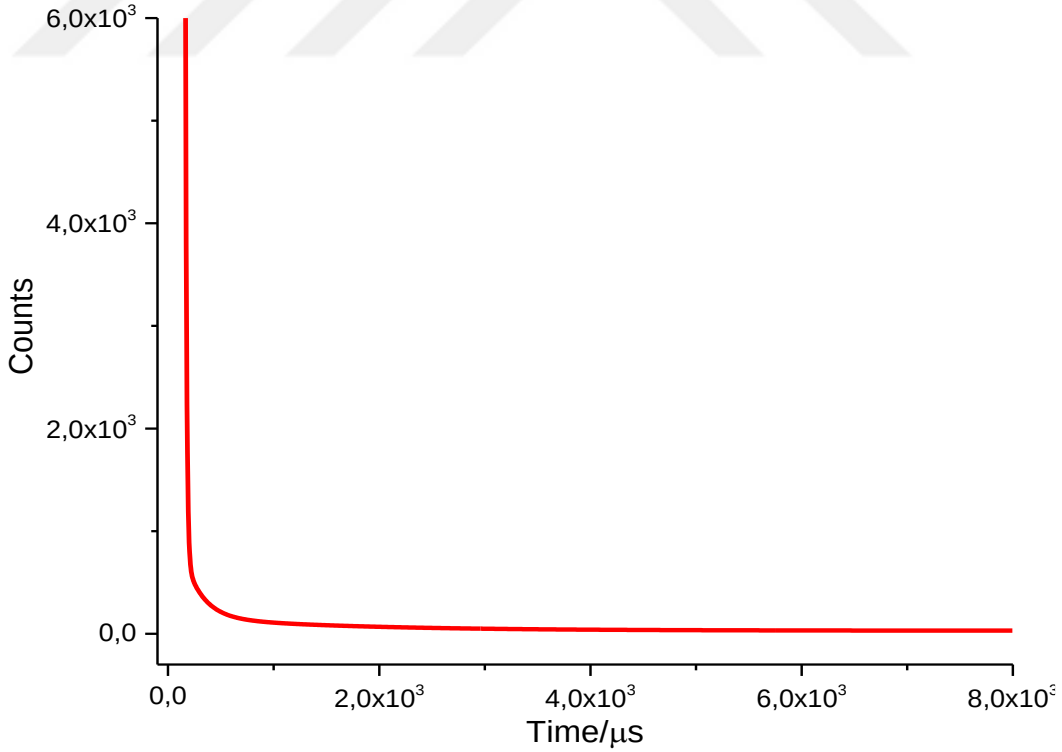

Figure 4.39 PL decay curves of the $Gd_2O_2SO_4$: Pr^{3+} nanoparticles

The presence of dopant ions in the host caused a decrease in decay times up to 1.0 % dopant concentration. When the spectral patterns of the decay time measurements and the results are evaluated together, it can be concluded that 1.0 % Dy^{3+} is more optimal (He et al., 2016).

In Figure 4.34, photoluminescence decay time curve of the $Gd_2O_2SO_4$: Ce^{3+} was investigated upon excitation at 340 nm. The emission data were acquired at 450 nm. The $Gd_2O_2SO_4$: Ce^{3+} exhibited two exponential decay times. The short and long lifetime components were 485 and 872 μs, respectively. Distribution of the short and long lifetime components was recorded as 35 and 65 %. The average decay time of the phosphor has been calculated as 735 μs.

In Figure 4.35, photoluminescence decay curve of the $Gd_2O_2SO_4$: Dy^{3+} was investigated upon excitation at 276 nm. The emission data were acquired at 575 nm. The $Gd_2O_2SO_4$: Dy^{3+} exhibited three exponential decay times. The short, mid and long lifetime components were 73, 231 and 715 μs, respectively. Distribution of the short, mid and long lifetime components were 19, 19, 62 %, respectively. The average decay time of the Dy^{3+} doped phosphor has been calculated as 501 μs.

The luminescence decay curves of the $Gd_2O_2SO_4$: Eu^{3+} nanoparticles are presented in Figure 4.36. The decay of the $^5D_0 \rightarrow {}^7F_2$ transition at 618 nm excited at 277 nm is measured. The decay time can be obtained by fitting a double exponential function. The short and long lifetime components were 337 (13.4%) and 1333 (86.6%) μs, respectively. The average decay time of the phosphor has been calculated as 1190 μs.

The decay times of $^5F_4$ and $^5F_5$ levels of $Gd_2O_2SO_4$: Ho^{3+} were measured under excitation at 262 nm. The decay curves are shown in Figure 4.37. The feeding of the energy level population occurs by direct energy transfer at higher energy levels than the groups of gadolinium, oxygen, and sulfate with the multi-phonon relaxation process. The fit curve is well equipped with a double exponential decay function. The short and long lifetime components were 2464 and 5250 μs, respectively. Distribution

of the short and long lifetime components was recorded as 2.6 and 97.4 %. The average decay time of the phosphor has been calculated as 5177 μs.

Figure 4.38 also shows the decay curves of Tb^{3+} ion emissions monitored at 544 nm in the representative $Gd_2O_2SO_4$: Tb^{3+} nanoparticles excited at 276 nm. The decay time can be obtained by fitting a double exponential function. The short and long lifetime components were 282 (24 %) and 1686 (76 %) μs, respectively. The average decay time of the phosphor has been calculated as 1349 μs.

Figure 4.39 shows, photoluminescence decay curve of the $Gd_2O_2SO_4$: Pr^{3+} was investigated upon excitation at 277 nm. The emission data were acquired at 615 nm. The $Gd_2O_2SO_4$: Pr^{3+} exhibited three exponential decay times. The short, mid and long lifetime components were 36, 262 and 1773 μs, respectively. Distribution of the short, mid and long lifetime components were 11, 32, 57 %, respectively. The average decay time of the Pr^{3+} doped phosphor has been calculated as 1097 μs.

The Dy^{3+}, Ce^{3+}, Eu^{3+}, Pr^{3+}, $Tb^{3+,}$ and Ho^{3+} doped forms exhibited average decay times of 501, 735, 1190, 1097, 1349 and 5177 μs, respectively. Among them, Dy^{3+} and Ce^{3+} doped forms can be concluded as more advantages over others due to the shorter decay times. However, all of the studied materials can be considered as potential scintillators. All of them satisfies requirements of scintillators both in terms of light conversion and decay time abilities.

CHAPTER FIVE
CONCLUSION

5.1 Conclusion

The $Gd_2O_2SO_4$: RE^{3+} orthogonal structures, Dy^{3+}, Eu^{3+}, Tb^{3+}, Ce^{3+}, $Pr^{3+,}$ and Ho^{3+} doped phosphor nanoparticles, which summarize the results of this thesis, have been successfully produced by the sol-gel method. In the synthesis method, the initial solution, gel state, and heat treated nanoparticles were separately characterized and the results were compared with the literature. The use of rare earth sulfates as scintillating material in the thesis is explained in detail. These detectors are used in digital imaging. The structure of the scintillator and the working mechanism are detailed. In addition, all the parameters that illustrate the efficiency of a scintillator are explained in detail. The luminescence mechanism that determines the properties of the scintillator has been described. The luminescence mechanism is explained by quantum mechanics approach. Potential application areas of $Gd_2O_2SO_4$ phosphor nanoparticles have been identified. In order to express and summarize the successful results obtained, it can be listed as follows:

1. Characteristic results (pH and turbidity) of solutions prepared by the sol-gel method to produce $Gd_2O_2SO_4$: 1.0%RE^{3+} phosphors have been investigated. The pH properties of $Gd_2O_2SO_4$ based solutions were measured before nanoparticles were formed. The results were determined in the range of 6.27 and 6.55. These results show that $Gd_2O_2SO_4$ based solutions initially exhibit basic character due to urea precursor. This is an important factor in terms of gelling time. Turbidity results of $Gd_2O_2SO_4$ based solutions were determined to be 5.0 ntu. The values of the other solutions were determined between 5 and 10 ntu. The reason for this increase is that the rare earth metal precursors used are colored and the color of the solutions changes. The obtained values compared to 1000 ntu indicate that the powder precursors in the solutions were completely dissolved. Upon examination of the already obtained solutions, a completely transparent appearance was obtained.

These results are extremely important in terms of both stoichiometric and physical properties of the nanoparticles.

2. As a result of the analyzes carried out, it was observed that the inclusion of additional elements did not cause a change in the FTIR results. For this reason, the FTIR results of pure $Gd_2O_2SO_4$ nanoparticles heat treated in solution, gel and at different temperatures were taken into account. FTIR analysis was performed to gain more insight into the structure and composition of the synthesized products. The spectrum shows the absorption peaks of physically absorbed water, crystal water, hydroxyl groups, carbonate groups, and a sulfate group, which indicates that the precursor is mostly composed of gadolinium hydroxyl, carbonate and sulfate groups with some crystal water. The broad SO_4^{2-} absorption bands split into some narrow peaks and the broad Gd\O bond peak also splits into two narrow peaks, indicating that the precursor has been gradually transformed into $Gd_2O_2SO_4$ phosphor. These results are consistent with those obtained by the DTA–TG.

3. DTA-TGA is an extremely important analysis to see the endothermic and exothermic reactions that occur with temperature increase in the material. The weight loss due to the increase in temperature is also determined by this analysis. In this context, all solutions were dried at 100 °C for several hours until gelation occurred and xerogels formed, and subsequently, DTA-TGA analysis was performed by heating up at the rate of 10 ºC/min at temperatures between 25 ºC and 950 ºC under dry air.

4. When XRD plots of nanoparticles activated with rare earth elements were examined, the orthorhombic phase structure of pure $Gd_2O_2SO_4$: RE^{3+} (JCPDS Card No. 029-0613) was detected. When doped elements with different ion diameters enter the structure, crystal cage shifts depending on the diameter of the dopant. This causes the XRD peaks in the different planes to decrease or increase. At the same time, there is a slight shift to the

right or left. The unit cell parameters of dopant-free $Gd_2O_2SO_4$; a = 12.996 Å, b = 8.117 Å, c = 4.184 Å and β = 96.58. The orthorhombic phase displays an efficient charge transfer process that ensures efficient luminescence emission. This phase is also used in phosphor screens.

5. XPS analysis was performed to determine the chemical composition and oxidation states of the nanoparticles. High-resolution elemental scans of $Gd_2O_2SO_4$ and $Gd_2O_2SO_4$: RE^{3+} nanoparticles were examined. The available elements, binding energies, and weights obtained as a result of the analyzes are detailed. Peak positions are consistent with the values reported in the literature. It has been observed that the peaks obtained in high-resolution elemental scans are in the same binding energy range for almost all nanoparticles. These peaks are detailed in the XPS results of all rare earth activated phosphors. In results, it is clear that doped elements Dy^{3+}, Ce^{3+}, Eu^{3+}, Ho^{3+}, $Tb^{3+,}$ and Pr^{3+} are in the structure of $Gd_2O_2SO_4$ phosphors. High-resolution elemental scans have not been reexamined because the binding energies of these phosphorus elements are almost identical to the binding energies.

6. Surface morphology, composition, and topography are important factors for nanoparticles. In principle, these factors strongly influence surface quality. Regarding this, SEM images of $Gd_2O_2SO_4$ nanoparticles activated with rare earth have been examined and their results discussed. Numerous small nuclei were formed in the sol-gel system, and the growth of the nucleus leads to the formation of nanoparticles due to the high anisotropic crystal structure nature. Most of the nanoparticles tend to aggregate into an orthorhombic structure during the course of the reaction, in order to reduce the surface energy. The sol-gel synthesis was involved dissolution-recrystallization and further growth processes.

7. Photoluminescence spectra were tested at room temperature for all samples to investigate the luminescence properties of $Gd_2O_2SO_4$ phosphors doped

with rare earth elements. Firstly, PL emission spectra of $Gd_2O_2SO_4$: Dy^{3+} was investigated due to Dy^{3+} nanoparticles concentration. Three different Dy^{3+} concentrations were studied, 0.5, 1.0 and 2.0 %, respectively. The ideal luminescence intensity values were obtained at 1.0% Dy^{3+} concentration. For this reason, only 1.0 percent concentration of the other $Gd_2O_2SO_4$: RE^{3+} (RE^{3+}: Eu^{3+}, Ce^{3+}, Ho^{3+}, Tb^{3+}, Pr^{3+}) have been studied. The results are compared with the literature and interpreted in detail in the thesis. When the amount of this critical concentration is exceeded, "concentration quenching" occurs in the material. This quench results from an increase in the ion-ion interaction triggered by the shorter distance between the interacting activators as the concentration increases. In addition, in the photoluminescence graphs of $Gd_2O_2SO_4$ nanoparticles activated with all rare earth, the peaks observed at about 310 nm are attributed to the transition of the gadolinium element. For this reason, it is seen in all emission results.

8. $Gd_2O_2SO_4$: RE^{3+} nanoparticle phosphors were stimulated with a microsecond flash lamb at different wavelengths. The decay curves of the phosphors were recorded at the maximum emission wavelength for all. While the emission data obtained at around 300-400 nm is due to the transitions of the host and the synthesizer, the data obtained at other regions can be assigned to characteristic transitions of rare earth elements. The decay time was determined after the excitation and calculated according to the principle of the exponential formula, that is, the time period for the intensity to fall to 1 / e from the initial value. The decay curves and values of all $Gd_2O_2SO_4$: RE^{3+} phosphor nanoparticles are compared with the literature and interpreted in detail in the thesis. The presence of dopant ions in the host caused a decrease in decay times up to 1.0 % Dy.

REFERENCES

Ahmed, S. N. (2007). *Physics and engineering of radiation detection*. Academic Press.

Aizawa, H., Katsumata, T., Takahashi, J., Matsunaga, K., Komuro, S., Morikawa, T., & Toba, E. (2003). Long afterglow phosphorescent sensor materials for fiber-optic thermometer. *Review of Scientific Instruments, 74*(3), 1344–1349.

Amelio, G. F. (1974). Charge-coupled devices. *Scientific American, 230*(2), 22–31.

Aritman, I., Yildirim, S., Ebeoglugil, M. F., Yurddaskal, M., Ertekin, K., & Celik, E. (2017). Sol–gel synthesis, characterization, and photoluminescence properties of sub-micron $Gd_2O_2SO_4$ powders. *Journal of the Australian Ceramic Society, 53*(2), 457–463.

Aritman, I., Yildirim, S., Kisa, A., Guleryuz, L. F., Yurddaskal, M., Dikici, T., & Celik, E. (2017a). Fabrication and characterization of $Gd_2O_2SO_4:Tb^{3+}$ phosphors by sol-gel method. In *AIP Conference Proceedings* (*1809*, 20003). AIP Publishing.

Aritman, I., Yildirim, S., Kisa, A., Guleryuz, L. F., Yurddaskal, M., Dikici, T., & Celik, E. (2017b). Production and characterization of magnetic and luminescent $Gd_2O_2SO_4:Eu^{3+}$ nanoparticles by sol-gel technique. In *AIP Conference Proceedings* (*1809*, 20004). AIP Publishing.

Aritman, I., Yildirim, S., Kisa, A., Guleryuz, L. F., Yurddaskal, M., Dikici, T., & Celik, E. (2017c). Synthesis and Characterization of $Gd_2O_2SO_4:Pr^{3+}$ Scintillation Material Produced by Sol-Gel Process for Digital Imaging System. *Acta Physica Polonica, A., 131*(1).

Baccaro, S., Cemmi, A., Di Sarcina, I., Esposito, B., Ferrara, G., Grossi, A., Quintieri, L. (2018). Radiation damage tests on diamond and scintillation detector components for the ITER Radial Neutron Camera. *IEEE Transactions on Nuclear Science*.

Bachmann, V., Ronda, C., & Meijerink, A. (2009). Temperature quenching of yellow

Ce3+ luminescence in YAG: Ce. *Chemistry of Materials*, *21*(10), 2077–2084.

Bai, G., Tsang, M., & Hao, J. (2015). Tuning the luminescence of phosphors: beyond conventional chemical method. *Advanced Optical Materials*, *3*(4), 431–462.

Barlett, & Jones. (2010). Scintillation detectors. *Journal of Nuclear Medicine Technology*, *38*(3), 17–27.

Birks, J. B. (2013). *The Theory and Practice of Scintillation Counting: International Series of Monographs in Electronics and Instrumentation* (*27*). Elsevier.

Bode, P. (2009). Detectors of Radiation. *Physical Methods, Instruments and Measurements*, *II*, 1–57.

Borgatti, F., Berger, J. A., Céolin, D., Zhou, J. S., Kas, J. J., Guzzo, M., Regoutz, A. (2018). Revisiting the origin of satellites in core-level photoemission of transparent conducting oxides: The case of n-doped SnO_2. *Physical Review B*, *97*(15), 155102.

Brinker, C. J., & Scherer, G. W. (2013). *Sol-gel science: the physics and chemistry of sol-gel processing*. Academic press.

Brooks, F. D. (1979). Development of organic scintillators. *Nuclear Instruments and Methods*, *162*(1–3), 477–505.

Chen, G., Chen, F., Liu, X., Ma, W., Luo, H., Li, J., Qiu, G. (2014). Hollow spherical rare-earth-doped yttrium oxysulfate: A novel structure for upconversion. *Nano Research*, *7*(8), 1093–1102.

Chen, Y., Hu, Z., & Lang, J. C. (1998). Turbidity investigation of the sol–gel transition in carrageenan gels under physiologic conditions. *Journal of Applied Polymer Science*, *68*(1), 29–35.

Chopra, D., Babb, H., & Bhalla, R. (1976). Appearance-potential study of the 4f states of holmium. *Physical Review B*, *14*(12), 5231.

Davisson, C. M. (1965). Interaction of γ-radiation with matter. In *Alpha-, beta-and gamma-ray spectroscopy* (37–78). Elsevier.

De Sa, G. F., Malta, O. L., de Mello Donegá, C., Simas, A. M., Longo, R. L., Santa-Cruz, P. A., & da Silva Jr, E. F. (2000). Spectroscopic properties and design of highly luminescent lanthanide coordination complexes. *Coordination Chemistry Reviews*, *196*(1), 165–195.

Du, S., Wang, D., Qiang, Q., Ma, X., Tang, Z., & Wang, Y. (2016). The dual-model up/down-conversion green luminescence of $Gd_6O_5F_8$:Yb^{3+}, Ho^{3+}, Li^{+} and its application for temperature sensing. *Journal of Materials Chemistry C*, *4*(29), 7148–7155.

Dutta, S., Som, S., & Sharma, S. K. (2015). Excitation spectra and luminescence decay analysis of K^{+} compensated Dy^{3+} doped $CaMoO_4$ phosphors. *RSC Advances*, *5*(10), 7380–7387.

Ebeoglugil, M. F. (2011). Processing, characterization and development of rare earth doped lead magnesium niobate ferroelectric ceramic capacitors by sol-gel technique. DEÜ Fen Bilimleri Enstitüsü.

Eidelman, S. I., & Shwartz, B. A. (2012). Interactions of particles and radiation with matter. In *Handbook of Particle Detection and Imaging* (3–23). Springer.

Electromagnetic spectrum. (n.d.). Retrieved May 18, 2018, from https://www.britannica.com/science/electromagnetic-spectrum

Engel, K. J., & Herrmann, C. (2015, April 28). Direct conversion X-ray detector.

Ergler, T., Freund, A., Kreisler, B., Schröter, C., & Wirth, S. (2016, July 19). Direct conversion x-ray detector.

FTIR analysis. (n.d.). Retrieved May 22, 2018, from http://www.machinery lubrication.com/Read/30205/ftir-oil-analysis

Gai, S., Li, C., Yang, P., & Lin, J. (2013). Recent progress in rare earth micro/nanocrystals: soft chemical synthesis, luminescent properties, and biomedical applications. *Chemical Reviews*, *114*(4), 2343–2389.

Gaisford, S., Kett, V., & Haines, P. (2016). *Principles of thermal analysis and calorimetry*. Royal society of chemistry.

Garcıa-Murillo, A., Le Luyer, C., Garapon, C., Dujardin, C., Bernstein, E., Pedrini, C., & Mugnier, J. (2002). Optical properties of europium-doped Gd_2O_3 waveguiding thin films prepared by the sol–gel method. *Optical Materials*, *19*(1), 161–168.

Gektin, A. V, Belsky, A. N., & Vasil'ev, A. N. (2014). Scintillation efficiency improvement by mixed crystal use. *IEEE Transactions on Nuclear Science*, *61*(1), 262–270.

Guo, H., Yang, X., Xiao, T., Zhang, W., Lou, L., & Mugnier, J. (2004). Structure and optical properties of sol–gel derived Gd_2O_3 waveguide films. *Applied Surface Science*, *230*(1–4), 215–221.

Haynes, J. W., & Brown, J. J. (1968). Preparation and luminescence of selected Eu^{3+}-activated rare earth-oxygen-sulfur compounds. *Journal of The Electrochemical Society*, *115*(10), 1060–1066.

He, F., Feng, L., Yang, P., Liu, B., Gai, S., Yang, G., Lin, J. (2016). Enhanced up/down-conversion luminescence and heat: Simultaneously achieving in one single core-shell structure for multimodal imaging guided therapy. *Biomaterials*, *105*, 77–88.

Hench, L. L., & West, J. K. (1990). The sol-gel process. *Chemical Reviews*, *90*(1), 33–72.

Herrmann, J., Spratte, W., & Schneider, G. M. (2017). Differential Thermal Analysis (DTA). In *Molecular and Chemical Physics, Chemistry, Biological Effects, Geo and Planetary Sciences, New Resources, Dynamic Pressures, High Pressure Safety: Proceedings of the VIIth International AIRAPT Conference (Organised Jointly with the EHPRG), Le Creusot, Fra* (673). Elsevier.

Hine, G. J. (2016). *Instrumentation in nuclear medicine*. Academic Press.

Hoheisel, M., Arques, M., Chabbal, J., Chaussat, C., Ducourant, T., Hahm, G., Spahn,

M. (1998). Amorphous silicon X-ray detectors. *Journal of Non-Crystalline Solids*, *227*, 1300–1305.

Holl, I., Lorenz, E., & Mageras, G. (1988). A measurement of the light yield of common inorganic scintillators. *IEEE Transactions on Nuclear Science*, *35*(1), 105–109.

Huang, X.-Z., Liu, Z., Yang, Y., & Tian, Y. (2013). Molten Salt Synthesis of $La_2O_2SO_4$ Nanosheets and Their Luminescent Properties with Eu^{3+} Doping. *Functional Materials Letters*, *6*(02), 1350019.

Huignard, A., Gacoin, T., & Boilot, J.-P. (2000). Synthesis and luminescence properties of colloidal YVO_4: Eu phosphors. *Chemistry of Materials*, *12*(4), 1090–1094.

Ikeue, K., Kawano, T., Eto, M., Zhang, D., & Machida, M. (2008). X-ray structural study on the different redox behavior of La and Pr oxysulfates/oxysulfides. *Journal of Alloys and Compounds*, *451*(1–2), 338–340.

Janesick, J. R. (2001). *Scientific charge-coupled devices* (*83*). SPIE press.

Jian, X., Wang, H., Lee, M. H., Tian, W., Chen, G. Z., Chen, W. Q., Yin, L. J. (2017). Insight the luminescence properties of AlON: Eu, Mg Phosphor under VUV excitation. *Materials*, *10*(7), 1–9.

Joens, J. A. (2015). Fluorescence and phosphorescence. *Salem Press Encyclopedia of Science*, 1–12. Retrieved from http://search.ebscohost.com/login.aspx?direct=true&db=ers&AN=89317011&authtype=sso&custid=s8993828&site=edslive&scope=site

Johann Zmeskal. (2015). Detector and detector systems for particle and nuclear physics I. Retrieved from https://www.oeaw.ac.at/fileadmin/subsites/etc/Institute/SMI/PDF/Detectors_WS2014-15_A2.pdf

Kang, H. R. (1997). *Color technology for electronic imaging devices*. SPIE press.

Kasap, S. O., & Rowlands, J. A. (2002). Direct-conversion flat-panel X-ray image sensors for digital radiography. *Proceedings of the IEEE*, *90*(4), 591–604.

Kent, A. D. (n.d.). X-ray Lab : Bragg Diffraction, 1–11.

Kijima, T., Isayama, T., Sekita, M., Uota, M., & Sakai, G. (2009). Emission properties of Tb^{3+} in $Y_2O_2SO_4$ derived from their precursory dodecylsulfate-templated concentric-and straight-layered nanostructures. *Journal of Alloys and Compounds*, *485*(1–2), 730–733.

Kijima, T., Shinbori, T., Sekita, M., Uota, M., & Sakai, G. (2008). Abnormally enhanced Eu3+ emission in $Y_2O_2SO_4$: Eu^{3+} inherited from their precursory dodecylsulfate-templated concentric-layered nanostructure. *Journal of Luminescence*, *128*(3), 311–316.

Kim, S., Masui, T., & Imanaka, N. (2009). Synthesis of red-emitting phosphors based on gadolinium oxysulfate by a flux method. *Electrochemistry*, *77*(8), 611–613.

Kinekawa, Y., & Kitabatake, N. (1995). Turbidity and Rheological Properties of Gels and Sols Prepared by Heating Process Whey Protein. *Bioscience, Biotechnology, and Biochemistry*, *59*(5), 834–840.

Knoll, G. F. (1972). Chapter 8: Scintillation Detector Principles. *Radiation Detection and Measurement*, 163–164.

Knoll, G. F. (2000). Radiation detection and measurement Glenn F. *Knoll, 3rd Ed.(J. Wiley, New York, 2000)*.

Krishnan, R., & Thirumalai, J. (2014). Up/down conversion luminescence properties of $(Na0.5Gd0.5)MoO_4:Ln^{3+}$ (Ln= Eu, Tb, Dy, Yb/Er, Yb/Tm, and Yb/Ho) microstructures: synthesis, morphology, structural and magnetic investigation. *New Journal of Chemistry*, *38*(8), 3480–3491.

Lakowicz, J. R. (1983). Quenching of fluorescence. In *Principles of fluorescence spectroscopy* (257–301). Springer.

Lecoq, P., Gektin, A., & Korzhik, M. (2016). *Inorganic scintillators for detector systems: physical principles and crystal engineering*. Springer.

Lecoq, P., Gektin, A., & Korzhik, M. (2017). Scintillation and Inorganic Scintillators. In *Inorganic Scintillators for Detector Systems* (1–41). Springer.

Lee, S. W., Jeong, J., Ra, C. S., & Sohn, Y. (2017). Hydrothermal Synthesis and Characterization of $Sm_2O_2SO_4$ Nanoplates. *Bulletin of the Korean Chemical Society*, *38*(10), 1149–1154.

Leroy, C., & Rancoita, P.-G. (2011). *Principles of radiation interaction in matter and detection*. World Scientific.

Lewis, G. N., & Kasha, M. (1944). Phosphorescence and the triplet state. *Journal of the American Chemical Society*, *66*(12), 2100–2116.

Li, G., Geng, D., Shang, M., Zhang, Y., Peng, C., Cheng, Z., & Lin, J. (2011). Color tuning luminescence of $Ce^{3+}/Mn^{2+}/Tb^{3+}$-triactivated $Mg_2Y_8(SiO_4)_6O_2$ via energy transfer: potential single-phase white-light-emitting phosphors. *The Journal of Physical Chemistry C*, *115*(44), 21882–21892.

Li, J.-G., Li, X., Sun, X., & Ishigaki, T. (2008). Monodispersed colloidal spheres for uniform $Y_2O_3:Eu^{3+}$ red-phosphor particles and greatly enhanced luminescence by simultaneous Gd3+ doping. *The Journal of Physical Chemistry C*, *112*(31), 11707–11716.

Li, K., Zhang, Y., Li, X., Shang, M., Lian, H., & Lin, J. (2015). Host-sensitized luminescence in $LaNbO_4:Ln^{3+}$ (Ln^{3+}= $Eu^{3+}/Tb^{3+}/Dy^{3+}$) with different emission colors. *Physical Chemistry Chemical Physics*, *17*(6), 4283–4292.

Lian, J. B., Wang, W. G., Wang, B. X., & Li, J. (2011). Photoluminescence of (Gd1-x, Dyx) $_2O_2SO_4$ phosphors synthesized by homogeneous precipitation method. In *Advanced Materials Research* (*299*, 612–615). Trans Tech Publ.

Lian, J., Liu, F., Wang, X., & Sun, X. (2014). Hydrothermal synthesis and photoluminescence properties of $Gd_2O_2SO_4:Eu^{3+}$ spherical phosphor. *Powder*

Technology, *253*, 187–192.

Light As Electromagnetic Radiation. (n.d.). Retrieved from https://www.britannica.com/science/light/Light-as-electromagnetic-radiation#ref929159

Liu, F., Wang, X., Yang, Y., Zhang, J., Zhang, Z., & Lian, J. (2016). Hydrothermal synthesis combined with calcination of $Gd_2O_2SO_4$:Yb^{3+}, Er^{3+} nanoparticles and their up-conversion luminescence. *J Ceram Process Res*, *17*, 1287–1291.

Liu, X., Zhang, D., Jiang, J., Zhang, N., Ma, R., Zeng, H., Qiu, G. (2012). General synthetic strategy for high-yield and uniform rare-earth oxysulfate ($RE_2O_2SO_4$, RE= La, Pr, Nd, Sm, Eu, Gd, Tb, Dy, Y, Ho, and Yb) hollow spheres. *RSC Advances*, *2*(25), 9362–9365.

Machida, M., Kawamura, K., Ito, K., & Ikeue, K. (2005). Large-capacity oxygen storage by lanthanide oxysulfate/oxysulfide systems. *Chemistry of Materials*, *17*(6), 1487–1492.

Machida, M., Kawano, T., Eto, M., Zhang, D., & Ikeue, K. (2007). Ln dependence of the large-capacity oxygen storage/release property of Ln oxysulfate/oxysulfide systems. *Chemistry of Materials*, *19*(4), 954–960.

Magnuson, M., Schmidt, S., Hultman, L., & Högberg, H. (2017). Electronic properties and bonding in ZrHx thin films investigated by valence-band x-ray photoelectron spectroscopy. *Physical Review B*, *96*(19), 195103.

Manigandan, R., Giribabu, K., Suresh, R., Munusamy, S., Muthamizh, S., Dhanasekaran, T., Narayanan, V. (2015). Synthesis, growth and photoluminescence behaviour of $Gd_2O_2SO_4$: Eu^{3+} nanophosphors: the effect of temperature on the structural, morphological and optical properties. *RSC Advances*, *5*(10), 7515–7521.

Martin, T., Koch, A., & Nikl, M. (2017). Scintillator materials for x-ray detectors and beam monitors. *MRS Bulletin*, *42*(6), 451–457.

McGregor, D. S. (2017). Materials for Gamma-Ray Spectrometers: Inorganic

Scintillators. *Annual Review of Materials Research*, (0).

Methodology, R. (2018). Chapter 3 Gas Filled Detectors, 1–16. Retrieved from https://www.science.mcmaster.ca/medphys/images/files/courses/4R06/4R6Notes3_GasFilled_Detectors.pdf

Meyer, S., Dudy, L., Schäfer, J., Blumenstein, C., Höpfner, P., Umbach, T. E., Claessen, R. (2014). Valence band and core-level photoemission of Au/Ge (001): Band mapping and bonding sites. *Physical Review B*, *90*(12), 125409.

Mihokova, E., Nikl, M., Mareš, J. A., Beitlerova, A., Vedda, A., Nejezchleb, K., D'Ambrosio, C. (2007). Luminescence and scintillation properties of YAG: Ce single crystal and optical ceramics. *Journal of Luminescence*, *126*(1), 77–80.

Nathans, M. W., & Wendlandt, W. W. (1962). The thermal decomposition of the rare-earth sulphates: Thermogravimetric and differential thermal analysis studies up to 1400 C. *Journal of Inorganic and Nuclear Chemistry*, *24*(7), 869–879.

Nguyen, H. T., Rougieux, F. E., Mitchell, B., & Macdonald, D. (2014). Temperature dependence of the band-band absorption coefficient in crystalline silicon from photoluminescence. *Journal of Applied Physics*, *115*(4), 43710.

Osseni, S. A., Denisenko, Y. G., Fatombi, J. K., Sal'nikova, E. I., & Andreev, O. V. (2017). Synthesis and characterization of $Ln_2O_2SO_4$ (Ln= Gd, Ho, Dy and Lu) nanoparticles obtained by coprecipitation method and study of their reduction reaction under H_2 flow. *Journal of Nanostructure in Chemistry*, *7*(4), 337–343.

Pedrini, C. (2005). Scintillation mechanisms and limiting factors on each step of relaxation of electronic excitations. *Physics of the Solid State*, *47*(8), 1406–1411.

Pierre, A. C. (2013). *Introduction to sol-gel processing* (*1*). Springer Science & Business Media.

Porcher, P., Svoronos, D. R., Leskelä, M., & Hölsä, J. (1983). Preparation and optical properties of europium-activated rare earth oxysulfates. *Journal of Solid State Chemistry*, *46*(1), 101–111.

Quora. (n.d.). Retrieved May 21, 2018, from https://www.quora.com/What-is-the-Jablonski-diagram

Rani, S., Suri, P., Shishodia, P. K., & Mehra, R. M. (2008). Synthesis of nanocrystalline ZnO powder via sol–gel route for dye-sensitized solar cells. *Solar Energy Materials and Solar Cells*, *92*(12), 1639–1645.

Yang, T. T. T. (Ed.). (2012). *Rare earth nanotechnology*. CRC Press.

Rodnyi, P. A. (1997). *Physical processes in inorganic scintillators* (*14*). CRC press.

Rodrigues, R. V, Marciniak, L., Khan, L. U., Matos, J. R., Brito, H. F., & Stręk, W. (2016). Luminescence investigation of $D_{y2}O_2S$ and $Dy_2O_2SO_4$ obtained by thermal decomposition of sulfate hydrate. *Journal of Rare Earths*, *34*(8), 814–819.

Saha, G. B. (2012). *Physics and radiobiology of nuclear medicine*. Springer Science & Business Media.

Scanning Electron Microscopy (SEM). (n.d.). Retrieved May 22, 2018, from http://www.microscopy.ethz.ch/sem.htm

Schreiber, W. F. (2012). *Fundamentals of electronic imaging systems: some aspects of image processing* (*15*). Springer Science & Business Media.

Schulze, D., Heiland, M., Thurmann, H., & Adam, G. (2004). Radiation exposure during midfacial imaging using 4-and 16-slice computed tomography, cone beam computed tomography systems and conventional radiography. *Dentomaxillo facial Radiology*, *33*(2), 83–86.

Seferis, I. E., Fiaczyk, K., Spassky, D., Feldbach, E., Romet, I., Kirm, M., & Zych, E. (2017). Synthesis and luminescence properties of $BaHfO_3$:Pr ceramics. *Journal of Luminescence*, *189*, 148–152.

Shang, M., Li, G., Kang, X., Yang, D., Geng, D., & Lin, J. (2011). Tunable luminescence and energy transfer properties of $Sr_3AlO_4F:RE^{3+}$ (RE= Tm/Tb, Eu, Ce) phosphors. *ACS Applied Materials & Interfaces*, *3*(7), 2738–2746.

Sheldon, R. (2012). *Metal-catalyzed oxidations of organic compounds: mechanistic principles and synthetic methodology including biochemical processes*. Elsevier.

Shen, W. H., & Naito, S. (2014). Easy precipitation method for preparation of cerium added $La_2O_2SO_4$ used for oxygen storage. In *Advanced Materials Research* (*886*, 196–199). Trans Tech Publ.

Skoog, D. A., Holler, F. J., & Crouch, S. R. (2017). *Principles of instrumental analysis*. Cengage learning.

Sohn, J. M., Kim, M. R., & Woo, S. I. (2003). The catalytic activity and surface characterization of $Ln_2B_2O_7$ (Ln= Sm, Eu, Gd and Tb; B= Ti or Zr) with pyrochlore structure as novel CH_4 combustion catalyst. *Catalysis Today*, *83*(1–4), 289–297.

Song, L., Du, P., Jiang, Q., Cao, H., & Xiong, J. (2014). Synthesis and luminescence of high-brightness $Gd_2O_2SO_4$: Tb^{3+} nanopieces and the enhanced luminescence by alkali metal ions co-doping. *Journal of Luminescence*, *150*, 50–54.

Sontakke, A., Ferrier, A., & Viana, B. (2017). Afterglow luminescence in sol-gel/Pechini grown oxide materials: persistence or phosphorescence process. *Oxide-based Materials and Devices VIII* (*10105*, 101050U). International Society for Optics and Photonics.

Souamti, A., Martín, I. R., Zayani, L., Lozano-Gorrín, A. D., & Chehimi, D. B. H. (2017). Luminescence properties of Pr^{3+} ion doped Mg-picromerite Tutton salt. *Journal of Luminescence*, *188*, 148–153.

Spahn, M., Strotzer, M., VÖlk, M., BÖhm, S., Geiger, B., Hahm, G., & Feuerbach, S. (2000). Digital radiography with a large-area, amorphous-silicon, flat-panel X-ray detector system. *Investigative Radiology*, *35*(4), 260–266.

Spinks, J. W. T., & Woods, R. J. (1976). An Introduction to Radiation Chemistry, *22*(22054407), 504.

Tan, X., Fan, Q., Wang, X., & Grambow, B. (2009). Eu (III) sorption to TiO_2 (anatase and rutile): batch, XPS, and EXAFS studies. *Environmental Science & Technology*,

43(9), 3115–3121.

Theuwissen, A. J. (2006). *Solid-state imaging with charge-coupled devices* (Vol. 1). Springer Science & Business Media.

University, M. (1999). Chapter 4 Scintillation Detectors. *Radioisotopes and Radiation Methodology*, *Viitattu: 29.1.2018*, 1–10. Retrieved from https://www.science.mcmaster.ca/radgrad/images/6R06CourseResources/4R6Notes4_ScintillationDetectors.pdf

Valeur, B., & Berberan-Santos, M. N. (2012). *Molecular fluorescence: principles and applications*. John Wiley & Sons.

Valeur, B., & Brochon, J.-C. (2012). *New trends in fluorescence spectroscopy: applications to chemical and life sciences* (*1*). Springer Science & Business Media.

Wakefield, G., Holland, E., Dobson, P. J., & Hutchison, J. L. (2001). Luminescence properties of nanocrystalline Y2O3: Eu. *Advanced Materials*, *13*(20), 1557–1560.

Wang, X., Liu, Q., Bu, Y., Liu, C.-S., Liu, T., & Yan, X. (2015). Optical temperature sensing of rare-earth ion doped phosphors. *Rsc Advances*, *5*(105), 86219–86236.

Weber, E. M. J., Dotsenko, a V, Glebov, L. B., & Tsekhomsky, V. a. (2003). *Handbook Of Optical Laser and Optical Science and Technology Series Physics and Chemistry of Photochromic Glasses*. *Optical Materials* (*23*).

Weber, M. J. (2004). Scintillation: mechanisms and new crystals. *Nuclear Instruments and Methods in Physics Research Section A: Accelerators, Spectrometers, Detectors and Associated Equipment*, *527*(1–2), 9–14.

Weeks, A. R. (1996). *Fundamentals of electronic image processing*. SPIE Optical Engineering Press Bellingham.

White, J. G., Amos, W. B., & Fordham, M. (1987). An evaluation of confocal versus conventional imaging of biological structures by fluorescence light microscopy. *The Journal of Cell Biology*, *105*(1), 41–48.

Woodhead, J. L., & Segal, D. L. (1984). Sol-gel processing. *Chemistry in Britain*, *20*(4), 310–313.

Wright, J. D., & Sommerdijk, N. A. J. M. (2014). *Sol-gel materials: chemistry and applications*. CRC press.

Wu, X., You, H., Cui, H., Zeng, X., Hong, G., Kim, C.-H., Park, C.-H. (2002). Vacuum ultraviolet optical properties of (La, Gd) PO_4: RE^{3+} (RE= Eu, Tb). *Materials Research Bulletin*, *37*(9), 1531–1538.

X-Ray tubes. (n.d.). Retrieved May 18, 2018, from https://www.crtsite.com /page5.html

Xia, Z., & Meijerink, A. (2017). Ce^{3+}-Doped garnet phosphors: composition modification, luminescence properties and applications. *Chemical Society Reviews*, *46*(1), 275–299.

Xie, R.-J., Hirosaki, N., Li, Y., & Takeda, T. (2010). Rare-earth activated nitride phosphors: synthesis, luminescence and applications. *Materials*, *3*(6), 3777–3793.

Xu, D., Yu, P., & Tian, L. (2017). Luminescence properties of Pr^{3+} and Bi^{3+} co-doped NaCaTiNbO6 phosphor for red-LEDs. *Journal of Rare Earths*.

Xu, M., Wang, L., Jia, D., & Le, F. (2015). Luminescence properties and energy transfer investigations of $Zn_2P_2O_7$:Ce^{3+}, Tb^{3+} phosphor. *Journal of Luminescence*, *158*, 125–129.

Yaffe, M. J., & Rowlands, J. A. (1997). X-ray detectors for digital radiography. *Physics in Medicine & Biology*, *42*(1), 1.

Yanagida, T. (2018). Inorganic scintillating materials and scintillation detectors. *Proceedings of the Japan Academy, Series B*, *94*(2), 75–97.

Ye, S., Xiao, F., Pan, Y. X., Ma, Y. Y., & Zhang, Q. Y. (2010). Phosphors in phosphor-converted white light-emitting diodes: Recent advances in materials, techniques and properties. *Materials Science and Engineering: R: Reports*, *71*(1), 1–34.

Yildirim, S., Asal, E. C. K., Ertekin, K., & Celik, E. (2017). Luminescent properties of scintillator nanophosphors produced by flame spray pyrolysis. *Journal of Luminescence*, *187*, 304–312.

Yoshida, A., & Horiuchi, H. (2015, October 13). *U.S. Patent No. 9,158,009*. Washington, DC: U.S. Patent and Trademark Office.

Zhang, D.-D., Liu, J.-M., Song, N., Liu, Y.-Y., Dang, M., Fang, G.-Z., & Wang, S. (2018). Fabrication of mesoporous $La_3Ga_5GeO_{14}:Cr^{3+}$, Zn^{2+} persistent luminescence nanocarriers with super-long afterglow for bioimaging-guided in vivo drug delivery to the gut. *Journal of Materials Chemistry B*, *6*(10), 1479–1488.

Zhang, J., & Gao, L. (2004). Synthesis and characterization of nanocrystalline tin oxide by sol–gel method. *Journal of Solid State Chemistry*, *177*(4–5), 1425–1430.

Zhen, X., Tao, Y., An, Z., Chen, P., Xu, C., Chen, R., Pu, K. (2017). Ultralong Phosphorescence of Water-Soluble Organic Nanoparticles for In Vivo Afterglow Imaging. *Advanced Materials*, *29*(33).

Zhou, J., & Xia, Z. (2015). Luminescence color tuning of Ce^{3+}, Tb^{3+} and Eu^{3+} codoped and tri-doped $BaY_2Si_3O_{10}$ phosphors via energy transfer. *Journal of Materials Chemistry C*, *3*(29), 7552–7560.

Zhou, Y., Lin, J., Yu, M., Wang, S., & Zhang, H. (2002). Synthesis-dependent luminescence properties of $Y_3Al_5O_{12}$: Re^{3+} (Re= Ce, Sm, Tb) phosphors. *Materials Letters*, *56*(5), 628–636.

Zhu, Q., Li, J.-G., Li, X., & Sun, X. (2009). Morphology-dependent crystallization and luminescence behavior of (Y, Eu)2O3 red phosphors. *Acta Materialia*, *57*(20), 5975–5985.

Zlatev, I., Wang, L., & Steinhardt, P. J. (1999). Quintessence, cosmic coincidence, and the cosmological constant. *Physical Review Letters*, *82*(5), 896.